Evaluating Measurement Techniques: Establishing a Testing Framework for Residual Stress in Selective Laser Melted Ti-6Al-4V

by
Lucas Steven Anderson

Thesis presented in partial fulfilment of the requirements for the degree of Master of Engineering (Mechanical) in the Faculty of Engineering at Stellenbosch University

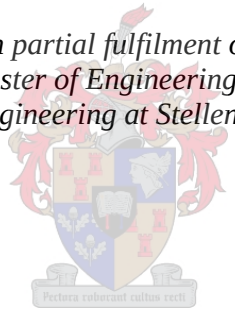

Supervisor: Dr Thorsten Herman Becker
Co-supervisor: Dr Johan Westraadt

December 2017

Declaration

By submitting this thesis electronically, I declare that the entirety of the work contained therein is my own, original work, that I am the sole author thereof (save to the extent explicitly otherwise stated), that reproduction and publication thereof by Stellenbosch University will not infringe any third party rights and that I have not previously in its entirety or in part submitted it for obtaining any qualification.

December 2017

Abstract

Residual stress (RS) plays an important role in the mechanical performance of components. Due to the manufacturing process involved in Selective Laser Melting (SLM), high RS is generated within the produced components. These stresses can increase component failure rates either during the manufacturing phase or in service.

An investigation was performed into the capabilities of various stress measurement techniques for the application of measuring the RS distribution in SLM produced Ti-6Al-4V (Ti64). This investigation will be used as the basis for creating a testing framework for further studies involving the RS distribution in SLM produced Ti64.

The stress measurement techniques were identified and reviewed with respect to the following: stress scale measurable, the stress tensor produced, measurement type, measurement penetration into SLM produced Ti64 and the achievable stress resolution in Ti64. Three techniques were selected for further evaluation, namely: neutron diffraction (ND), X-ray diffraction (XRD) and stress relaxation coupled with Digital Image Correlation (DIC).

SLM produced Ti64 specimens built with nine combinations of build layer thickness and exposure strategy were used as test specimens. ND was used to resolve the macro-stress distribution along a plane running through the depth of the tested specimens and XRD was used to measure both near surface stress and, combined with electro-polishing, the stress distribution through individual build layers. The development of a technique – using focused ion beam (FIB) micro-milling and DIC displacement mapping – for the measurement of the residual stress at the layer scale, was also initiated.

ND was capable of performing volumetric stress distribution measurements through the full depth of the specimens. Long testing durations and limited accessibility limits its application to RS measurements in SLM produced Ti64. A reduced analysis domain should be used in future testing to allow for more stress orientations to be scanned.

The XRD technique, coupled with electro-polishing, was capable of resolving the in-plane stress distribution through individual build layers. The use of the $\sin^2\psi$ method simplifies the calculation of the stress components. Care should be taken when interpreting the results obtained at the surface as high surface roughness can lead to erroneous stress results.

Due to equipment failure the FIB-DIC technique could not be investigated fully. A validation test showed that the technique was able to resolve the in-plane strain components resulting from stress relaxation to a depth of ~20 µm. Further work on this method will include testing on SLM produced Ti64 specimens.

The influence of build layer thickness and exposure strategy on RS was also investigated. An increase in the build layer thickness resulted in a decrease in the stress component magnitude and gradient at both the component scale and at the layer scale. The exposure strategy influences the homogeneity of the stress distribution. A uni-directional exposure strategy produces an approximately uni-axial stress distribution at the component scale, whereas the use of two or more laser vector directions results in an approximately bi-axial stress distribution at the component scale. The stress distribution at the layer scale remains uni-axial regardless of the exposure strategy used.

Opsomming

Residuele spanning (RS) speel 'n belangrike rol in die meganiese gedrag van komponente. Die vervaardigingsproses van Selektiewe Lasersmelting (SLM) genereer hoë interne RS in komponente. Hierdie belastings kan die voorkoms van komponentfaling tydens die vervaardigingsfase of tydens gebruik verhoog.

‘n Ondersoek is uitgevoer in die doeltreffendheid van verskeie spanningmeetingstegnieke vir RS in SLM vervaardigde Ti-6Al-4V (Ti64). Hierdie ondersoek sal gebruik word as ‘n basis vir die skep van 'n toetsraamwerk vir verdere studies van RS-verspreiding in SLM vervaardigde Ti64 komponente.

Die spanningsmetingstegnieke wat geïdentifiseer was is hersien met betrekking tot: die meetbare spanning skaal, die spanningstensor wat gebou kan word, die tipe metings wat uitgevoer is, hul metingspenetrasie in SLM vervaardigde Ti64 en laastens, die haalbare spanningsresolusie in komponente. Drie tegnieke was gekies vir verdere evaluering, naamlik: neutron diffraksie (ND), X-straal diffraksie (XD) en materiaal ontspanning in samewerking met digitale beeldkorrelasie (DBK).

SLM vervaardigde Ti64-monsters is met nege kombinasies van laagdikte en blootstellingstrategieë gebou. ND is gebruik om die makrospanningvelde te aniliseer op die vlak wat deur die diepte van die getoetsmonsters loop. XD is gebruik om beide naby-oppervlakspanning te meet en, gekombineer met elektropolering, om die spanningsverdeling van individuele boulae te meet. Die ontwikkeling van 'n tegniek vir die meting van die RS op die skaal van die geboude lae is ondersoek met behulp van gefokusde ioonbundel (FIB) mikrograaf en DBK-verplasingsmetings.

Die studie het gevind dat ND in staat was om volumetriese spanningsverdelingsmetings deur die volle diepte van die monsters te neem. Lang toetstye en beperkte toeganklikheid beperk ND se toepassing op RS-metings in SLM vervaardig Ti64. Daar was bevind dat 'n verminderde analise gebied gebruik moet word in toekomstige toetse om voorsiening te maak vir ’n groter aantal geskandeerde spanningsoriëntasies.

Die XD-tegniek, tesame met elektropolering, kon die in-vlak spanningsverdeling verkry deur individuele boulae. Die gebruik van die $\sin^2\psi$-metode vereenvoudig die berekening van die spanningskomponente. Voldoende sorg moet geneem word met die interpretering van resultate wat op die oppervlak verkry word omdat hoë oppervlakrofheid kan lei tot foutiewe spanningslesings.

As gevolg van toerustingonderbreking, kon die FIB-DBK-tegniek nie volledig ondersoek word nie. 'n Validasietoets het getoon dat hierdie tegniek die spanningskomponente van spanningsverslapping in die boulae tot 'n diepte van

~20 µm kon bereken. Verdere werk op hierdie metode sal die toetsing van SLM vervaardig Ti64-monsters insluit.

Die invloed van die boulaagdikte en blootstellingstrategie op RS is ook ondersoek. 'n Verhoging van die boulaagdikte het daartoe gelei dat die spanningskomponent se grootte en gradiënt op beide die komponentskaal en die boulaag skaal verminder is. Daar was verder bevind dat die blootstellingstrategie beïnvloed die homogeniteit van die spanningsveld. 'n Enkelrigtingsblootstellingstrategie veroorsaak 'n ongeveer eenassige spanningsverdeling op die komponentskaal, terwyl die gebruik van twee of meer laservektorrigtings 'n ongeveer twee-assige spanningsverdeling op die komponentskaal tot gevolg bring. Die spanningsverdeling op die boulaagskaal bly eenassig ongeag die blootstellingstrategie wat gebruik word.

Acknowledgements

I would like to extend my thanks to the following persons and organizations that made the completion of this project possible.

To my parents, Jon and Janine Anderson, for their continual support and encouragement over the past two years. I would not have gotten to this point in my academic career if not for them.

To my friends, Daniel Lombard, Edgar Niit, Arno Scholtz, Nicol Pirow, Nico Naude and Kyle Beecham for their encouragement through the duration of this project and to my friend Kerry Lanz for assisting with the proof reading of this report.

To my supervisor, Dr. Thorsten Becker, for the guidance and assistance he provided in steering this project down the correct path. Your patience, advice and enthusiasm has been thoroughly appreciated.

To my co-supervisor at Nelson Mandela University, Dr. Johan Westraadt, for his guidance and assistance in the use of the FIB/SEM as well as the guidance he gave during the duration of this project.

To my fellow researchers in the Materials Engineering Research Group at Stellenbosch University for the office humour, social outings, encouragement and support over the past two years. Thank you Nur Dhansay, Matt Molteno and Richard Huchzermeyer. Special thanks to Melody van Rooyen and Gerrit ter Haar who helped with the translation of the abstract.

To the staff at StressTech Oy and Esteq for the assistance with the XRD stress vs depth profiling analyses. Particular thanks go to Juha Siiriänen for his in depth assistance in understanding the process with which the tests were performed and XRD in general.

To Dr Andrew Venter and the staff at the neutron diffraction test centre run by the South African Nuclear Energy Corporation for their assistance in performing the neutron diffraction analyses and surface XRD analyses as well as the general information provided by Dr Andrew Venter on the use of diffraction techniques for stress measurement.

To the team at the Department of Metallurgy and Materials Engineering, University of Leuven, for providing the test specimens used in this project and for advice given over the duration of the research.

Lastly, thanks must be given to the CPAM initiative, South African Department of Science and Technology and Stellenbosch University for funding and supporting this project. It could not have been performed otherwise.

Table of contents

List of figures

Page

List of tables

Page

List of abbreviations

3D	3 Dimensional
AM	Additive Manufacturing
ASTM	American Society for Testing and Materials
BSI	British Standard Institute
CAD	Computer Aided Design
CCD	Charge Coupled Device
CHRTEM	Centre for High Resolution Transmission Electron Microscopy
CPAM	Collaborative Program for Additive Manufacturing
CSIR	Centre for Scientific and Industrial Research
DIC	Digital Image Correlation
DMLS	Direct Metal Laser Sintering
EDM	Electronic Discharge Machining
FIB	Focused Ion Beam
FIB/SEM	Dual beam Focused Ion Beam / Scanning Electron Microscope
ICE	Ion Conversion and Electron Detector
LBM	Laser Beam Melting
LMF	Laser Metal Fusion
ND	Neutron Diffraction
NECSA	South African Nuclear Energy Corporation
NMU	Nelson Mandela University
PSD	Position Sensitive Detector
RESTAN	Residual Stress Analyser
ROI	Region of Interest
RS	Residual stress
SEM	Scanning Electron Microscope
SLM	Selective Laser Melting
SOI	Site of Interest
TGM	Temperature Gradient Mechanism

Ti64	Titanium - 6 Aluminium - 4 Vanadium
XRD	X-ray Diffraction

Nomenclature[1]

d'	Inter lattice spacing
d_0	Strain free lattice spacing
$d_{\phi\psi}$	Lattice spacing in the direction defined by the Phi and Psi angle
E	Young's Modulus
e_{sys}	Systematic error
H	Layer thickness
$\boldsymbol{h}$	Vector of depth increments
hkl	Family of crystallographic planes
$\boldsymbol{h}_{scaled}$	Depth increment scaled by layer thickness
$K\alpha$	Radiation type
m	gradient of d vs. sin2ψ plot
n	Integer number
P	Position of the central point in a subset
P^*	Displaced position of the central point in a subset
S_1, S_2	Diffraction elastic coefficients
x, y, z	Cartesian coordinate directions
x_1^*, x_2^*	coordinates of the displaced central point in a subset
x_1,x_2	Coordinates of the central point in a subset
γ_{xy}	Directional shear strain component
δ_{DIC}	Displacement measured using DIC
δ_{ij}	Kronecker delta coefficient
δ_{ref}	Reference displacement performed by stage translation
ε_i	Principal strain component
ε_{ii}	Normal strain tensor components
ε_{ij}	Shear strain tensor components
ε_{xx}, ε_{yy}, ε_{zz}	Directional normal strain components

[1] This document makes use of SI units for all stated values.

ε_{ψ}	Lattice strain at a particular Psi angle
θ	The half Bragg angle
λ	Radiation wavelength
ν	Poisson's Ratio
$\boldsymbol{\sigma}$	Stress tensor
σ_1	Maximum principal stress component
σ_2	Middle principal stress component
σ_3	Minimum principal stress component
σ_{avg}	Average value of particular stress component vector
σ_i	Principal stress component
σ_{ii}	Normal stress tensor components
$\boldsymbol{\sigma_{ii}}$	Stress component vector
σ_{ij}	Shear stress tensor components
$\boldsymbol{\sigma}_{scaled}$	Rescaled stress component vector
σ_{xx} ,σ_{yy}, σ_{zz}	Directional normal stress components
σ_{ϕ}	Stress in the direction of angle Phi
τ_{xy}, τ_{zx}, τ_{yz}	Directional shear stress components
ϕ	Phi angle of rotation of a specimen about its surface normal
χ	Chi angle of rotation about diffraction Chi axis
ψ	Psi angle between the diffraction plane normal and specimen normal
ω	Omega angle between the incident radiation beam and the sample surface
2θ	The Bragg angle

1 Introduction

For centuries, manufacturing has relied on methods that produce a component out of a mass of raw material through subtractive methods – be it using a chisel to sculpt Michelangelo's David from a block of marble or a CNC lathe to turn a Formula One car's crank shaft from a cylinder of high chrome steel. Regardless of the material, process or product, subtractive methods all have one thing in common: material wastage. This waste material is generally in the form of offcuts or shavings and, depending on the material being processed, may be recyclable, but at a high energy cost. Thus, in recent years, there has been a considerable move towards additive manufacturing (AM) methods, which aim to expedite the manufacturing process while cutting down on material wastage.

A group of AM processes that is at the cutting edge of metal fabrication is Laser Beam Melting (LBM) manufacturing. LBM is the common name given to a group of powder-bed fusion AM technologies that use a high power laser in order to produce components in a layer-wise fashion (Herzog *et al.*, 2016). This group includes AM technologies such as Direct Metal Laser Sintering (DMLS), LaserCUSING and Laser Metal Fusion (LMF). However, Selective Laser Melting (SLM) has become the most commonly used term when referring to LBM technology (Murr *et al.*, 2012).

The research reported in this document is aimed at identifying technologies that may be used in the measurement of residual stress (RS) in SLM produced Ti-6Al-4V (Ti64); a titanium based alloy containing 6% aluminium and 4% vanadium by weight. Ti64 is used in a range of applications including medical implant and aerospace components (Rack and Qazi, 2006; Boyer, 1996). RS plays an important role in the mechanical performance of material and as such, there is often a need to quantify its distribution through a component. As the choice of measurement technique is dependent on the type of stress being measured, it is important to understand the capabilities of the various stress measurement techniques available in order to make a selection that is suitable for the intended application. This process has not yet been fully explored in regards to measuring RS in SLM produced Ti64.

The project was conducted under the supervision of Dr Thorsten Becker, from Stellenbosch University and the co-supervision of Dr Johan Westraadt, from Nelson Mandela University (NMU). The project forms part of the Collaborative Program for Additive Manufacturing (CPAM). This program involves a number of South African institutions, namely Stellenbosch University, the Central University of Technology, the Vaal University of Technology and the University of Cape Town, North West University, the National Laser Institute at CSIR and Aerosud. The aim of this program is the qualification of SLM Ti64 for industrial

application in the South African manufacturing environment. As such it is comprised of a number of research fields directed at studying the mechanical performance of SLM produced Ti64; including fracture toughness and fatigue life, achievable microstructure through heat treatments, measuring RS distribution and improving the stress strain characteristics of the material.

In the context of manufacturing in South Africa, SLM is an emerging technology with the major drivers being the institutions involved in the CPAM initiative. Through their collaborative research, these institutions are striving to bring SLM to the forefront of modern manufacturing technology in South Africa.

The research was initiated in 2016 and aims to be concluded at the end of 2017. The work required for this research was performed at a number of locations, including sample production at Leuven University in Belgium and experimental testing at the Centre for High Resolution Transmission Electron Microscopy (CHRTEM) at Nelson Mandela University, the SAFARI-1 research reactor run by the South African Nuclear Energy Corporation (NECSA) and at StressTech Oy in Finland.

1.1 Project Background

AM, more popularly known as 3D printing, is slowly becoming the preferred answer to the question of how to produce complex parts quickly and with minimal wastage. AM can be applied to a wide variety of materials, from ceramics to plastics to high strength metals, and has a multitude of applications. These applications range from the manufacture of custom medical implants and prostheses to creating sand casting molds to printing houses. Simply put, AM is a process that functions on the principle of producing a component from a computer aided design (CAD) model through some form of material additive process (Gibson *et al.*, 2010). As components are formed by adding material, as opposed to subtracting from a larger material mass, the gross amount of material used is reduced and consequently the amount of material wasted is reduced.

SLM is one of the many methods of AM that can be defined as a three dimensional printing process that utilizes a high powered laser to melt a powdered metallic material. SLM uses a layer-by-layer growth process in order to produce a component (Wong and Hernandez, 2012). SLM has become a popular manufacturing method for low volume, high intricacy products due to its high accuracy and ability to produce complex geometries without part specific tooling (Bremen *et al.*, 2012).

Due to its manufacturing abilities SLM is well suited to application which makes use of advanced metals such as Titanium alloys. Ti64 is known as the workhorse of the Titanium alloys and has application in a wide range of industries due to its wear and corrosion resistance, superb mechanical properties and biocompatibility (Boyer, 1996; Rack and Qazi, 2006). However, there are also disadvantages to

SLM manufactured Ti64, chief amongst which is high RS and low material ductility. These are both driven by the same mechanism of local heating, followed by rapid cooling (Zaeh and Branner, 2009). High RS, which can sometimes exceed the yield strength of the material, leads to part deformation - affecting dimensional accuracy, affect mechanical strength and in some cases contribute to crack formation, separation of the part from the base plate or even delamination (Zaeh and Branner, 2009). These issues detract from the overall usefulness of SLM in the manufacturing field.

Studies have been performed on the RS build-up in SLM manufactured components for a variety of materials. Often these studies rely on FE modelling of the system in order to estimate how the stress develops as the component is grown (Parry *et al.*, 2016; van Belle *et al.*, 2013). Alternately there has been studies performed using experimentation to calculate the RS present at the component scale. These studies commonly employ a form of destructive testing, such as hole drilling,, crack compliance method, beam deflection method or the contour method as a means of quantifying the RS present in the component as a whole (Knowles *et al.*, 2012; Thöne and Leuders, 2012; Vrancken *et al.*, 2014; Mercelis and Kruth, 2006). Non-destructive testing in terms of X-ray diffraction (XRD) has also been employed in previous research as a means to calculate the stress at the surface of built specimens (Yadroitsev and Yadroitsava, 2015).

There is, however, no conclusive method for calculating the RS in SLM manufactured components. This is due to the unique way in which RS propagates through the component during the SLM process. Thus, there are two trajectories when discussing the topic of RS in SLM manufacturing. The first is the identification of suitable technologies for the measurement of RS and the second is the application of these technologies with the intent of quantifying the RS present in SLM components.

1.2 Project Motivation

In recent years much emphasis has been placed on the qualification of SLM produced Ti64 for the use in the aerospace and biomedical fields. This qualification is based on the achievable mechanical properties as well as post processing of components. Part of this qualification is in understanding the RS that is present in the manufactured parts before undergoing any post manufacturing process, such as heat treatment and/or surface treatment. As RS development is inherent to the build process, a better understanding of how this development occurs and is influenced by the build parameters may help to reduce their effects and aid in the qualification of SLM produced Ti64 components.

According to Withers and Bhadeshia (2001a) RS exists at three scales. Type I RS acts over large areas of a body and equilibrate over macroscopic dimensions. These stresses can also be referred to as part level stresses as they exist at a scale

that is approximately equal to the scale of the body that hold them. Type II stresses are microscopic stresses which exist at a scale that is within one order of magnitude of the grain size of the material. These are typically caused by thermal expansion mismatching in multiphase materials. Type III RS acts at the atomic scale and equilibrate within a single grain of the material.

RS in SLM is unique due to the layer wise process in which parts are manufactured. This process causes appreciable stresses to be generated at not only the part scale (Type I), micro-scale (Type II) and atomic scale (Type III), but also at a scale somewhere between Type I and Type II. This fourth stress scale arises in the build layers as a result of the layer-wise manufacturing process of SLM. It is the contribution of layer-wise stress build up that, with each additional build layer, ultimately leads to the formation of RS in a component. Figure 1.1 provides a visual representation of the different stress scales in an SLM build component in terms of the stress distribution through a single layer, the stress state of a single layer as well as how the stress in each individual layer leads to the stress distribution found in SLM produced components. It is as a result of these three levels of stress that the study of the RSes present in SLM components is challenging.

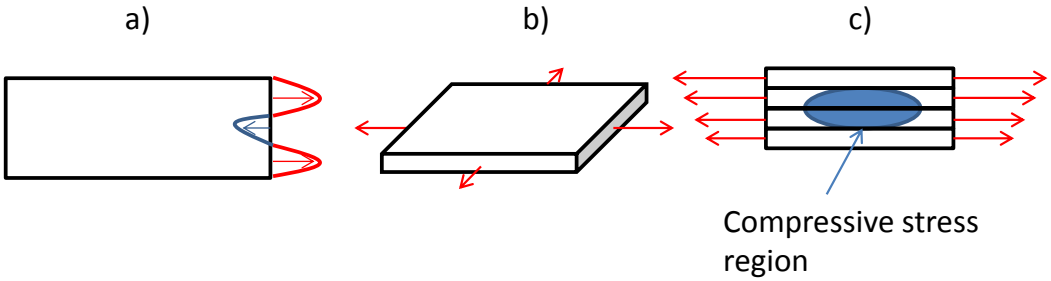

Figure 1.1 Illustration of a) the possible stress distribution through a single layer, b) the stress state of a single layer and c) the accumulated stress state from a number of layers. Red represents tensile stress and blue represents compressive stress.

An initial aim of the research lies in identifying testing procedures that are capable of measuring RS at the required scales, namely Type I down to Type II. This identification of testing procedures and the evaluation of their capabilities will establish a framework for the use in future research. Furthermore, such a framework aims to develop a holistic experimental methodology that is capable of quantifying RS in SLM produced Ti64 components. This entails identifying measurement techniques that are capable of quantifying stress at both the part scale and at the layer scale.

A secondary aim lies in investigating the stress distribution using the identified framework. This investigation includes the measurement of RS at both the part scale as well as the stress distribution through individual build layers. The

connection between part and layer stress formation aims to establish an understanding of the link between the part stress distribution and the layer stress distribution.

1.3 Objectives

A mentioned above, the aim of this research is to i) identify suitable measurement techniques that can be used for resolving the RS distribution at both the part scale and layer scale; and ii) to apply these techniques to the measurement of stress build-up in SLM Ti64 parts. The following key objectives have been identified for this project:

- Complete an in-depth literature study on SLM and the techniques that can be applied to measure RS.
- Review the measurement techniques with respect to their measurement scale range and applicability to SLM.
- Identify and develop suitable measurement techniques for experimental testing
- Acquire simple samples that have differing build parameters to be investigated.
- Determine how the RS is affected by the change of layer thickness and exposure strategy

1.4 Scope

This project is aimed at investigating techniques that may be applied to measuring the RS distribution and magnitude of as-built SLM components once they have been released from the base plate. Specifically, the interest is in identifying techniques that can be used to calculate the stress at both the macro (part) scale (Type I stress) and at the micro (layer) scale. An additional aspect of this work is an investigation into how changing the build layer thickness and laser exposure strategy influences the RS present.

The testing conducted in this research is a combination of standard testing procedures such as diffraction methods and the development of a prototype testing method for measuring RS at the layer level. The techniques identified as being applicable to SLM will be used as a means to qualify the RS distribution through the body of the samples at both the macro and micro scale.

The prototype method was unsuccessful in delivering final stress values as the methodology chosen was not refined enough to produce acceptable stress results. As such, the calculation of stress from the displacements measured by this method falls outside the scope of this document. However, the methodology developed for

performing the stress relaxation and measuring the resultant displacement was successful and will be addressed in this report.

1.5 Layout of Thesis

An investigation into the measurement techniques applicable for determining the RS in SLM Ti64 is detailed in this document. A thorough background investigation of SLM, RS and various strain measurement techniques is presented in Chapter 2. This chapter will include a brief overview of the current research being done into RS in SLM Ti64. Chapter 3 presents a review and selection of appropriate RS measurement techniques. This chapter will assist the reader in understanding the fundamental concepts of the testing and analysis used in this project. The experimental methodology and the results obtained from the relevant testing procedures will then be presented in Chapter 4 and Chapter 5, respectively. Chapter 5 will also present a post testing technique analysis. Following this, Chapter 6 will present a full discussion of the results from all testing. The document is concluded in Chapter 7.

2 Background reading

This section will contextualize the background knowledge necessary to understand the SLM process and the role RS plays in SLM produced components. Further, it will provide details on how the stress tensor is defined and its relationship with the strain tensor. Understanding the concept of the stress tensor is important to the understanding of the various stress measurement techniques and the assumptions that they employ. A brief overview of the strain measurement techniques that were investigated during this project will then be presented and finally three key papers will be reviewed.

2.1 Selective Laser Melting as a manufacturing method

SLM, and AM in general, has the unique manufacturing ability to produce components that have complex geometries and internal features without the need for part-specific tooling (Bremen *et al.*, 2012). The biomedical and aerospace industries currently make use of this ability for the production of prototype and low production volume, high complexity components. A key advantage to the biomedical industry is that prosthetics can be produced to fit a patient perfectly, using models created by performing CT scans of the patient's anatomy (Bremen *et al.*, 2012).

The feedstock for SLM is an atomized metallic powder, typically with particle sizes ranging from 10 µm – 60 µm (Murr *et al.*, 2012). A variety of metals can be

used in SLM fabrication, including Titanium alloys, Aluminium alloys, Nickle based super-alloys and various steels (Wong and Hernandez, 2012). This powder is deposited, in layers of 20 μm – 100 μm, on a massive substrate made of a similar material, known as a base plate (Herzog *et al.*, 2016).

Industrial machines utilize a laser source that generates light at wavelengths between 1060 nm and 1080 nm at a laser power that ranges from 20 W to 1 kW(Herzog *et al.*, 2016). However, specialized, high speed machines, such as the AeroSwift machine used by Aerosud, can be fitted with a laser of up to 5 kW for rapid production. The laser impinges on the metal powder at a focused spot and is scanned along vectors that are specified by the laser exposure strategy. This strategy defines the laser velocity, hatch spacing and scanning pattern used (Herzog *et al.*, 2016). Provided the laser power is sufficient, for the material being used, the impingement of the laser results in melting of both the powdered material and the adjacent, previously solidified, material. The melt pool then cools to fuse with the previously solidified material lying below it (Herzog *et al.*, 2016).

The basic process by which a component is manufactured using SLM can be seen in Figure 2.1. A 3D CAD model of the component is imported into a slicing program which divides the model into layers of the same thickness as the intended build layer thickness. Once a layer of powder has been deposited the laser path is calculated so that the areas that are to contain solid material are scanned by the laser in each slice. This process is repeated, layer by layer, until the final component has been created (Bremen *et al.*, 2012).

The conventional coordinate system used to describe the orientation of components manufactured by SLM is shown in Figure 2.2. Each build layer is deposited and melted in the *x*-*y* plane and the component is grown along the *z*-axis.

2.2 The stress tensor

The stress tensor is a representative element which describes the state of stress at a single point. It consists of normal stresses in three orthogonal directions and shear stresses that act on three orthogonal planes (Dowling, 2013, p.204). The stress tensor does not need to be aligned with the coordinate system of the body in which it lies and can be described by Figure 2.3. The stresses σ_{11}, σ_{22} and σ_{33} are the normal stresses and σ_{12}, σ_{13}, σ_{21}, σ_{23}, σ_{31} and σ_{32} are the shear stresses. Due to equilibrium constraints, the shear stresses σ_{12} and σ_{21}, σ_{13} and σ_{31}, and σ_{23} and σ_{32} must be equivalent. Thus the generalised stress tensor can be described in tensor form using six components as shown in Equation (2.1).

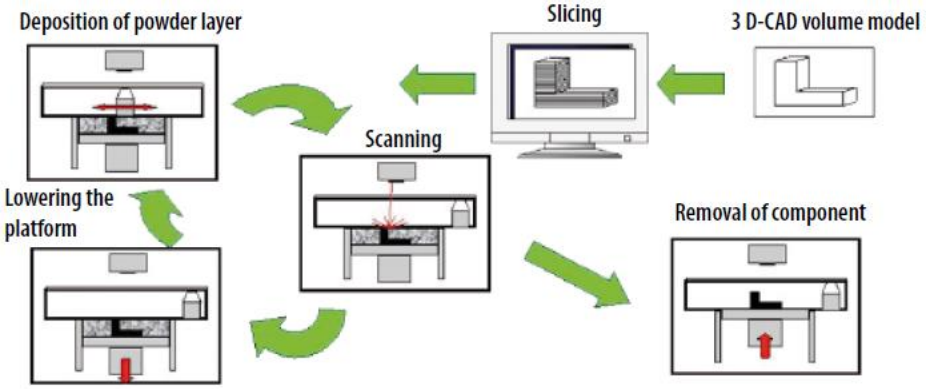

Figure 2.1 Steps used in SLM process from part design to final component (Bremen et al., 2012).

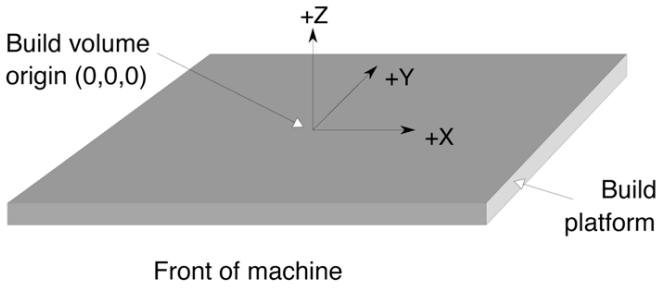

Figure 2.2 Standard coordinate system used for SLM manufacturing (ASTM, 2012).

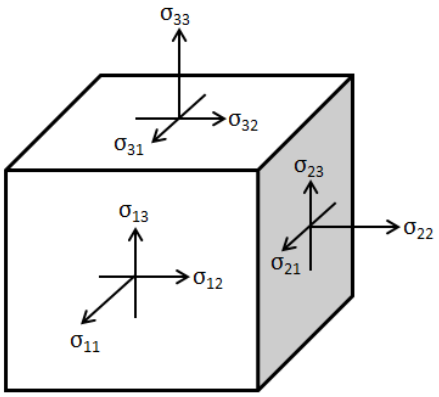

Figure 2.3 The generalised stress tensor element.

$$\boldsymbol{\sigma} = \begin{bmatrix} \sigma_{11} & \sigma_{12} & \sigma_{31} \\ \sigma_{12} & \sigma_{22} & \sigma_{23} \\ \sigma_{31} & \sigma_{23} & \sigma_{33} \end{bmatrix} \tag{2.1}$$

The stress tensor can be related to the corresponding strain tensor by using Equation (2.2) (Dowling, 2013, p.215). However, this equation only holds for isotropic materials. For anisotropic materials the coefficient matrix becomes directionally dependent. Anisotropic materials fall outside the scope of this investigation and as such, will not be discussed further.

$$\begin{Bmatrix} \varepsilon_{11} \\ \varepsilon_{22} \\ \varepsilon_{33} \\ \varepsilon_{12} \\ \varepsilon_{31} \\ \varepsilon_{23} \end{Bmatrix} = \frac{1}{E} \begin{bmatrix} 1 & -\nu & -\nu & 0 & 0 & 0 \\ -\nu & 1 & -\nu & 0 & 0 & 0 \\ -\nu & -\nu & 1 & 0 & 0 & 0 \\ 0 & 0 & 0 & 2+2\nu & 0 & 0 \\ 0 & 0 & 0 & 0 & 2+2\nu & 0 \\ 0 & 0 & 0 & 0 & 0 & 2+2\nu \end{bmatrix} \begin{Bmatrix} \sigma_{11} \\ \sigma_{22} \\ \sigma_{33} \\ \sigma_{12} \\ \sigma_{31} \\ \sigma_{23} \end{Bmatrix}, \tag{2.2}$$

where E is the stiffness of the material, ν is the Poisson's ratio.

These stresses and strains may be aligned with the coordinate system of the body in which they exist, in which case the notation changes as shown in Equation (2.3), assuming the 11-direction is aligned with the *x*-, 22- with the *y*- and 33- with the *z*-axis:

$$\begin{Bmatrix} \sigma_{11} \\ \sigma_{22} \\ \sigma_{33} \\ \sigma_{12} \\ \sigma_{31} \\ \sigma_{23} \end{Bmatrix} \rightarrow \begin{Bmatrix} \sigma_{xx} \\ \sigma_{yy} \\ \sigma_{zz} \\ \tau_{xy} \\ \tau_{zx} \\ \tau_{yz} \end{Bmatrix}, \tag{2.3}$$

where σ_{ii} denotes a normal stress and τ_{ij} denotes a shear stress.

A special state of stress known as plane stress can be assumed under certain circumstances. At the free surface of a body there can be no stress acting in the direction normal to the surface as this would disobey the laws of equilibrium. Thus, from Figure 2.3 the stresses σ_{33}, σ_{13} and σ_{23} must all reduce to zero. Once again, in order to maintain equilibrium, the sum of the moments around the 1- and 2-axes must sum to zero and as such σ_{31} and σ_{32} must also reduce to zero (Dowling, 2013, p.235). Thus, under the plane stress condition the tensor in Equation (2.1) reduces to a tensor with only four components as seen in Equation (2.4)

$$\boldsymbol{\sigma} = \begin{bmatrix} \sigma_{11} & \sigma_{12} \\ \sigma_{12} & \sigma_{22} \end{bmatrix}. \tag{2.4}$$

This can again be expressed, as in Equation (2.3), in the coordinate system of the body by aligning the tensor axes with those of the body. The stress-strain relationship described in Equation (2.2) reduces to Equation (2.5) for the plane stress state.

$$\begin{Bmatrix}\varepsilon_{11}\\ \varepsilon_{22}\\ \varepsilon_{12}\end{Bmatrix} = \frac{1}{E}\begin{bmatrix}1 & -\nu & 0\\ -\nu & 1 & 0\\ 0 & 0 & 2+2\nu\end{bmatrix}\begin{Bmatrix}\sigma_{11}\\ \sigma_{22}\\ \sigma_{12}\end{Bmatrix} \tag{2.5}$$

$$\varepsilon_{33} = -\frac{\nu}{E}(\sigma_{11} + \sigma_{22}).$$

It is important to note that although all stresses in the direction normal to the free surface are reduced to zero, there is a normal strain component, ε_{33}, which exists in this direction. This is due to the Poisson's effect enforcing the conservation of volume.

2.3 Residual stress defined

RS is a phenomenon that can occur in any solid material. It is most comprehensively defined as a stress that is present within the material once all external loading has been removed and one that is not necessary to maintain equilibrium between the body and its environment (Withers and Bhadeshia, 2001b). RS can be generated in numerous ways, including mechanically – through forging or shot peening; thermally – through non-uniform cooling or multiphase materials with each phase having a different coefficient of thermal expansion; or chemically – such as in the nitriding of steel (Withers and Bhadeshia, 2001a).

RS plays a major role in the mechanical performance of components under load. Under loading the RS must be algebraically added to the externally applied stress in order to calculate the total stress state of the body (Withers and Bhadeshia, 2001a). Depending on the magnitude and direction of the stress, this can result in components failing at loads well below that which they were designed for.

RS can be either tensile or compressive. However, in order to maintain equilibrium regions of both tensile and compressive RS must be present within a body while no loading is applied. Depending on the distribution of these tensile and compressive stress regions, the mechanical performance of the body may be improved or diminished (Mercelis and Kruth, 2006). Typically, compressive stresses present at the surface of the body – such as in tempered glass – are beneficial as they improve fatigue performance and prevent crack growth at the surface (Withers and Bhadeshia, 2001b). However, in most cases, RS present in a body acts to diminish the mechanical performance. Tensile stresses often occur near the surface or at stress concentration points and these stresses reduce the body's ability to resist applied loading and crack propagation. Additionally, the removal of residually stressed material result in part deformation as the remaining stress field is redistributed to attain a new equilibrium state. An example of this deformation can be seen in Figure 2.4.

Figure 2.4 Deformation of a section of box tubing, after being cut, caused by achieving a new equilibrium state after the removal of residually stressed material (Simiprof, 2015).

RS exists at a range of scales, from the atomic scale up to the full component scale (Withers and Bhadeshia, 2001a). RS falls under one of three scales, depending on the length over which the stress equilibrates. Type I stresses, commonly referred to as macro-stresses, equilibrate over macroscopic dimensions and have a characteristic length that is on the same scale as the body in which they occur. Type II stresses, known as micro-stresses, equilibrate over a number of grains of the material. These stresses often occur as a result of a mismatch in thermal expansions at an interphase boundary (Withers and Bhadeshia, 2001a). The final scale of stress is Type III stress, known as atomic scale stress. These stresses equilibrate within a single grain and are caused by misfits in the atomic structure, such as dislocations and point defects (Withers and Bhadeshia, 2001a). Stresses of Type I are most commonly investigated as they play the most significant role in the mechanical performance of components. Due to their macroscopic scale, they are also the most easy to resolve. However, both Type II and Type III contribute to the formation of Type I stress.

2.4 Residual stress in Selective Laser Melting

Although SLM has numerous advantages over conventional manufacturing methods such as turning and milling, it still faces a number of process challenges. One of the major challenges is the development of high magnitude RS during the building process which often lead to build failures and/or service failures (Zaeh and Branner, 2009).

The primary mechanism through which RS propagates is known as the Temperature Gradient Mechanism (TGM), which is a result of rapid, localized, heating that occurs at the impingement point of the laser on the material (Knowles *et al.*, 2012). Although it cannot be said that this is the definitive answer to the question of RS generation in SLM, it is the most widely accepted theory proposed in literature. Large thermal gradients form due to the slow conduction of heat

away from the melt pool, which result in a mismatch in the thermal expansion experienced by the heated material and the solidified material surrounding it (Mercelis and Kruth, 2006). The thermal expansion of the heated material is thus constrained by the surrounding solid material, resulting in the formation of elastic compressive stress in the surrounding material. If the expansion is sufficient, the compressive stress in the constraining solid material exceeds the material's yield strength and the constraining material is plastically deformed (Mercelis and Kruth, 2006). It should be noted that due to the elevated material temperature, the yield strength is reduced and as such the stress required to induce plastic strain is lower than that required to produce plastic strain at room temperature.

Upon cooling of the molten region the secondary mechanism of RS propagation occurs, whereby the thermal contraction of the molten region during the state change from liquid to solid is constrained by the plastically deformed solid material surrounding it. This constraint induces tensile stress in the newly solidified region and as a result the top build layer tends to develop a net tensile stress (Yadroitsev and Yadroitsava, 2015). Both of these mechanisms are illustrated in Figure 2.5.

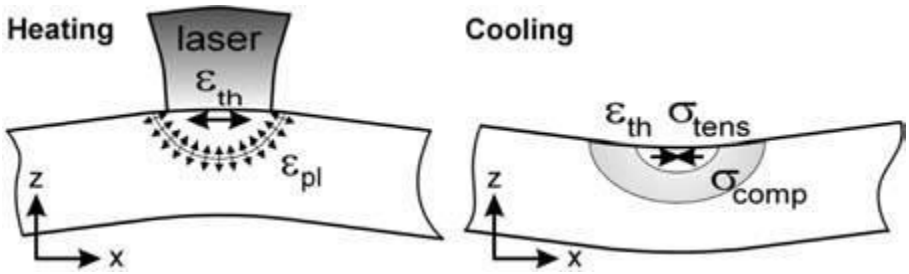

Figure 2.5 Primary and secondary mechanisms of RS generation in SLM manufacturing (Mercelis and Kruth, 2006).

It is the previously solidified material surrounding the heated material that constrains the expansion and contraction. The powdered material adjacent to the laser spot is unable to constrain expansion and as a result the stress in the transverse (perpendicular to the laser path) direction is typically lower than the stress in the longitudinal direction (parallel to the laser path) (Yadroitsev and Yadroitsava, 2015). This has also been found to be the case in laser cladding where, for single track deposition, the first principal stress component lies in the direction of the laser scan direction (de Oliveira *et al.*, 2006). The RS present in the component tends to accumulate with the addition of each build layer. Shiomi, *et al.* (2004) used a numerical model to show that the stress contribution of each build layer can be approximated as a linear function. This model was verified by Mercelis & Kruth (2006). Thus components that have fewer build layers tend to have RS of a lower magnitude (Mercelis and Kruth, 2006).

This layer-wise addition of RS is what makes the distribution of RS in SLM components unique. Each build layer, on its own, exists in a state of plane stress, with a stress tensor described by Equation (2.4), where σ_{11} and σ_{22} are at some rotation from the *x*- and *y*-axis shown in Figure 2.2, respectively. This is due to the fact that thin sections cannot hold significant magnitudes of out of plane stress and that each layer, on its own, is representative of a free surface. However, with the addition of successive build layers, the material below the surface of the component develops a tri-axial state of stress as described by Equation (2.1). This tri-axial state of stress is as a direct result of the addition of layers of plane (biaxial) stress and the mechanical boundary conditions present at the part-base plate interface (Zaeh and Branner, 2009). Although the magnitude of the RS that develops in the direction of the *z*-axis is low compared to that in the *x*-*y* plane, the strain component is the highest (Parry *et al.*, 2016, p.13). This is demonstrated by the tendency of specimens to deform primarily in the direction of the *z*-axis, as shown in Figure 2.6.

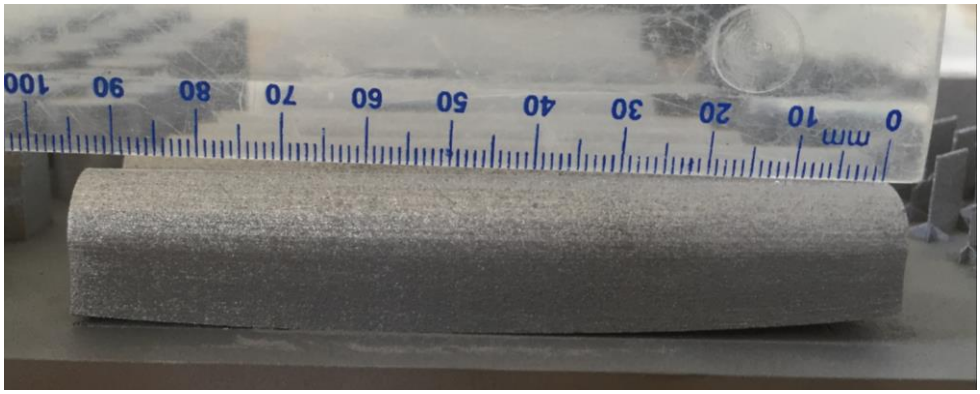

Figure 2.6 Separation from base plate and resultant warping of an SLM built Ti64 specimen due to RS build up during the build process.

The region of highest RS magnitude is found at the top surface of a component and is typically tensile (Casavola *et al.*, 2009; Yadroitsev and Yadroitsava, 2015). These tensile stresses are high and can approach or exceed the yield strength of the material (Knowles *et al.*, 2012). The tensile stress decreases sharply with distance from the top surface, with the magnitude being reduced by ~80% at a depth of 1.5 mm (Casavola *et al.*, 2009; Mercelis and Kruth, 2006; Shiomi *et al.*, 2004). Removal of the part from the base plate results in a drastic reduction in RS as relaxation occurs (Mercelis and Kruth, 2006). After removal, the stress field redistributes and consists of tensile stress zones at the upper and lower surfaces and a compressive stresses between these zone (Mercelis and Kruth, 2006).

The implications of RS on the mechanical performance of SLM manufactured components are similar to the implications for components manufactured by any other means. However, there are certain implications that are unique to SLM. During the build process the RS build-up may be high enough to initiate cracking

in the component before it is completed (Yadroitsev and Yadroitsava, 2015; Vrancken *et al.*, 2014). A further issue is that of delamination, where previously deposited build layers separate from each other entirely as a result of the tensile stresses present in the material (Zaeh and Branner, 2009). An example of this is seen in Figure 2.6, where delamination occurred at the base of the sample, causing it to partially separate from the base plate and warp excessively as the build continued. Furthermore, when parts are released from the build plate, typically using wire electronic discharge machining (wire EDM), the resulting stress relaxation causes components to deform as a new equilibrium state is achieved (Mercelis and Kruth, 2006).

It is due to these factors that RS plays a significant role in the production of components through SLM. Not only does the RS generated affect the mechanical performance of the completed component, but it can also cause failure in the manufacturing of the component.

2.5 Strain measurement techniques

As stress is an extrinsic property, it cannot be directly measured (de Oliveira *et al.*, 2006). Instead, stress quantification techniques detect displacements associated with stress and convert these to elastic strains, which are then used to calculate stress using a relationship such as Equation (2.2). The displacements associated with RS can be measured using either contact methods, such as the application of strain gauges, or non-contact methods such as Digital Image Correlation (DIC) and diffraction methods.

2.5.1 The strain gauge

Strain gauges measure the displacement at a single point on the surface of the object onto which they are bonded (Figliola and Beasley, 2011). The gauge is mechanically bonded to the surface, usually with an adhesive, and is able to detect the displacement of the material onto which it is bonded. A strain gauge is capable of measuring the displacement in the direction in which it is aligned, as shown in Figure 2.7. For deformations to be measured in multiple directions, two or more strain gauges, arranged in a rosette, are required to be oriented in each of the desired measurement directions. With two strain gauges oriented at 90° to one another the ε_{11} and ε_{22} components of Equation (2.5) can be determined. If three strain gauges are used, oriented at an angle of 45° to each other, the full plane strain tensor in Equation (2.5) can be determined. Since strain gauges can only measure in-plane displacement, the out of plane component, ε_{33}, cannot be determined.

As the material onto which the strain gauge is bonded deforms, the measured resistance of the strain gauge changes. This resistance change is related to the strain experienced by the material (Figliola and Beasley, 2011). As strain gauges are only able to measure deformation at the point to which they are bonded, it is

common for multiple strain gauge rosettes to be fitted to an object in order to measure the plane strain distribution at a number of points.

Strain gauges are used in a number of applications including frequency response analyses, as part of force transducers such as load cells, determining the stress experienced by beams under loading and the measurement of RS. The strain gauge is thus one of the most versatile devices for measuring local deformations.

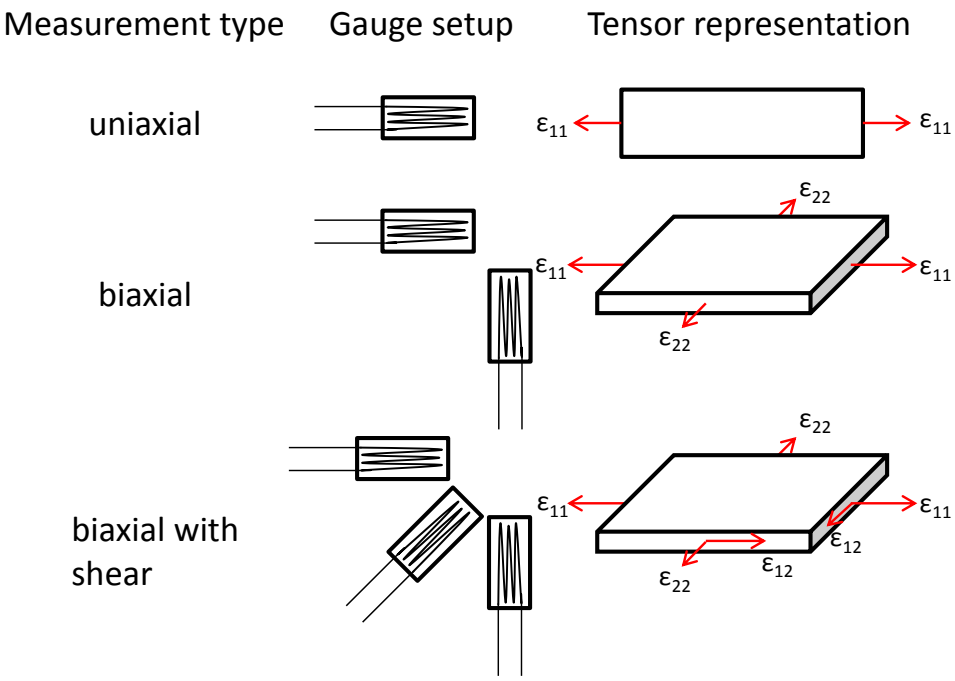

Figure 2.7 Strain gauge configurations for measuring strain components.

2.5.2 Digital Image Correlation

DIC is an image processing technique for full field strain measurement. It is capable of capturing localised displacements within a global displacement field and is thus useful as a means to capture the deformation of a specimen under complex loading (Huchzermeyer, 2017). It works by comparing images captured at different stages of a deformation testing process and tracking the change in position of defined surface features (Lord *et al.*, 2008).

DIC requires unique surface features to be present on the analysis surface for the purpose of deformation measurement. These features are commonly referred to as a speckle pattern and consist of random areas of light intensity, as can be seen in Figure 2.8. Typically, this speckle pattern is applied to the surface using an aerosol paint, however the specimen surface itself may have a sufficiently random light intensity pattern to use DIC without the need to apply an artificial pattern (Yates *et al.*, 2010a).

The analysis surface is discretised into sets of pixels, known as subsets. It is the position of the centre of each of these subsets which the correlation algorithm tracks to subpixel accuracy in order to determine the deformation experienced by the specimen when under load (Lord *et al.*, 2008). The correlation algorithm then outputs a displacement vector for each subset centre and from this the associated strain components can be calculated (Lord *et al.*, 2008).

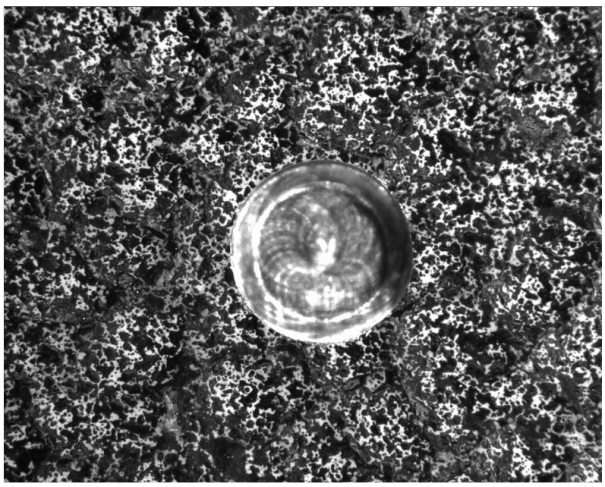

Figure 2.8 Example of a speckle pattern used to measure displacement with DIC during a hole drilling test. The circular region in the center is the drilled hole (Lord et al., 2008).

The correlation process is visually explained in Figure 2.9. A subset of features having a central point, P, and original position (x_1, x_2) undergoes some displacement and deformation. The corresponding features, in the next image, form a subset with central point, P^*, and position (x_1^*, x_2^*). This mapping from P to P^* forms the displacement fields seen in Figure 2.9. The position of P^* is found by using the speckle pattern within the region of interest (ROI). The light intensity values in the reference subset are summed over the area of the subset to obtain a unique marker value. In the next image, a region containing a corresponding light intensity value that will yield the same marker value is sought within the ROI (Yates *et al.*, 2010b). If the region is found, it is given the central point P^*. This process is repeated for each subset within the ROI in order to obtain a fully mapped displacement field.

2.5.3 Diffraction methods

Diffraction techniques such as XRD, synchrotron diffraction and neutron diffraction (ND) rely on measuring the change in the spacing of crystallographic lattice planes in order to determine elastic strain in polycrystalline materials (Park *et al.*, 2004). This is done by firing a radiation beam at the specimen and recording the patterns which are created by the diffracted radiation. Then, using

Bragg's Law of Diffraction, the inter-planar spacing of the crystal lattice can be determined (Fitzpatrick and Lodini, 2003).

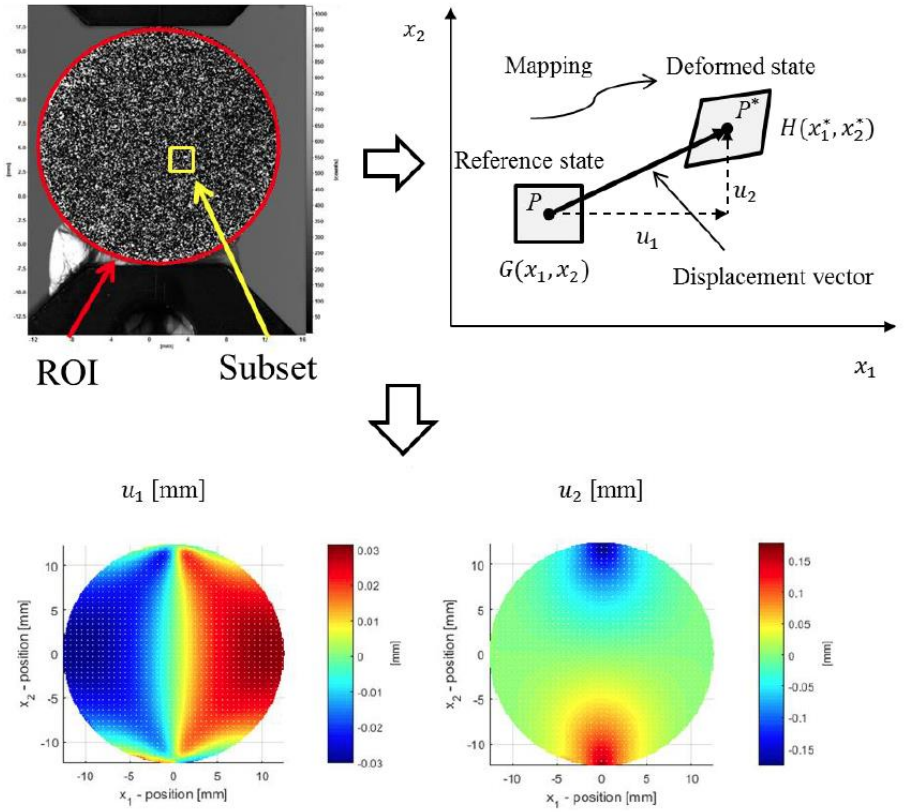

Figure 2.9 A visual explanation of the correlation process and an example of the calculated displacement map (Huchzermeyer, 2017).

To understand how Bragg's Law is used to calculate the lattice spacing, or d-spacing as it is commonly referred to, the formation of the diffraction patterns must first be understood. When an X-ray or neutron beam strikes the atoms of a specimen, the beam diffracts and is scattered in all directions. Some of these scattered rays will be in phase and will interfere constructively with one another. In Figure 2.10 ray 1 and 1a both strike atoms on the first plane of atoms and their beams are scattered in all directions. However, in directions 1' and 1a' the scattered rays are in phase with each other and thus, interfere constructively. This constructive interference occurs due to the two beams having the same path length between their wave fronts, XX' and YY'. The constructive interference occurs for all other rays that strike the first atomic plane and that are scattered to have a path parallel to 1' (Fitzpatrick et al., 2005). This constructive interference results in an intensity peak, known as a diffraction peak, being detected at the diffraction angle, θ, which is the angle between the incident beam and the atomic plane. This is also referred to as the half Bragg angle.

Rays scattered from atoms in other planes can also interfere constructively with those scattered from the first plane. If ray 2 is to constructively interfere with ray 1, the path difference, from Figure 2.10, between the wave fronts can be expressed as:

$$ML + LN = 2d' \sin\theta, \tag{2.6}$$

where *d'* is the inter-planar spacing between the first and second atomic planes and *ML* + *LN* is the difference in path length between ray 1 and ray 2 (Fitzpatrick *et al.*, 2005).

The diffracted rays, 1' and 2', can only be in phase if the path difference is an integer multiple of the wavelength of the radiation used. This is what forms the basis for Bragg's Law of diffraction, which relates the spacing between atomic planes, *d'*, to the radiation wavelength, λ, and angle of diffraction, θ (Fitzpatrick *et al.*, 2005). Bragg's Law is mathematically described by Equation (2.7)

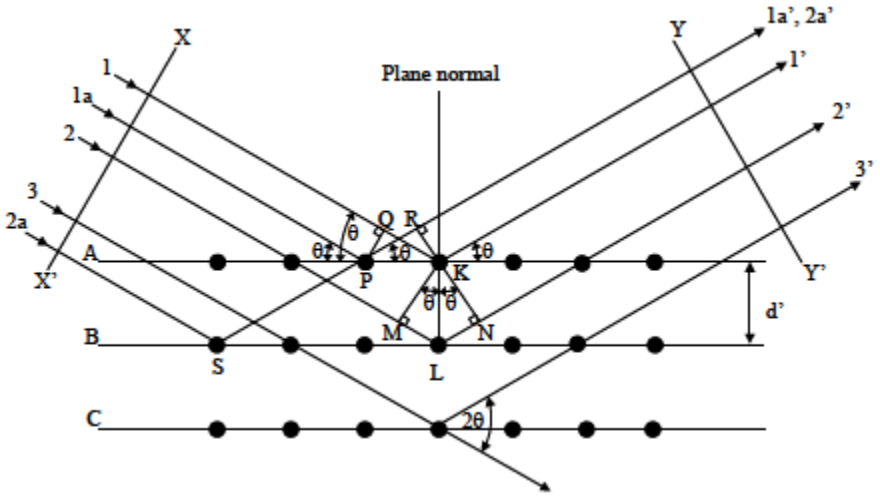

Figure 2.10 Diffraction of X-rays by a crystal lattice (Fitzpatrick et al., 2005).

$$n\lambda = 2d' \sin\theta, \tag{2.7}$$

Where *n* is an integer, λ is the wavelength of the radiation and θ is the half Bragg angle. Since the value of λ is known and the angle θ can be measured, the value of *d'* can be calculated (Fitzpatrick and Lodini, 2003).

The use of the highest possible 2θ angle is desirable as this results in the largest peak shift of the diffraction pattern (BSI, 2008). The 2θ angle is also chosen to ensure that adjacent diffraction peaks are far enough apart that they do not overlap each other and cause distortion in the measurements.

Figure 2.11 shows the coordinate system used for the diffraction techniques. The angles used are (Fitzpatrick *et al.*, 2005):

- 2θ – The Bragg angle between the incident and diffracted beams.
- ω – The angle between the incident beam and the sample surface.
- ϕ – The angle of rotation of the sample about its surface normal.
- χ – A rotation in the plane normal to that in which ω and 2θ lie.
- ψ – The angle through which the sample is tilted in the $\sin^2\psi$ method. Measured between the diffraction plane normal and the specimen normal.

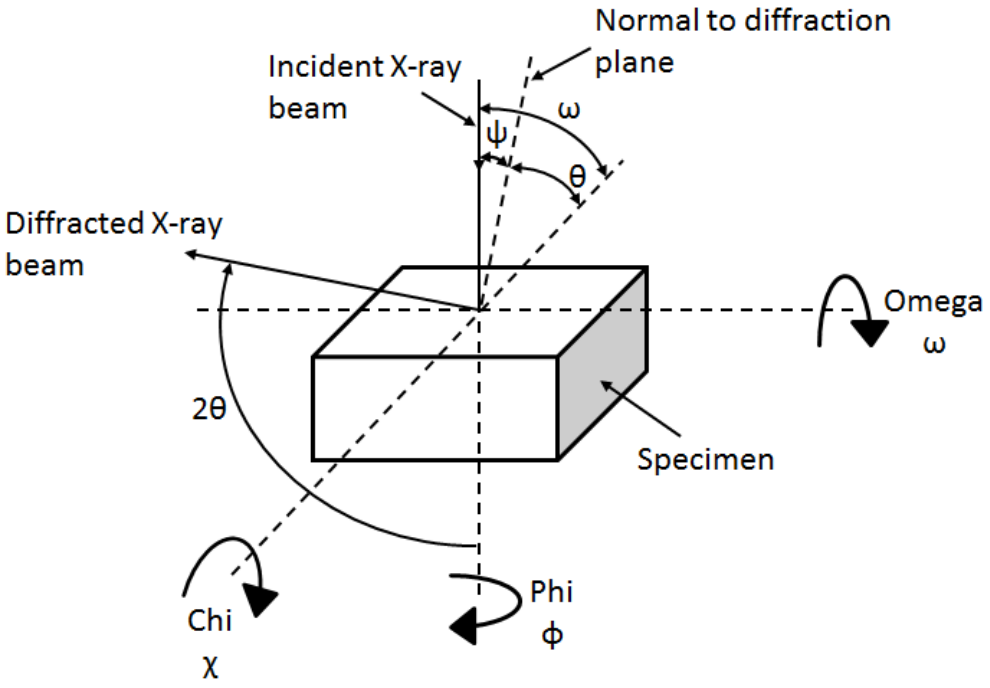

Figure 2.11 Diagram of the axes and angles used for XRD analysis (Fitzpatrick et al., 2005).

These axes are independent of the coordinate system of the body being analysed (Fitzpatrick and Lodini, 2003). However, the angle of rotation about these axes can be linked to a coordinate system. As an example, the angle $\phi = 0°$ can be aligned with the *x*-axis and the angle $\omega = 90°$ can be aligned with the *z*-axis in order to fix the diffraction coordinate system to the specimen coordinate system. This orientates the angular notation for diffraction measurement within the Cartesian coordinate system. In Figure 2.11 the incident beam strikes the

specimen perpendicularly to its surface; however, in practice the incident beam can strike the surface at any combination of angles ϕ, ω or χ.

Strain measurements are performed by rotating the beam through an arc around the specimen in order to determine the location of the diffraction peaks. The location of these peaks is dependent on the radiation wavelength used and the inter-planar spacing of the material as shown in Equation (2.7). By altering either of these, the peak locations can be changed (Fitzpatrick *et al.*, 2005). It is thus possible to determine the lattice strain present in a material using a constant radiation wavelength and comparing the peak locations of strain free material to strained material. The general strain equation used for diffraction techniques is:

$$\varepsilon_{\psi} = \frac{d_{\phi\psi} - d_0}{d_0}, \tag{2.8}$$

where ε_{ψ} is the strain in the directions defined by angle ψ (Psi), $d_{\phi\psi}$ is the inter-planar spacing in the direction defined by angles ϕ (Phi) and ψ and d_0 is the strain free inter-planar spacing (Fitzpatrick *et al.*, 2005).

The strain components that can be measured are dependent on the technique used. Due to the low penetration of XRD into many engineering materials, it is considered to be a surface stress measurement technique (Fitzpatrick *et al.*, 2005). As a result, the measurements are typically performed using the plane stress assumption explained in Section 2.2 . Thus, the stress tensor has three components as shown in Equation (2.4) and the strain tensor produced has four components as shown in Equation (2.5).

ND is capable of greater penetration depths into engineering materials than XRD. In iron, the penetration depth of ND is 20 000 times more than XRD (Stacey *et al.*, 1985). As a result, ND can measure all strain components within a body and is capable of constructing a full stress tensor, as shown in Equation (2.2). In order to do this, lattice spacing measurements are required in six orientations to calculate the six strain components using Equation (2.9) (Park *et al.*, 2004; Fitzpatrick and Lodini, 2003). However, if the principal directions are known, or if the specimen is under plane stress conditions, the stress tensor reduces to three components and as such only three orthogonal measurements are required (Park *et al.*, 2004).

$$\begin{aligned}\varepsilon_{\phi\psi} = \frac{d_{\phi\psi} - d_0}{d_0} = {} & \varepsilon_{11}\cos^2\phi\sin^2\psi + \varepsilon_{22}\sin^2\phi\sin^2\psi + \\ & \varepsilon_{33}\cos^2\psi + \varepsilon_{12}\sin 2\phi\sin^2\psi + \varepsilon_{13}\cos\phi\sin 2\psi + \\ & \varepsilon_{23}\sin\phi\sin 2\psi,\end{aligned} \tag{2.9}$$

where $\varepsilon_{\phi\psi}$ is the lattice strain in the direction defined by angles ϕ and ψ and ε_{ii} and ε_{ij} are the six strain components, measured in the crystal reference system (*hkl*), required to produce a full strain tensor (de Oliveira *et al.*, 2006). These components can be converted to the specimen coordinate system using the appropriate rotation matrix.

Once the six components of the strain tensor have been determined, the stress tensor can be calculated using Hooke's Law. Equation (2.10) is typically used for converting the strain tensor to a stress tensor (Fitzpatrick and Lodini, 2003).

$$\sigma_{ij} = \frac{1}{(1/2)S_2}\left[\varepsilon_{ij} - \delta_{ij}\frac{S_1}{(1/2)S_2 + 3S_1}\varepsilon_{ii}\right], \tag{2.10}$$

where σ_{ij} is the stress component being calculated, ε_{ij} is the corresponding strain component δ_{ij} is the Kronecker delta coefficient ($\delta_{ij} = 1$ if $i = j$ and $\delta_{ij} = 0$ if $i \neq j$), ε_{ii} is a normal strain component and S_1 and $½S_2$ are the diffraction elastic coefficients in the chosen family of planes.

Equation (2.10) is simplified to Equation (2.11) in the case where the principal directions are known and measurements are performed in these directions (Park *et al.*, 2004).

$$\sigma_i = \frac{1}{1/2\, S_2}\left[\varepsilon_i - \frac{S_1}{1/2\, S_2 + 3S_1}\sum_{i=1}^{3}\varepsilon_i\right], \tag{2.11}$$

where, σ_i and ε_i is the stress and strain, respectively, in the three principal directions.

A further method of converting the measured strain to stress, known as the $\sin^2\psi$ method[2], is commonly used with XRD (Fitzpatrick *et al.*, 2005). This method uses the plane stress assumption to estimate the stress free inter-planar spacing as the spacing measured normal to the surface, hence $\psi = 0°$ (de Oliveira *et al.*, 2006). A number of measurements are taken at various ψ angles for a single ϕ angle. The measured d-spacing is then plotted versus the value of $\sin^2\psi$. Typically, for isotropic materials, this plot can be fitted with a linear curve. The gradient of the fitted curve corresponds to the lattice strain at the particular ϕ angle. The stress in the direction of ϕ can then be calculated by:

$$\sigma_\phi = \left(\frac{E}{1+\nu}\right)m, \tag{2.12}$$

Where σ_ϕ is the stress in the ϕ direction analysed, E is the Young's Modulus of the material, ν is the Poisson's Ratio and m is the gradient of the d' vs. $\sin^2\psi$ curve (Fitzpatrick *et al.*, 2005).

For further information on how diffraction is used to measure lattice strain and RS, the reader is advised to consult Fitzpatrick and Lodini (2003), Fitzpatrick, et al.(2005) and BS EN 15305 standard (BSI, 2008).

[2] A detailed description of how the $\sin^2\psi$ method is used to calculate stress from the measured lattice spacing is presented in Appendix A

2.6 State of the art in RS measurement of SLM produced components

This section gives a brief overview of some of the research that has been previously conducted on RS development in SLM. The papers can be grouped according to the measurement technique employed to determine RS.

- The hole-drilling method with strain gauges
  - Knowles, *et al.* (2012)
  - Casavola, *et al.* (2009)
- The contour method
  - Vrancken, *et al.* (2014)
  - Wu, *et al.* (2014)
- The crack compliance method with strain gauges
  - Mercelis and Kruth (2006)
- The beam deflection method with strain gauges
  - Shiomi, *et al.* (2004)
  - Thöne, *et al.* (2012)
- X-ray diffraction
  - Yadroitsev and Yadroitsava (2015)
  - de Oliveira, *et al.* (2006)
- Neutron diffraction
  - Zaeh and Branner (2009)
  - Wu, *et al.* (2014)
- Numerical modelling
  - Parry, *et al.* (2016)
  - Van Belle, *et al.* (2013)

Research that has been conducted using the hole drilling method and crack compliance method has produced information on the stress distribution near the specimen surface. However, due to the depth resolution of these techniques they have not been able to resolve stresses below the macro-scale. Both the beam deflection method and contour method are destructive methods that produce qualitative results of the stress present at discrete planes through the specimen. The studies that have employed numerical modelling have been used to simulate the development of RS during the build process and give some insight into how the stress distribution is generated. However, these results should be used qualitatively as many assumptions are made that do not represent the physical

process. The research utilizing diffraction methods has been able to produce the most relevant quantitative results. The volumetric stress distribution has been measured as well as the near surface stress distribution using ND and XRD. Furthermore, an understanding of the directionality of the stresses has been gained through the use of XRD analyses.

The three papers underlined in the above list are discussed in more detail below. These papers were selected for further investigation as they were deemed to be most relevant to the research presented in this document and give the most concise summary of the methods for determining RS as well how the stress is affected by various build parameters.

2.6.1 Casavola, Campanelli & Pappalettere (2009)

This paper was a preliminary investigation into the distribution of RS in steel components made by SLM. The material used was AISI Marage 300 steel and the researchers made use of the hole drilling method in order to measure the RS present in the samples once they had been removed from the base plate.

Two aspects that were investigated: the influence on the component size (thickness) and the position on the base plate in which it was grown. Test specimens in the form of disks with a diameter of 35 mm were manufactured with four different thicknesses at three positions on the base plate, shown in Figure 2.12. The specimens were manufactured using a layer thickness of 30 μm and a laser scanning strategy that divided the build layer into 5 mm x 5 mm square sectors and then randomly melted each sector.

The researchers indicate that in order to reduce RS the heat generated by the laser should be conducted away from the site of the melt pool as rapidly as possible and the build-up of heat should be avoided. It is because of this that they believed that the location of the specimen on the base plate may play a role in the build-up of RS. Table 2.1 shows the build parameters used for the production of the specimens and the resultant physical properties of the specimens.

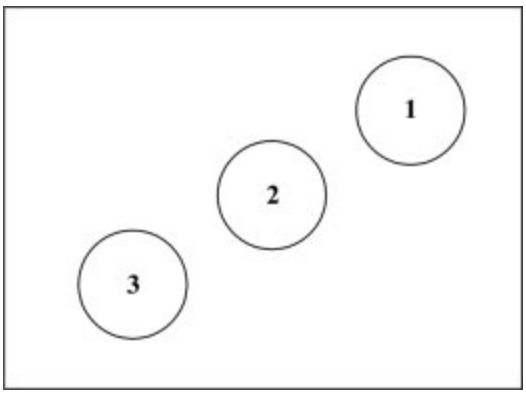

Figure 2.12 Build positions on the base plate.

A Residual Stess Analyser (RESTAN) automatic hole drilling machine from SINT Technology was used to measure the RS in the samples in increments ranging from 33 μm using a test methodology in accordance with ASTM E837-00. The cutter used produced a hole of ~2 mm in diameter.

Table 2.1 Build parameters and physical properties for Casavola specimens.

Laser Power (W)	Scan Velocity (mm/s)	Energy Density (J/mm^2)	Porosity (%)	Hardness (HRC)	Elongation at Break (%)
100	180	2.78	0.01	34	7.6

In all of the tests performed it was found that the stress near the free surface was tensile and reduced rapidly as the hole depth was increased. It was found that the material remains in tensile stress up to around 1.5 mm from the free surface and in material deeper than this there appeared to be some amount of thermal stress relief having occurred. It was found that the thicker samples displayed higher stress values. The researchers noted that specimens printed at positions 1 and 2 showed the lowest values of RS, but could only give a sufficient explanation for this for position 2 which is directly below the laser source and thus has the best configuration of molten and re-solidified zones due to the orthogonality of the scan lines.

The researchers concluded that high tensile stresses occur at the top free surface and rapidly decrease into the body of the sample regardless of the build position or sample thickness. However it was found that thicker samples displayed a higher stress magnitude and the stress reduction gradient is lower in the thicker samples. Lastly the researchers concluded that the position at which the specimen is built on the build platform does play a role in the amount of RS present in the material, however no clear explanation for why this is the case was given.

2.6.2 Yadroitsev & Yadroitsava (2015)

This research investigated the propagation of RS in SLM Ti64 and stainless steel 316L and how the track pattern used can influence this RS.

The steel samples were built on a Phenix PM100 SLM system and the Ti64 samples were built on a EOSINT M280 SLM machine. The machine parameters used for the production of both materials can be seen in Table 2.2. The steel powder was obtained from Sandvik Osprey Ltd and TLS Technik GmbH was the supplier of the Ti64 powder. The specimen build parameters as well as the powder size distribution are shown in Table 2.3. A unidirectional scanning strategy was used for the steel specimens and a rotated raster scan vector strategy was used for the titanium specimens, with scan vectors being inclined by 45° from the previous layer for each layer added.

RS testing was performed using XRD, Table 2.4 shows the parameters used for the scans of each material as well as the coefficients used for the calculation of stress values from the measured d-spacing.

Table 2.2 Machine build parameters for SS 316L and Ti64 specimens.

Material	Laser Power (W)	Hatch Spacing (µm)	Scan Speed (mm/s)	Layer thickness (µm)
SS 316 L	50	70	100	50
Ti64	150	100	1200	30

Table 2.3 Powder size distribution and specifications for SS 316 L and Ti64 specimens.

Material	Powder Size (µm)	Build Dimensions W x H (mm)	Number of Layers	Substrate Thickness (mm)
SS 316 L	3 - 27.5	3 x 3	1, 5, 25	12
Ti64	12 - 41	5 x 10	1, 2, 4, 7, 11, 46	20

The results obtained showed that the normal stresses in the steel sample were entirely tensile. Stress values in the direction parallel to the scan vector were found to be ~1.2-1.7 times greater than the stress values in the direction perpendicular to the scan vector. In some cases the stress in the direction parallel to the scan vector exceeded the yield strength and approached the UTS of the wrought material. Similarly, the stress measured in the Ti64 samples showed that the maximum stress in the surface layers occurred in the direction parallel to the scan vector and was tensile. In this case the stress in the parallel direction was around double the magnitude of the stress in the perpendicular direction. The stress in the Ti64 samples was found to increase in magnitude with an increase in layers added.

Table 2.4 XRD parameters used for RS analysis of SS 316 L and Ti64 samples.

Material	Source	Accelerating voltage (kV)	Beam current (mA)	Spot diameter (mm)	Lattice plane {*hkl*}	½S_2 / S_1 (x10^{-6} MPa^{-1})
SS 316L	MnKα	12	4	1	{311}	7.14 / -1.2
Ti-6Al-4V	CuKα	25	4	3	{213}	11.89 / -2.83

The reason for this alignment of maximum stress with the scan vector is that a solidification front forms along the scan vector and is aligned perpendicularly to the direction of the scan line. The maximum stress direction is oriented perpendicularly to this solidification front and thus parallel to the scan vector in single-track depositions. By overlapping the scan tracks the direction of this solidification front is tilted and as a result, so is the direction of the maximum principle stress. The researchers refer to a study by Gusarov *et al.* (2013) that showed that the stress in the direction parallel to the scan vector is approximately double that of the stress in the perpendicular direction regardless of whether the scanning direction is changed per layer. This means that rotation of the scanning vectors results only in the stress becoming more homogenous with direction rather than reducing the actual magnitude of the stress.

The stresses near the surface of the Ti64 samples were much higher than for the steel samples. This is partly due to the superior mechanical and thermal properties of the Ti64 and partly due to the higher energy input needed to melt the Ti64 powder. The study concluded that RS tends to develop preferentially in the direction of the scan vector, with the magnitude in that direction being nearly double that of the magnitude in the perpendicular direction. The RS in the steel samples was also found to fluctuate greatly from layer to layer, showing an oscillatory trend.

2.6.3 Parry, Ashcroft & Wildman (2016)

This study focused on the use of thermo-mechanical modeling in order to simulate the generation of RS in SLM and how it is influenced by the laser scan strategy used. This study uses coupled thermo-mechanical FE modeling in order to investigate the influence of the temperature history, resulting from the chosen scan strategy and spot size, on the development of RS.

The researchers used MSC Marc to develop the coupled model to simulate the manufacture of SLM Ti-6Al-4V on a Realizer SLM-50 machine. The simulation

attempts to directly imitate the full machine build file in order to directly compare the simulation results with experimentally measured results.

The simulation assumed three possible phases for the material – powder, liquid and solid. These states are important in order to use the correct material properties for each step in the manufacturing process. All of the relevant heat transfer coefficients were independently measured through experimental analysis of the material in its powder, liquid and solid forms.

The change from powder to liquid was defined as unidirectional, whereas the change from liquid to solid was defined as bi-directional meaning that re-melting is allowed to occur in the model. Whenever the material is in the liquid phase all stress within the material is reduced to zero in order to simulate the zero stress state of a stationary liquid.

An elasto-plastic constitutive model was used for the analysis as the real building process produces both elastic and plastic strain in the component. Due to the scales involved a small strain and small deformation formulation was used. The model accounts for three types of strain: elastic strain, plastic strain and thermal strain; using superposition these strain values are what is used by the analysis to calculate the stress in the model.

The study investigated the influence of the laser scan strategy by using two simple strategies: a unidirectional (raster style) strategy and an alternating (meander style) strategy, these strategies are depicted in Figure 2.13. For each layer added the central hatched region is first scanned, followed by the perimeter. As both strategies take an equivalent time in order to complete a layer, they can be directly compared.

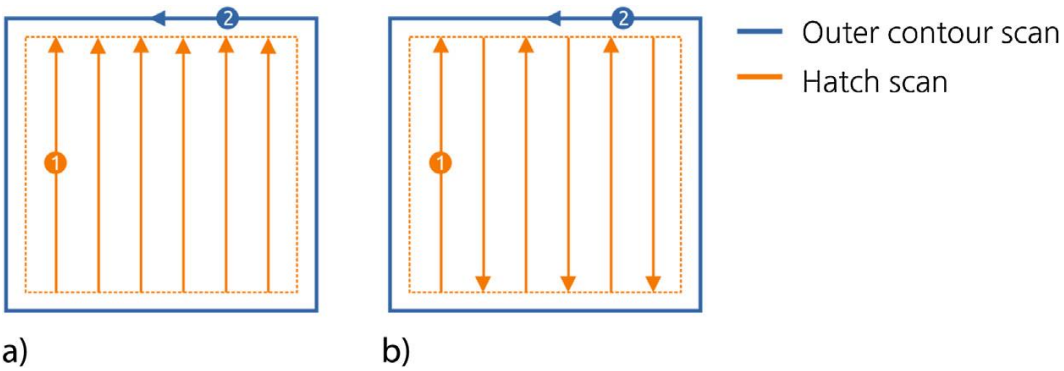

Figure 2.13 Scanning strategies used by Parry: a) raster style and b) meander style.

The thermal model was validated by comparing the size of the molten area in the simulation to that produced on a Realizer SLM 50 using the same scanning parameters. A single layer of 3 mm x 3 mm was formed and micrographs were

taken of the scan tracks. The micrographs show a track width of 104 µm - 107 µm, whereas the simulation estimated a melted track of ~140 µm. Taking the influence of re-melting and overlapping of the adjacent tracks into account, the researchers estimated a variation of ~14% between the melt pool in the simulation and in the real world test. This error was sufficiently small for the material and thermal models to be used with confidence. Due to the difference in thermal conductivity between the powder and the solidified region, the melt pool in the simulation is not symmetric, tending to form preferentially towards the previously scanned region.

By inspecting the stress formation during the simulation of a single track being scanned, it was found that the stress in the longitudinal direction is generated as the contraction of the cooling material behind the melt pool is inhibited by previously solidified material. The stress that forms in the transverse direction is lower in magnitude as there is a lack of solid material to inhibit the contraction in this direction. With the addition of further scan transverse stress tends to accumulate due to the solid material now present to inhibit expansion and contraction in the transverse direction.

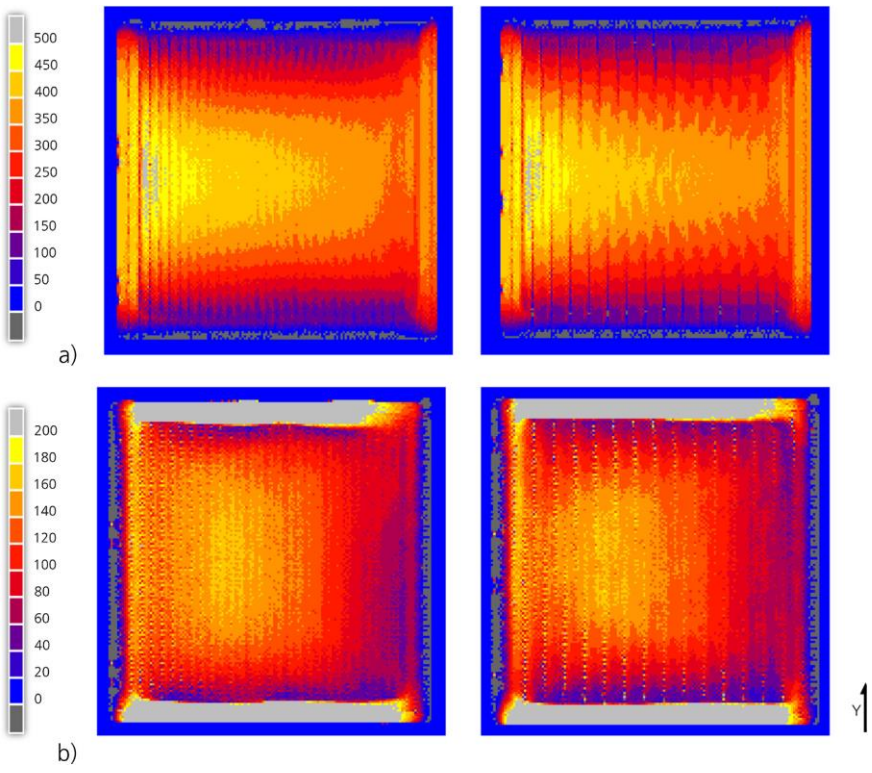

Figure 2.14 Normal stresses in MPa in a) longitudinal and b) transversal directions for raster strategy (left) and meander strategy (right). The scanning starts at the bottom left corner.

It was found that the stress distribution was dominated by the longitudinal stress, with the highest magnitudes being found centrally along each scan line. The longitudinal stress also became increasingly dominant as the size of the model increased. The average magnitude of the longitudinal stress also appeared to reduce from the first scan line to the last. This can be seen in Figure 2.14, which shows the simulated stress distribution in a single layer for the unidirectional and alternating scan strategies. This variation in stress magnitude was attributed to the lower temperature gradients that exist adjacent to the melt pool as more scan tracks are added.

It was found that large areas of the scanned region remain above the superplastic temperature for smaller specimen sizes and that, with superplastic forming, the RS in SLM Ti-6Al-4V layers can be minimized. As the part size increases, there is a lower percentage of the material above the superplastic temperature and this allows RS to accumulate – it is for this reason that larger components tend to experience higher levels of RS than smaller ones. It was also determined that as the length of the scan vector is increased, so does the stress present in the longitudinal direction, thus decreasing the scan path lengths would also help to reduce the amount of RS that accumulates in SLM built specimens.

3 Review of RS measurement techniques

In this section, a review of the proposed stress measurement techniques will be presented. The review will take into account the capabilities of each of the measurement techniques in terms of the measurement scale achievable, the assumptions made about the stress measurements and the techniques applicability to measuring RS in SLM produced Ti64.

The scale of stress that can be measured is an important factor in judging the applicability of a method to the measurement of RS in SLM produced Ti64. As mentioned in Section 1.2 and 2.4, the RS resulting from the SLM build process occurs at two scales of major interest – the part scale and the layer scale. As such, selected measurement techniques should be capable of resolving stress at both of these scales or performing measurements at one scale in such a way that measurements at the other scale are still possible. Hence, non-destructive testing methods have a greater applicability to stress measurement in SLM than destructive testing methods.

3.1 Strain gauges

Strain gauges are the most widely used means of quantifying stress. They are versatile and have a wide range of applications. When applied to the quantification of RS, strain gauges are typically used in conjunction with a destructive or semi-destructive form of stress relaxation machining. Stress

relaxation methods such as hole drilling, slot cutting and the curvature method involve the mechanical removal of stressed material from a body (Withers and Bhadeshia, 2001b). This results in local deformation at the site of the material removal as the remaining material attains a new state of equilibrium. This is shown in Figure 3.1 where a hole has been drilled into a stressed material. The blue arrows indicate the traction forces required to return the deformed hole back to its original geometry. Thus, they represent the opposition to the traction forces removed from the material. If strain gauges are fixed to the surface near the site of material removal, the resultant deformation can be measured and the magnitude of the relaxed stress can be calculated.

3.1.1 Stress scale measurable

As a result of the physics which govern the functionality of strain gauges, they are able to resolve deformations that occur at the scale of the gauge, which is typically a few square millimeters. Thus, Type I stress measurements can be performed using strain gauges in conjunction with an appropriate stress relaxation method. Some commercially available strain gauges are capable of resolving strains as low as 1 pε (Figliola and Beasley, 2011). This corresponds to a stress resolution of ~0.12 Pa in Ti64. This high sensitivity means that strain gauges may be used in applications where the deformation resulting from the application or relaxation of low stress magnitudes can still be detected and the stress resolved.

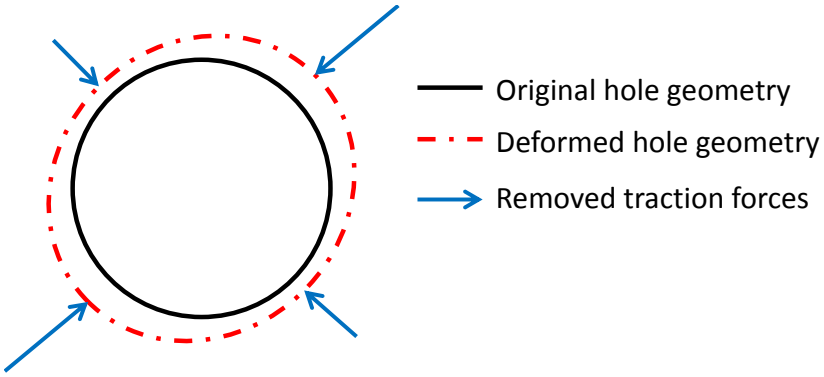

Figure 3.1 The removal of traction forces results in deformation near the removal site.

Commercial hole drilling machines have a depth resolution of ~30 µm, which is on the scale of a single build layer. In order to perform the appropriate stress profiling, a depth resolution of at most 10 µm is required if the stress distribution is assumed to be parabolic and at most 7.5 µm if it is assumed to be cubic. Wire EDM has the ability to perform milling steps to an accuracy of 0.1 µm. However, the setup required to realise this level of accuracy across the full cut surface makes the practical depth resolution lower (Albert, 2001). Thus, it is the stress

relaxation methods available that limit the application of strain gauges for measuring the RS distribution at the layer scale.

3.1.2 Assumptions and stress measurement

As mentioned in Section 2.5.1, strain gauges are capable of measuring only displacements that occur in plane and in the direction of the strain gauge. Through the use of a strain gauge rosette the displacement in a number of directions can be measured; however, the measurements remain in-plane. Thus, for all stress calculations performed using strain gauges, a plane stress assumption is made the resultant stress element is as shown in Figure 3.2 (Group, 2010). When depth profiling is performed, the in plane stress components at each depth increment can be determined and used to populate the stress tensor shown in Equation (2.4).

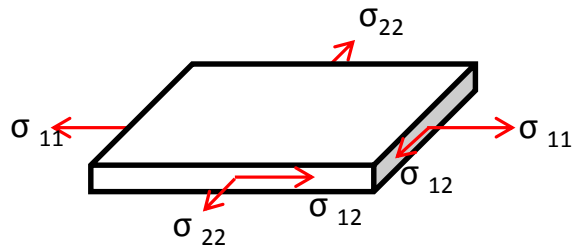

Figure 3.2 Plane stress element.

When hole drilling is used as the means to relieve stress an assumption is made about the relative hole depth required to induce full relaxation. The relative hole depth is defined as the depth of the hole divided by the diameter of the gauge circle of the strain gauge rosette used. Simulations as well as experimental testing have shown that strain relaxation saturates at a relative hole depth of 0.4 (Knowles *et al.*, 2012; ASTM International, 2001). As rosettes used for RS measurement are available in specific sizes – 2.57 mm, 5.13 mm and 10.26 mm – this imposes a fixed limit on the depth to which stresses can be resolved using a particular rosette (ASTM International, 2001). Furthermore, in order to calculate the stress tensor from the measured strain directions, a number of calibration factors must be used for particular hole to gauge diameter ratios and relative hole depth combinations. For further information on how these calculations are performed, the reader is advised to consult ASTM E837 standard for RS measurement with hole-drilling and strain-gauges.

3.1.3 Applicability to stress measurement in SLM

The use of stress relaxation methods in conjunction with strain gauges has already found application in the measurement of RS in SLM produced components (Mercelis and Kruth, 2006; Knowles *et al.*, 2012; Casavola *et al.*, 2009). However, the information that can be attained by this technique is limited to near

surface in-plane stress at the macroscale. However, with the use of the crack compliance method, stresses far removed from the surface can be extrapolated, but only in one direction (Mercelis and Kruth, 2006).

Thus, although it is a simple technique which makes use of readily available equipment, it cannot be used to provide a deeper understanding of the RS distribution present at the various scales in SLM produced Ti64. It is, however, a powerful tool for performing simple qualitative analyses that can be used to estimate the effect of certain build parameters on the maximum RS found at the top surface of a component.

3.2 X-ray diffraction

XRD is a diffraction technique that is capable of measuring stress in any polycrystalline material (Gamiet, 2015). It makes use of Bragg's Law, described in Section 2.5.3, to measure the lattice strain present near the surface of a material. XRD's ability to measure surface strain, and thus infer surface stress, makes it an ideal candidate for measuring the effects of surface treatments such as shot peening on the state of stress in the material

3.2.1 Stress scale measurable

In most engineering materials the depth of penetration achievable by XRD is on the micron scale, ranging from 2 µm – 5 µm in Titanium alloys to around 50 µm in Aluminium alloys (Fitzpatrick *et al.*, 2005). Thus, depending on the grain size of the material being tested, XRD is capable of resolving both Type I and Type II stresses. XRD has a spatial resolution of ~1 mm laterally, meaning that for fine grained materials a large number of grains are incorporated in the measurement (Withers and Bhadeshia, 2001b). If the Type I stresses tend to vary over large distances compared to the penetration depth it can be assumed that the stress measured by the XRD analysis is of Type I. However, if there are significant Type II stresses present in the material, which equilibrate over a short distance from the surface, the XRD analysis will return these stress results. Correction need to be made in order to infer the macro-stresses present in the material from these Type II stresses (Withers and Bhadeshia, 2001b).

The resolution of XRD stress measurements is dependent on the choice of detector and the Bragg peak selected. Lattice spacing measurements on the scale of 1e-6 Å[3] are possible with the use of position-sensitive detectors (PSD's) and a high Bragg angle (2θ > 120°). This results in a stress resolution of ~1 MPa in Ti64.

[3] Calculated from average standard deviation of measurements performed with XRD

Although XRD is typically used as a surface stress analysis tool, it is capable of performing depth resolved stress profiling when combined with electro-polishing (Fitzpatrick *et al.*, 2005). Electro-polishing of the surface is performed between measurement steps in order to remove surface material. This method of surface removal is used as it does not induce a change in the stress field as mechanical or EDM surface removal would (BSI, 2008). Using this technique, stress vs. depth profiles up to a depth of 1 mm can be performed (Withers and Bhadeshia, 2001b). This enhances the capabilities of XRD for application in materials which have a high X-ray absorptivity factor, thus a low X-ray penetration depth, such as Titanium alloys.

3.2.2 Assumptions and stress measurement

Due to the low penetration depth of this technique it is commonly assumed that the stress state measured is plane stress. Thus, all stresses acting perpendicular to the free surface are assumed to be zero, as shown by the stress element in Figure 3.2. Therefore XRD is able to construct the plane stress tensor described by Equation (2.4). The plane stress assumption somewhat simplifies the stress calculations as it can be assumed, without significant error, that the lattice spacing in the direction normal to the specimen surface is representative of the strain free spacing. This simplification forms the basis of the $\sin^2\psi$ method, where the d-spacing at $\psi = 0°$ is assumed to be the zero stress spacing (Fitzpatrick *et al.*, 2005).

Two methods exist for rotating the specimen in order to measure the RS using the $\sin^2\psi$ method. The ω- (Omega) method rotates the sample around the ω-axis as seen in Figure 2.11, thus changing the ω angle. The values of ψ are algebraically added to θ in order to calculate the stress values (BSI, 2008). The second method is known as the χ- (Chi) method or side inclination method. In this method the specimen is rotated about the χ-axis in Figure 2.11 and the ω angle remains constant. A special stage, called an Eulerian cradle is required in order to perform this method of XRD analysis (Fitzpatrick *et al.*, 2005). The χ-method typically leads to smaller errors than the ω-method when using negative ψ angles (BSI, 2008).

The final assumption made, specific to stress vs. depth profiling, is that the electro-polishing process does not change the stress field of the body. As explained in Section 3.1, any removal of material from a stressed body will result in the redistribution of stress to reach a new equilibrium state. Thus, using electro-polishing to remove layers of material must, by definition, alter the stress field of the body. However, this change in the stress field is typically insignificant compared to the overall stress magnitudes present in the body. Additionally, electro-polishing does not induce any surface stresses through plastic deformation and localised heating as with mechanical grinding and polishing (Fitzpatrick *et al.*, 2005).

3.2.3 Applicability to stress measurements in SLM

It has been found that the most severe stress is present at the top surface of a specimen produced through SLM and that this stress rapidly diminishes away from the surface (Casavola *et al.*, 2009; Yadroitsev and Yadroitsava, 2015; Mercelis and Kruth, 2006). As XRD is primarily a surface stress measurement technique, it is an ideal method for quantifying this region of maximal stress. With the capability of XRD - when coupled with electro-polishing - to perform high resolution stress vs. depth profiling, it is able to resolve the stress distribution through individual build layers at increments lower than 10 µm. Furthermore, XRD is a non-destructive method when used only to determine the surface stress and semi-destructive when performed in conjunction with electro-polishing. Thus, specimens analysed with XRD can have further testing performed in order to quantify the stress distribution at a larger scale without the stress field being significantly altered.

3.3 Neutron diffraction

ND is the second diffraction method of interest. Due to the high penetration of the neutron beam into engineering materials, it is often used in applications such as quantifying the RS distribution resulting from weldments.

Two limitations exist in the use of ND as a means of quantifying stress. The first is the duration required for measurements to be performed. Depending on the assumptions made and the testing setup, a measurement in a single direction, at a single point, can have a duration of between 5-10 minutes and 2-3 hours (Park *et al.*, 2004). The second limitation is the limited access to neutron diffraction facilities. As this technique requires a neutron source, typically a nuclear reactor, it is not as accessible as the other methods reviewed in this chapter. It is, however, a powerful tool for quantifying stress distribution if access is available.

3.3.1 Stress scale measurable

Unlike XRD, which averages strain measurements over a small surface area and depth, neutron diffraction utilises volumetric averaging deep within the sample to calculate the stress tensor at a point (Stacey *et al.*, 1985). Typically, gauge volumes range in size from 1 mm^3 to 10 mm^3, with larger volumes allowing for faster acquisition rates, but reducing the sensitivity of the results to steep stress gradients (Withers and Bhadeshia, 2001b; Stacey *et al.*, 1985). Due to the large gauge volumes used and its high penetration depths, ND is typically used to resolve Type I stress through the volume of a specimen (Withers and Bhadeshia, 2001b). It can, however, detect Type II stresses, which manifest in the form of diffraction peak width changes (Withers and Bhadeshia, 2001b).

Despite the ability of ND to resolve Type I stress as well as detect Type II stress, it is unable to resolve the stress distribution at the scale of SLM build layers. This

is due to the large gauge volumes used in this technique, where even the smallest usable gauge volume incorporates many build layers.

Similarly to XRD, the measurement resolution is determined by the Bragg peak selected and the detector used. Practically, ND has a lattice spacing measurement resolution of on the scale of 1e-4 Å,[4] resulting in a stress resolution of ~10 MPa in Ti64.

3.3.2 Assumptions and stress measurement

As ND uses relatively large gauge volumes compared to XRD, and can perform strain measurements deep within the specimen, it is capable of resolving the full strain tensor and in turn the full stress tensor seen in Figure 2.3. However, in order to do so, strain measurements must be performed for at least six combinations of ϕ and ψ angles to form a set of six, non-singular, equations using Equation (2.9) (Fitzpatrick and Lodini, 2003). The low acquisition rates of ND makes performing this number of measurements impracticable. By using six strain measurements per data point can result in testing durations of up to 20 days for a single specimen.

Two assumptions can be made in order to reduce the number of measurement orientations required. The first is to make a plane stress assumption, which reduces the required number of measurement orientations to three and the resulting stress tensor to that seen in Equation (2.4) (Stacey *et al.*, 1985). This assumption holds if the gauge volume is roughly equivalent to the scale of the specimen or if surface stresses are being measured.

The second assumption is that the directions of the principal stresses are known (Park *et al.*, 2004). In some applications it is possible to estimate the direction of the principal stresses through knowledge of how the stresses develop. For example, it is known that in single track SLM specimens, the maximum principal stress, σ_1, lies in the direction parallel to the direction of the laser path; σ_2, the second principal stress, lies in the direction perpendicular to the laser path and σ_3, the third principal stress, lies in the direction perpendicular to the plane formed by σ_1 and σ_2 (de Oliveira *et al.*, 2006; Parry *et al.*, 2016). In the case where the principal directions are known, three orthogonal strain measurements can be performed in these directions and the calculation of the principal stress tensor can be performed using Equation (2.11) (Park *et al.*, 2004; Stacey *et al.*, 1985).

3.3.3 Applicability to stress measurement in SLM

With the ability of ND to perform non-destructive strain measurements deep within a specimen it is in a unique position amongst the techniques available for RS analysis. Many techniques that can perform non-destructive or semi-destructive measurements are constrained to the measurement of near surface

[4] Determined from the average standard deviation of measurements performed with ND

stress, whereas the stress within the specimen can, typically, only be resolved with the use of destructive testing.

With this in mind, ND is a powerful tool for the measurement of RS in SLM produced Ti64. The technique, if used appropriately, is able to quantify the macro-stress distribution throughout the full depth of a test specimen as it has a penetration depth of ~4 mm in Titanium (Withers and Bhadeshia, 2001b). As it is a non-destructive technique it can be used synergistically with high resolution methods, such as XRD, in order to resolve not only the macro-stress distribution, but also the stress distribution through individual build layers. Furthermore, as the direction of the principle stresses present in an SLM produced component can be estimated based on the exposure strategy – provided this strategy is sufficiently basic – ND stress measurements can be expedited using the assumption described by Equation (2.11).

3.4 Digital Image Correlation

DIC is an optical displacement measurement technique that has a number of applications – from material characterisation to modal analysis (Huchzermeyer, 2017). The ability of this technique to measure strain using a set of digital images makes it highly versatile and portable. The advantages in using DIC is that full field strain measurements can be undertaken, i.e. across the entire specimen surface, compared to a single measurement point such as with strain gauges. Furthermore, DIC is scale independent and therefore allows for large – as well as microscale – measurements to be taken. The disadvantage of DIC is the low strain resolution compared to strain gauges and the requirement of high resolution, high quality optical images.

3.4.1 Stress scale measurable

DIC relies on calculating the displacement of pixels – instead of physical units of distance – making it a scale independent technique (Huchzermeyer, 2017). Thus, the measurable stress scale is limited not by the strain measurement technique, but by the manner in which images are captured.

At the macro-scale, high resolution digital image capturing devices, typically in the form of Charge Coupled Device (CCD) sensors are used to capture images as the specimen is deformed. The typical displacements measurable at this scale range from tens of microns to a few millimeters and the strains are calculated accordingly. Through the use of high magnification optical or electron microscopy, the measurable scale can be decreased drastically. Scanning electron microscopy (SEM) has been used successfully to perform DIC strain mapping at a scale of 2 µm (Sebastiani *et al.*, 2011).

DIC is, intrinsically, only limited in its measurement sensitivity by the definition of the images analysed and the surface features present. As it relies on the

displacement of pixels, which are discrete elements, both the scale and accuracy of the displacement measurable for a particular set of images is limited by the density of the pixels within an image. Displacements can typically be calculated, using interpolation functions, to within 0.01 of a pixel spacing (Da Fonseca *et al.*, 2005). Thus, images with a high pixel density are able to capture smaller displacements. Furthermore, the size of the surface speckle features present on the specimen defines the scale at which deformation can be captured. If speckles are large relative to the field of view, the techniques sensitivity to displacement is reduced. Speckle features should be at least three pixels in diameter, with a surface covering of between 25% and 50% in order to achieve optimal sensitivity and displacement resolution (Carter *et al.*, 2015; Da Fonseca *et al.*, 2005).

The achievable strain sensitivity is determined by the quality of the speckle pattern, pixel density of the images and the subset and step sized used in the processing phase. A strain resolution of down to 100 με is practically achievable with the use of DIC. This results in a stress resolution of ~12 MPa when applied to Ti64.

The scale independence means that DIC can be used to measure strain at a wider range of scales than any other strain measurement technique available. Type I stresses are routinely resolved with the use of readily available digital cameras and Type II stresses can be resolved using high magnification microscopes.

3.4.2 Assumptions and stress measurement

DIC relies on the displacement of surface features in order to measure the strain experienced by a specimen. Thus, in the application of RS measurement it is only capable of resolving near surface stress fields. The displacement measured by DIC is typically induced through the use of stress relaxation methods as described in Section 3.1 (Lord *et al.*, 2008; Winiarski and Withers, 2010; Sabate *et al.*, 2007). As such the depth to which stresses can be resolved is limited by the surface materials ability to react to stress relaxation that occurs at increasing depths below the surface. Thus, although the spatial resolution of DIC is only confined by the image capturing equipment available, the depth resolution is similar to that of strain gauge measurements as it is constrained by the laws of stress relaxation and depends on the relaxation geometry used.

Because of this depth constraint it is common practise to assume, as with strain gauges, that the measured strain is as a result of plane stress. This assumption can also be forced by the available imaging apparatus. A single-camera system, as in the case of a SEM, is only able to detect in plane displacements, thus no out of plane strain can be calculated and the use of the plane stress assumption is forced (Lord *et al.*, 2008). Thus Equation (2.5) is used without the ε_{33} component to calculate the in plane stress tensor described by Equation (2.4). In two-camera systems, which make use of stereographic imaging, the out of plane component of displacement can also be captured (Malesa *et al.*, 2015). However, due to the

depth resolution of the stress relaxation methods, a state of plane stress is still assumed and Equation (2.5) is used to calculate the three plane stress components, to a higher statistical accuracy, from the four measured strain components.

In DIC it is typically assumed that the first image in a series is representative of the specimen in its equilibrium state at zero stress. In terms of residuals stress measurements, the opposite is true. The undeformed image represents the specimen at equilibrium under its maximum surface stress state. As material is removed through the application of a stress relaxation technique, this surface stress state reduces until no further deformation can be detected. At this point the surface material is said to be fully relaxed and thus, holds no stress. The change in stress state between the first and final image must be reversed in order to determine the original stress magnitude (Winiarski and Withers, 2012).

3.4.3 Applicability to stress measurement in SLM

With the capability of DIC to measure stress at any scale at which a digital image can be taken, it is well suited to resolving the multiple stress scales present in SLM produced Ti64. Although it cannot be used to resolve stress at multiple scales within the same set of images; separate, semi-destructive, tests can be performed in order to resolve the macro-scale stress distribution in the specimen as well as the stress distribution though the build layers (Winiarski and Withers, 2012; Korsunsky *et al.*, 2010; Lord *et al.*, 2008; Wu *et al.*, 2014).

A limitation in its use at the micro-scale is the necessity to have access to a dual beam Focused Ion Beam / Scanning Electron Microscope (FIB/SEM)[5]. This specialised apparatus is not as readily accessible as other methods of measuring micro-scale stresses, such as XRD. Regardless of this limitation, the capabilities of the coupled stress relaxation – DIC method make it ideal for measuring the stress distribution resulting from the SLM production process.

3.5 Technique summary

The techniques and their capabilities presented in this chapter can be summarised by Table 3.1.

[5] For further information on FIB milling and SEM imaging, please refer to Appendix B.

Table 3.1 Summary of reviewed measurement techniques.

Technique	Measurement type	Measurement depth (mm)	Stress state assumption	Stress resolution in Ti64 (MPa)
Strain Gauge	Surface Contact Destructive	1 – 4	Plane stress	> 0.12
XRD	Surface Non-contact Non-destructive[6]	2e-6 – 5e-6[7]	Plane stress	> 1
ND	Volumetric Non-contact Non-destructive	4	Triaxial stress	> 10
DIC	Surface Non-contact Semi-destructive	limitless	Plane stress	> 12

4 Experimental methodology

Based on the review performed in Chapter 3, it was determined that the techniques most applicable to RS measurement in SLM produced Ti64 are XRD, ND and micro stress relaxation with DIC. This section will present the methodology used in each of these techniques for the purpose of RS measurement. This section will first address the procurement of the test specimens used in this study and then present a detailed look at the equipment, processes and parameters used in these techniques.

[6] Semi-destructive if coupled with electro-polishing.
[7] Up to 1 mm using XRD coupled with electro-polishing.

4.1 Specimen Procurement

The specimens used for this study were designed and built at University of Lueven's Department of Mechanical Engineering using their self-built SLM machine. The specimens were made from Ti64 powder acquired by KU Leuven from 3D Systems Layerwise; an analysis of the powder showed a particle size distribution between 5 µm and 50 µm, with 50% of the particles having a diameter of less than 34.43 µm. The build parameters that were common to all of the specimens produced are shown in Table 4.1.

Further, a shot peened, wrought, 12CrNiMo steel specimen was acquired for the purpose of verifying the results obtained by the FIB-DIC. As the specimen had a known stress distribution to a depth of 500 µm, determined using XRD and electro-polishing stress profiling, it could be used in a validation study of this non-standard technique for RS measurement (Gamiet, 2015).

Table 4.1 Build parameters common to all specimens produced.

Laser power (W)	Laser scan speed (mm/min)	Hatch spacing (µm)
250	1800	75

A total of nine specimens were produced for use in this project, each with a different combination of layer thickness and exposure. This was done to allow for the investigation of only two build parameters and the direct comparison of the influence of each. Specimens were named according to their exposure strategy and layer thickness, with the first digit referring to the exposure strategy used and the second and third digit describing the layer thickness, in µm, used to produce the specimen. A graphical description of the three exposure strategies used can be seen in Figure 4.1 along with the specimen dimensions and attached coordinate system. Table 4.2 explains the specimen naming convention used and provides a test matrix for all specimens used in this study.

Nine small specimens were also produced with parameters corresponding to each of the test specimens. These specimens were 3 x 3 10 mm in dimension and were intended to act as zero stress reference specimens. As their dimensions are small, it can be assumed that the RS generated during the build process was sufficiently relieved upon releasing them from the base plate that they are in a stress free state.

No specimen preparation, such as polishing, was performed before testing as surface preparation of this kind would result in a redistribution of the stress field; with stresses being artificially created through the plastic deformation and

temperature increase associated with grinding and polishing (Fitzpatrick *et al.*, 2005, p.31).

Table 4.2 Specimen description and testing matrix.

Specimen	Exposure strategy	Layer thickness (µm)	Surface XRD	XRD profiling	ND	FIB-DIC
130	1	30	*	*	*	
160	1	60	*	*		
190	1	90	*	*		
230	2	30	*	*	*	
260	2	60	*			
290	2	90	*		*	
330	3	30	*	*	*	
360	3	60	*			
390	3	90	*			
12CrNiMo	---	---				*

4.2 Neutron diffraction analysis

ND was used to measure the RS distribution throughout the depth of the specimens. It was possible to perform this testing non-destructively as the high energy thermal neutron beam was able to penetrate through the full depth of the test specimens.

4.2.1 Experimental setup

ND testing was performed by the NECSA using their MPISI neutron strain scanning instrument. The instrument consists of a neutron source, a sample mounting table that is able to rotate about two axes and a detector apparatus as shown in Figure 4.2. This setup allowed for measurements to be performed in any combination of angles ϕ and ψ. However, to reduce the testing time, it was assumed that the principal axes were coincident with the specimen axes. Thus, measurements were performed in three orthogonal directions corresponding to the

coordinate system attached to the specimen, as shown in Figure 4.2 and Figure 4.3.

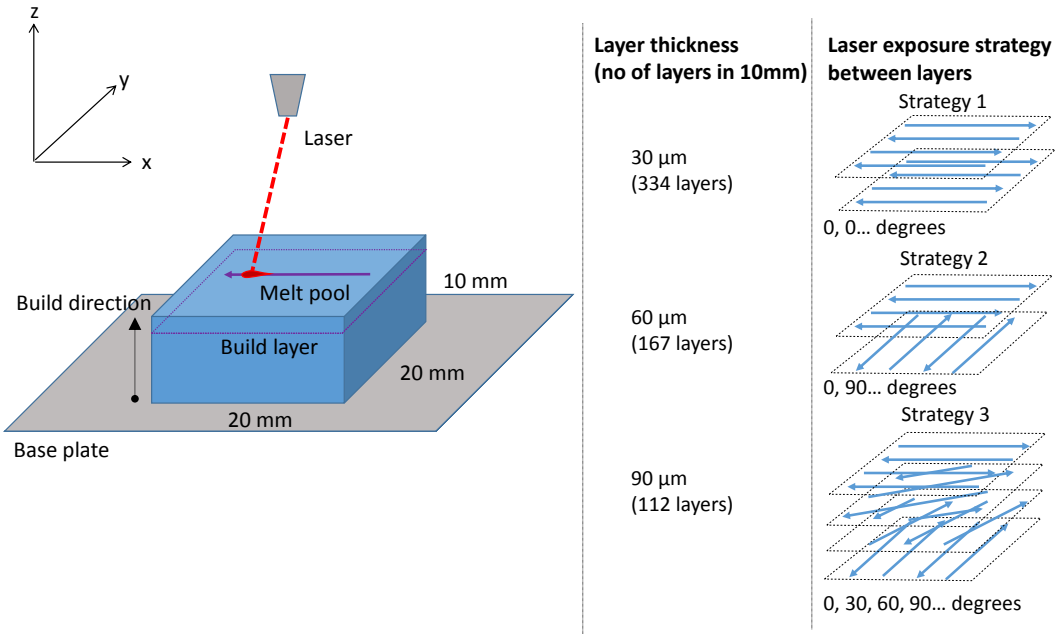

Figure 4.1 SLM produced specimen dimension, coordinate system, layer thickness and exposure strategy.

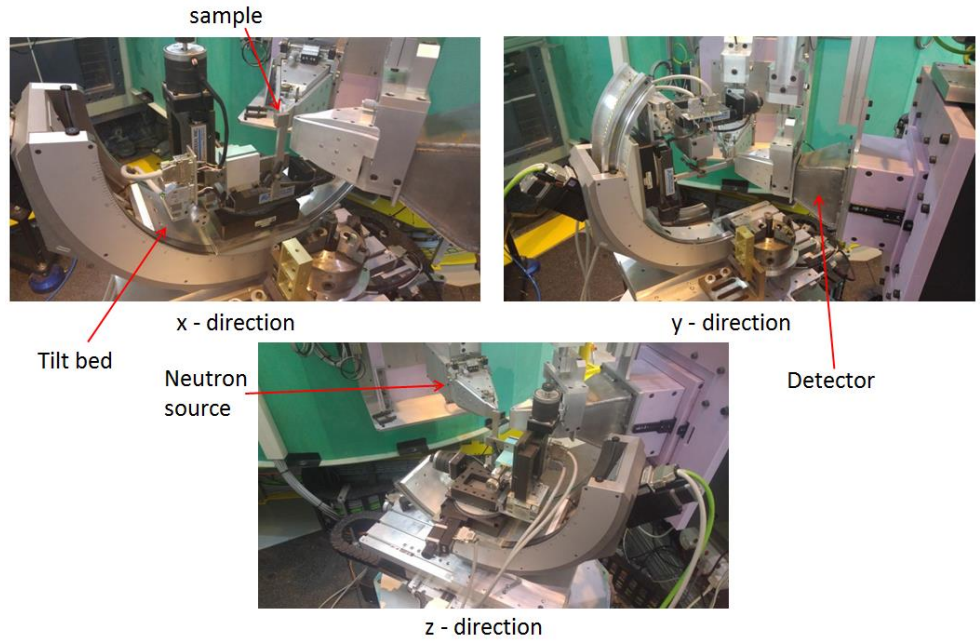

Figure 4.2 Equipment setup for performing neutron diffraction analysis.

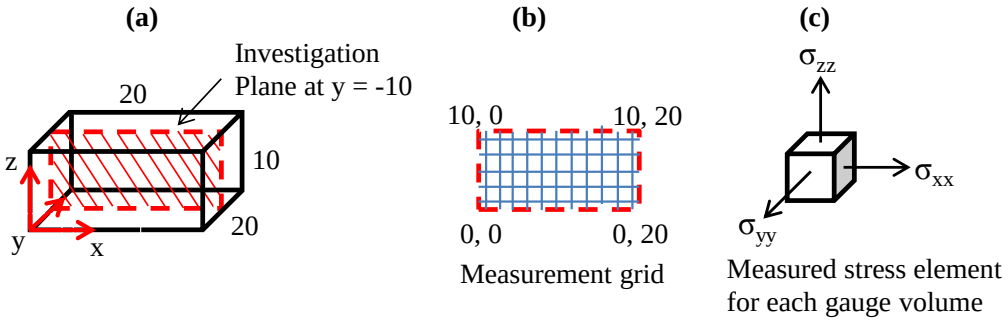

Figure 4.3 a) Reference coordinate system used for ND scans along with the location of the investigation plane, b) grid points used and c) representation of the measured stress tensor for each gauge volume.

Lattice spacing measurements were first conducted on the small specimens in order to establish the reference d-spacing to be used in the calculation of the lattice strains present in the test specimens. Due to the size of the gauge volume relative to the specimen size, it was assumed that the reference specimens were in a state of plane stress. As such, the d-spacing in the direction perpendicular to the surface was measured and set as the reference spacing for each test specimen.

As it was assumed that the stress distribution would be approximately symmetric across a surface in the *xz* plane through the centre of the specimen. Thus, measurements were taken along this cross sectional plane at y = -10 mm as shown in Figure 4.3. The plane was subdivided into a measurement grid of 5 x 11 sample points, ~2 mm apart. These points act as the centre point of each gauge volume used to determine d-spacing results. At each of these points a scan was performed using the parameters shown in Table 4.3. Despite the two assumptions used to reduce the testing duration, an average of 13 days per specimen was required in order to perform a full set of d-spacing measurements. This is primarily due to the low neutron counting rate of the SAFARI-1 reactor. For this reason, testing was performed on only four of the available specimens.

Table 4.3 Parameters used for neutron diffraction analysis.

Gauge volume (mm^3)	**ψ tilt (°)**	**Bragg peak (°)**	**Planes analysed (*hkl*)**	**Elastic coeff. S_1 (MPa^{-1} x 10^{-6})**	**Elastic coeff. S_2 (MPa^{-1} x 10^{-6})**
2 x 2 x 2	90	77.6	(301)	-2.579	10.870

4.2.2 Data Processing

The lattice strain components were calculated using the measured d-spacing of the stressed specimens and the reference specimens substituted into Equation (2.8) The three stress components of each gauge volume, seen in Figure 4.3, were then calculated using Equation (2.11), as done by Park, *et al.* (2004). According to de Oliveira, *et al.* (2006), the assumption that the principal stress direction is aligned with the laser vector holds true only for single track SLM produced specimens, whereas all of the tested specimens were multi-track specimens. As such, the data obtained from the tested specimens can only be used as qualitative results and will be considered as such.

4.3 XRD surface stress analysis

A surface stress analysis was performed at NECSA by Mr T.P. Ntsoane and Dr A.M. Venter using the XRD $\sin^2\psi$ technique. The testing followed the ω-method outlined by the BS EN 15305 standard where, at each ϕ angle, the specimen was rotated about its ω-axis to change the ψ angle (BSI, 2008).

4.3.1 Experimental setup

The analysis was performed using a Bruker's D8 Discover instrument fitted with a Vantec 500 area detector. An area detector allows for a larger section of the diffraction cone to be collected at once (Fitzpatrick *et al.*, 2005). This type of detector is primarily used for gathering information about grain size and texture, but its sensitivity to sample fluorescence means that it is not suited to performing residuals stress analyses. However, this was the detector that was available.

Measurements were performed at the central point of the top surface as shown in Figure 4.4. Measurements were performed at six ϕ orientations, namely 0°, 180°, 90°, 270°, 45° and 225°; where the ϕ angle is measured from the *x*-direction shown in Figure 4.4. At each ϕ orientation, lattice spacing measurements were performed at six ψ tilt angles. This resulted in 36 $d_{\phi\psi}$ measurements for each specimen. The stress free lattice spacing was determined according to the $\sin^2\psi$ method, where the spacing at $\psi = 0°$ is assumed to be representative of the stress free spacing.

The parameters used to perform the measurements are shown in Table 4.4. The reported penetration depth was estimated at 20 µm. However, this penetration depth is likely in error as the maximum penetration of X-rays from a Cu source into Ti-alloys is reported as ~5 µm by both Fitzpatrick, *et al.* (2005) and the BS EN 15305 standard (BSI, 2008).

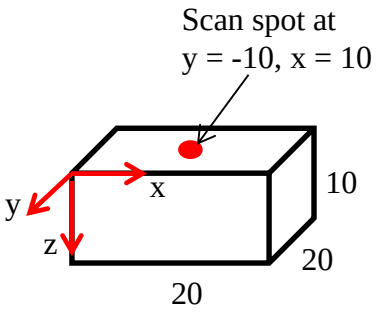

Figure 4.4 Reference coordinate system used and scan location of XRD analyses.

Table 4.4 Measurement parameters used for XRD surface stress analysis.

X-ray source	Spot diameter (mm)	ψ angles traversed (°)	Bragg peak (°)	Planes analysed (*hkl*)
Cu-Kα	0.8	0 – 50 in steps of 10	~110	(211)

4.3.2 Data processing

With the use of the $\sin^2\psi$ method, the stress in each ϕ direction was calculated using Equation (2.12). Once these stresses had been calculated, the in-plane stress tensor was calculated for each specimen using six equations of the form shown in Equation (4.1) and a least squares solution (BSI, 2008). The stress components σ_{11} and σ_{22} correspond, arbitrarily, to the normal stress in the *x* and *y* directions of the specimens and σ_{12} corresponds to the shear stress in the *xy* plane of the specimens. In the analyses performed, σ_{11} was set to correspond to σ_{xx}, σ_{22} to σ_{yy} and σ_{12} to τ_{xy}. The stress calculations were performed automatically using LEPTOS v6 data reduction and stress calculation software. This program uses, as inputs, the measured Bragg peak positions at the various ψ tilts and the corresponding diffraction elastic moduli to calculate the final stress tensor.

$$\sigma_\phi = \sigma_{11}\cos^2\phi + \sigma_{22}\sin^2\phi + \sigma_{12}\sin 2\phi. \tag{4.1}$$

4.4 XRD stress vs. depth profile analysis

This method was used to resolve the stress distribution through the top two build layers of the tested specimens. It was hypothesised that the capabilities of XRD

coupled with electro-polishing would allow for this stress distribution to be measured.

4.4.1 Experimental setup

The testing was performed by StressTech Oy, with the assistance of Mr. Juha Siiriäinen and Ms. Jenna Tarvonen. The measurements were performed on StressTech's G3R XSTRESS device using a Ti Kα X-ray source tube in accordance with the modified χ-method in the BS EN 15305 standard. In this method, the ω angle is kept constant and the specimen is tilted around its χ-axis instead (BSI, 2008). A biaxial stress state assumption was used for the calculation of the stress tensor at each depth increment. Hence, the stress calculations produced the plane stress tensor. Electro-polishing was performed incrementally using a Struers Movipol-3 electro-polishing unit with Struers Electrolyte A2 as the polishing solution. The equipment setup is shown in Figure 4.5 and the measurement parameters are shown in Table 4.5

PSD's were used as these detectors are best suited for RS analyses where good quality data is required (Fitzpatrick *et al.*, 2005). The two detectors were positioned at the chosen Bragg angle as this was the highest 2θ angle of diffraction, when using a Ti-radiation source, which would fulfil Bragg's Law of Diffraction, described in Equation (2.7).

As part of the initial setup, a powder sample was used to calibrate the distance from the sample surface to the detector. A powder with a fine particle size does not hold macroscopic stresses, or the stresses are negligibly small. Thus, the measurement instrument should detect zero stress, within a certain tolerance, when the correct working distance is found. The working distance was not reported in the results received from StressTech and as such is not reported here.

The reference lattice plane spacing for each ϕ angle, at each depth increment was determined in accordance with the $\sin^2\psi$ method where the spacing in the direction perpendicular to the surface, at $\psi = 0°$, is assumed to be representative of the stress free spacing, d_0. This method simplifies the testing procedure greatly and the error in using this simplification is usually less than 2%.

Measurements were performed at the centre point of the top surface of the samples, as shown in Figure 4.4. The measurements were taken for three ϕ angles, namely 0°, 45° and 90°. This allowed for the calculation of the three stress components for a biaxial state of stress described by the tensor in Equation (2.4). At each of the three ϕ angles, scans were performed at χ angles ranging from -45° to 0° and from 0° to 45° in two sets of seven increments. This was done to increase the number of grains that contribute to the diffraction signal (BSI, 2008). The ω angle was 90° to the specimen surface when $\chi = 0$ and was held constant for all χ tilts.

Table 4.5 Parameters used to perform XRD stress profile analysis.

Radiation wavelength (nm)	Spot diameter (mm)	Bragg angle (°)	ψ angles traversed (°)	Planes analysed (*hkl*)	Penetration depth (µm)
λ=0.27497	3	137.5	-45 – 0 & 0 – 45 in steps of 5	[110]	6

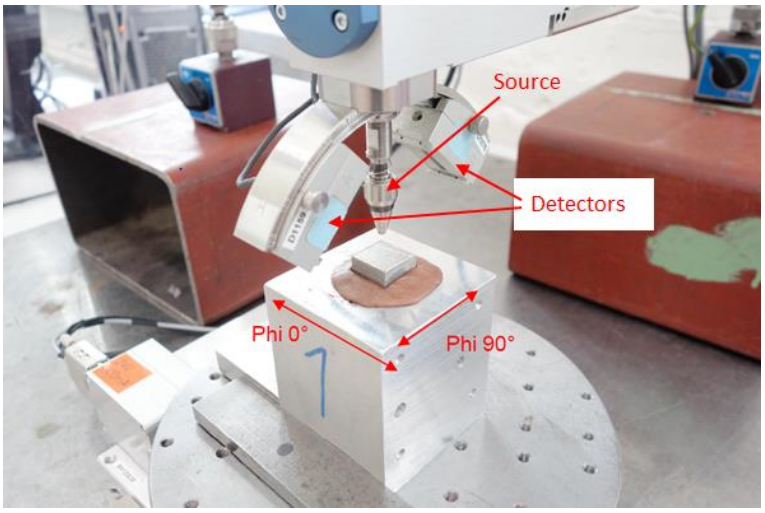

Figure 4.5 Equipment setup for XRD stress profiling. Measurement orientations are given by ϕ angles.

Once the current depth increment had been fully scanned, the surface was electro-polished to remove a layer of material. Ten depth increments were performed in the *z*-direction for each of the five specimens, with the amount of material removed between each increment being dependent on the layer thickness of the specimen. The depth increments can be seen in Table 4.6. The depths were chosen so as to allow at least five increments per build layer and penetrate at least the first two build layers, with a total number of 10 stress measurement increments. This number of measurements per layer would allow a complex stress distribution through each layer to be captured.

Table 4.6 Electro-polishing depth increments for XRD stress profiling according to layer thickness.

Layer Thickness (µm)	30	60	90
Depth Increment (µm)	7 ± 2	14 ± 3.5	20 ± 3.5

4.4.2 Data processing

The diffraction peak measured by each detector was used to calculate the peak shifts at each χ tilt. The calculated shifts at each χ tilt were then averaged and used to calculate the resultant d-spacing at each χ tilt (BSI, 2008). The set of lattice spacings measured at each of the three ϕ angle was used by the XTronic 1.9.1 software, in conjunction with the $\sin^2\psi$ method, to calculate the stress in the three ϕ directions. Since the chosen ϕ directions correspond to the *x*, *y* and *xy* directions of the specimen, the stress in these directions can be inferred immediately.

4.5 Micro stress relaxation with DIC

This section details the work performed in developing a new method of measuring the stress distribution through the depth of an SLM build layer as introduced in Section 2.4. The methodology was based on techniques used to measure stress in thin metallic films (Sebastiani *et al.*, 2011). Due to the microscopic scale of the testing, DIC was used as a virtual strain gauge with which to measure the deformations associated with the removal of stressed material. Testing was performed at Nelson Mandela University, with the assistance of Dr Johan Westraadt, at the CHRTEM lab.

4.5.1 Experimental setup

A FEI Helios NanoLab 650 Dual Beam FIB-SEM was used to perform both the milling and imaging steps. The testing used a wrought 12CrNiMo steel specimen that had undergone shot peening and had previously had the RS measured, to a depth of 500 µm, using XRD stress profiling. The SEM column was used in combination with an Ion Conversion and Electron (ICE) detector for capturing micrographs of the site of interest and the FIB column was used for material removal.

Based on literature by Sebastiani, *et al* (2011) and Korsunsky, *et al* (2009) the ring core milling method was chosen as this provides the most efficient method of surface strain relief. Furthermore, this method is able to capture a biaxial state of

stress, which is the stress state assumed for both shot peening and within an SLM build layer. Ring core milling has also been found to be least affected by the issues inherent to FIB milling, such as sputtered material deposition (Korsunsky *et al.*, 2010). In this method, an annular trench is milled around a central stub. As the depth of the trench is increased, the stub undergoes stress relaxation and its surface deforms. This deformation is measured through the use of DIC and from it the relaxed strain can be calculated.

The method followed can be broken down as follows:

1. Specimen is attached to translation stage using conductive silver paint to prevent surface charge build-up.
2. SEM imaging is used to select sight of interest (SOI).
3. Stage tilted to 52° so specimen surface is perpendicular to FIB column.
4. FIB used to mill speckle pattern into specimen surface at SOI using a white noise bitmap pattern.
5. FIB used to mill alignment markers.
6. Stage tilted to 0° so specimen surface is perpendicular to SEM column.
7. SEM used to capture reference image of SOI for DIC analysis.
8. Stage tilted to 52°, realigned with FIB column using markers and FIB is refocused on surface.
9. FIB used to mill the first ring trench increment.
10. Stage tilted to 0°, realigned with SEM column using markers and SEM is refocused on surface.
11. SEM used to capture image of first ring trench increment.
12. Step 8 – 11 is repeated until trench depth is 40% of stub diameter (Song *et al.*, 2011).
13. Perform DIC analysis on captured images to extract displacement maps.

FIB ring core milling: The use of a FIB allows for the minimization of stress relaxation methods such as hole drilling, slot milling and ring core milling. By adjusting the beam current, the rate of material removal can be adjusted to the requirements of the milling process. For the testing performed the ring trench was set to have an inner diameter of 50 μm and an outer diameter of 70 μm. The inner diameter was chosen so that maximum relaxation would occur at a trench depth of

~20 µm, which is close to the full depth of a build layer in an SLM produced specimen. The FIB parameters used to produce this trench are given in Table 4.7.

Table 4.7 FIB parameters for trench milling and speckle pattern milling.

Milling	FIB magnification (x mag)	Accelerating voltage (kV)	Beam current (A)	Depth milled (µm)
Speckle pattern	2500	30	4.3e-9	~0.15
Ring trench	2500	30	43e-9	~2

Each time the stage was tilted to 52° it was necessary to realign the FIB column with the previously milled area due to the stage drift that occurred during the tilt. In order to perform this realignment, two markers were milled into the surface at the SOI. These markers can be seen in Figure 4.6. Before each depth increment was milled, the milling pattern was realigned with these markers to ensure that the FIB removed material from the same region in each increment. This process required that images be captured using the FIB. A reduced imaging area, which excluded the speckle pattern, was used to prevent ion erosion of the speckle pattern surface.

The ring milling was performed using an outer-to-inner spiral path to reduce the deposition of ejected material onto the stub surface. The use of this method resulted in the material being ejected towards the outside of the trench, thus minimizing the change of surface features on the stub surface associated with material deposition.

SEM imaging: The SEM column was used to capture two images after each milling step had been completed using the SEM settings shown in Table 4.8. The first image was captured at a stage tilt of 52° to allow for the depth of the trench to be measured. The SEM imaging software automatically applies a tilt correction factor to the measurement to account for the aspect ratio effect of measuring on a tilted plane. The stage was then tilted to 0° and the images that are to be used for the DIC analysis are captured. Line integration was applied during the capturing of each image in order to reduce image noise. Using this method, the SEM scans a line multiple times and integrates the results in order to generate the final image. The images captured at each depth increment can be seen in Figure 8.10 and Figure 8.11.

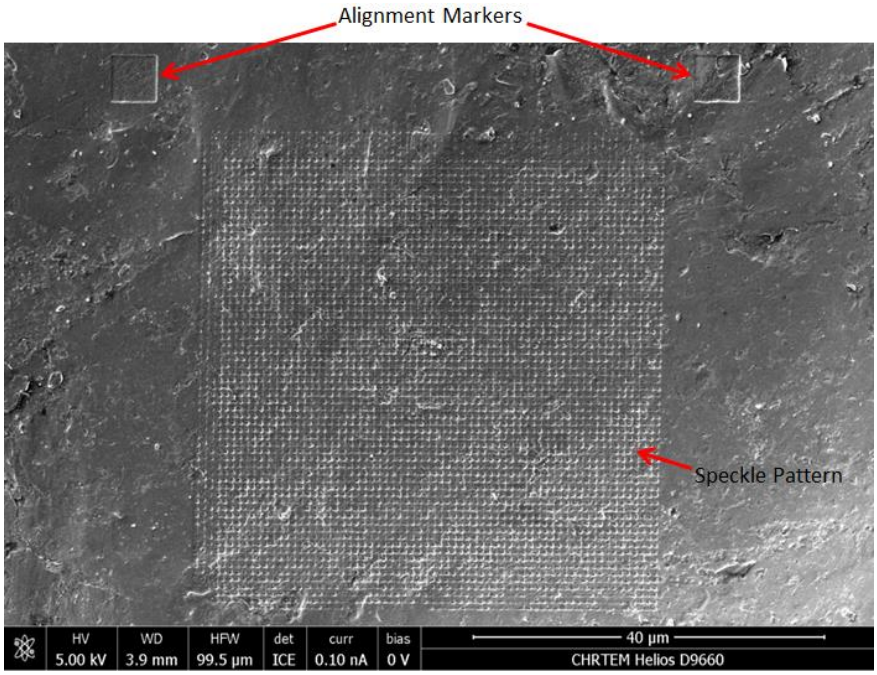

Figure 4.6 Speckle pattern milled into specimen surface, with alignment markers shown.

Table 4.8 SEM imaging settings used for capturing micrographs.

Beam Voltage (kV)	Beam Current (nA)	Resolution W x H (pixels)	Magnification	Lines Integrated
5	0.1	1536 x 1103	2500	8

Due to the stage drift that occurred during the stage tilt from 52° to 0° it was necessary to refocus and realign the SEM column before each increment image could be captured. It was also necessary to adjust the contrast of the images after each tilt. As the displacement results obtained by DIC can be affected by changes in the image focus and contrast, it was ensured that the image focus and contrast was set to the same value, respectively, for each imaging step.

DIC analysis of images: A DIC analysis was performed on the images captured by the SEM and acted as a virtual strain gauge, allowing for the surface displacements to be measured. As DIC requires a pattern of unique surface features in order to perform displacement measurements, the FIB was used to mill a pattern into the surface at the SOI using the parameters shown in Table 4.7. A 256 x 256 pixel white noise bitmap with 50% fill was used as a template to mill the speckle pattern. Due to problems with the FIB milling software, the white noise image was milled as a semi-regular grid. The milled pattern can be seen in Figure 4.6 along with the alignment markers mentioned previously. As the surface

contained pre-existing, random, features it was assumed that the semi-regular grid would result in a speckle pattern that was sufficiently unique for the purposes of the DIC analysis.

An error analysis was performed on the speckle pattern by performing rigid body shifts of the pattern using the translation stage. An image was captured after each translation using the SEM settings detailed in Table 4.8. A total of eight translations were made in the *x*- and *y*-direction. A MATLAB script was used to calculate the systematic and random error of the speckle pattern from the measured displacement fields. The average displacement measured in the *x*- and *y*-direction, respectively, was calculated over the full field and compared to the reference displacements imposed. The systematic error was calculated using:

$$e_{sys} = |\delta_{ref}| - |\delta_{DIC}|, \tag{4.2}$$

Where e_{sys} is the calculated systematic error, δ_{ref} is the reference displacement and δ_{DIC} is the displacement measured by DIC. The random error was then calculated as the standard deviation of the displacements in the *x*- and *y*-direction.

The error analysis performed on the speckle pattern produced the systematic and random error results shown in Table 4.9. As the imposed displacements were on the scale of 5e-4 mm, it follows that the relative systematic error in the *x*- and *y*-direction is on the scale of 0.2% and 13%, respectively and the random error in both directions is ~0.4%. The higher systematic error in the *y*-direction can be attributed to the use of line integration instead of image integration during the capturing of the SEM images. Line integration does not remove image noise or erroneous displacements caused by stage drift in the *y*-direction, whereas image integration would.

Table 4.9 Error analysis of speckle pattern used for DIC on FIB milled specimen.

Systematic error		**Random error**	
x-direction (mm)	**y-direction (mm)**	**x-direction (mm)**	**y-direction (mm)**
8.80362e-7	6.7408e-5	1.73e-6	2.0033e-6

The displacement of each of the captured images was calculated using LaVision DaVis ver. 8.4. A pre-processing shift correction was applied to the images in order to remove any rigid body displacements caused by SEM misalignment at each imaging step. An initial analysis of the full area of the stub was performed using the parameters shown in Table 4.10, along with the application of a smoothing and outlier filter. The large subset size reduces the noise in the calculated displacement maps by averaging the displacement of a larger number of pixels, thus reducing the influence of outliers. The small step size was used so

as to allow the square subsets to fit better to the circular analysis domain. Furthermore, increasing the overlap of subsets improves the accuracy of the results.

Table 4.10 Parameters used for DIC displacement calculations.

Subset size (pixels)	Step size (pixels)	Calculation type	Sub-pixel displacement
139	4	Relative to first	Linear interpolation

After the initial analysis had been performed, the correlation factor was calculated over the surface of the stub for each image captured. The correlation factor is a measure of how well subsets could be correlated between images. Areas close to the edge of the stub were found to have poor correlation due to the ion beam erosion and material deposition that occurred in this region, resulting in a change to the surface features. Thus, the masking region was set to include only the areas of the stub that achieved a correlation factor of 0.85(or 85%) and above. This allowed for sufficiently accurate results to be calculated without excluding too much of the information close to the edge of the stub. The analysis was then run again using this reduced mask and the parameters shown in Table 4.10. An example displacement map is shown in Figure 4.7. The full set of displacement maps can be found in Figure 8.12 to Figure 8.17.

4.5.2 Method validation

Once displacement maps were produced, the vectors for *x*- and *y*-displacements for each milling step were extracted and exported as tecplot files. Figure 4.7 shows the reference coordinate system used to describe the displacement components. A MATLAB 2017a script, found in Appendix D, was used to fit a Gaussian surface to the displacements measured in each image. This allowed for the in-plane strain components to be calculated from the gradient of the fitted surfaces. The strain components calculated for each depth increment are shown in Figure 4.8.

The method was able to capture an incremental increase in strain for each depth increment. However, as the strain does not converge to an asymptotic value at the highest depth increments, full relaxation was not achieved. Thus the trench depth at which full relaxation is achieved is higher than 40% of the stub diameter. Figure 4.8 shows that the stress at the SOI was approximately uni-axial compressive stress, with a high shear component. This high shear component is likely as a result of the shot peening treatment that was applied to the specimen. The shot peening process results in high shear stresses due to the impingement angle of the beads (Davis, 2012).

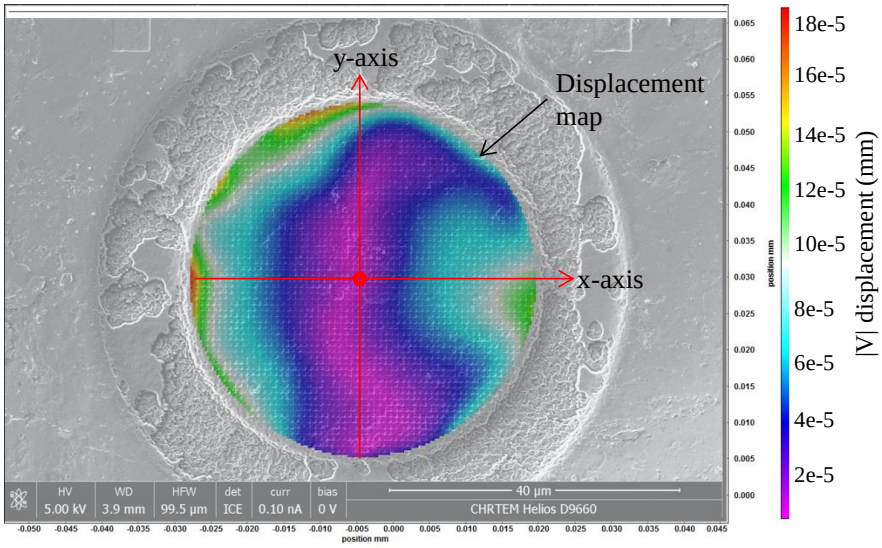

Figure 4.7 Displacement map generated for depth increment 9, a trench depth of ~18.5 µm

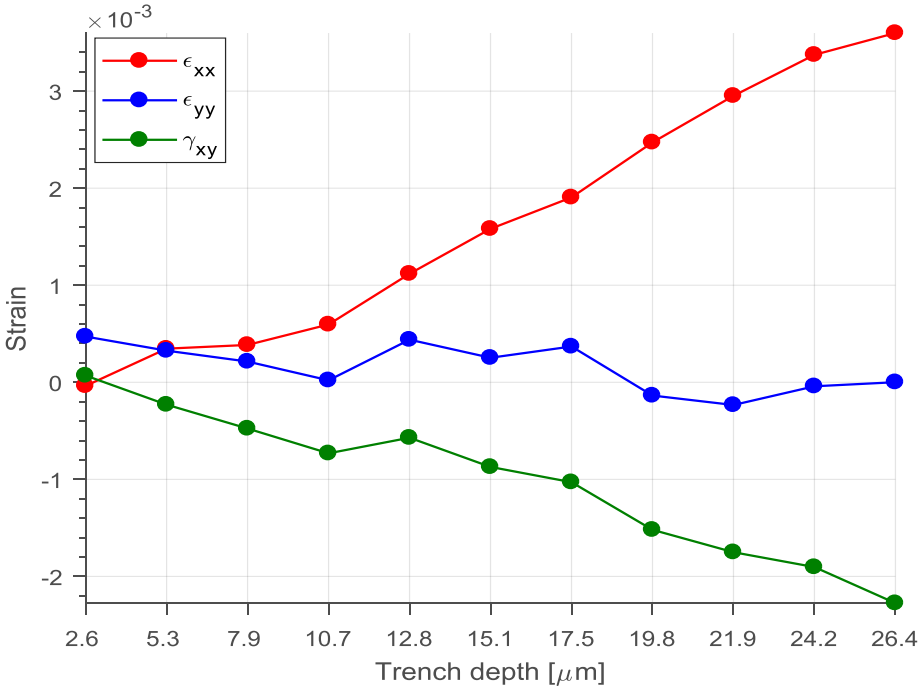

Figure 4.8 Plane strain components calculated at each depth increment.

The stress components could not be extracted as full relaxation was not achieved. The calculation of the stress components requires that full relaxation be achieved

and the measured displacements be applied to an FE model along with calibration coefficients for each depth increment. For further reading on how the stress calculations are performed, please consult Barsanti, *et al*. (2015).

5 Experimental results and technique analysis

This chapter will present the results obtained as well as a technique analysis based on the various experimental methods followed in Chapter 4.

5.1 Results

In this section, tables and plots are given for the stress distributions measured by the three diffraction methods and displacement plots are given for the combined SEM/FIB – DIC methodology.

5.1.1 Neutron diffraction results

The results obtained from the neutron diffraction analyses are presented in this section. The method used was able to resolve stress in three orthogonal directions through the full depth of the specimens. Figure 5.1 to Figure 5.4 shows the stress distribution along the *xz* plane running through the centre of the specimens. Note that a grid has been imposed into the figures to mark the position of zero stress magnitude. The surface created by separating the specimen from the base plate is at the position of $z = 0$ mm.

It can be seen in Figure 5.1 to Figure 5.4 that the stress is compressive over most of the analysed domain in all three measurement directions. However, the stress near the surfaces tends to have a lower compressive magnitude or be tensile. This is in agreement with research that has been conducted previously, which showed that there tends to be tensile stresses at the top and bottom surfaces of SLM built specimens (Mercelis and Kruth, 2006; Yadroitsev and Yadroitsava, 2015). All of the figures show that the stress in the *z*-direction is more uniform over the domain than in the other two directions, which show an approximately parabolic distribution. The full set of stress results, along with the standard deviation calculated for the stress at each point can be found in Appendix E.1.

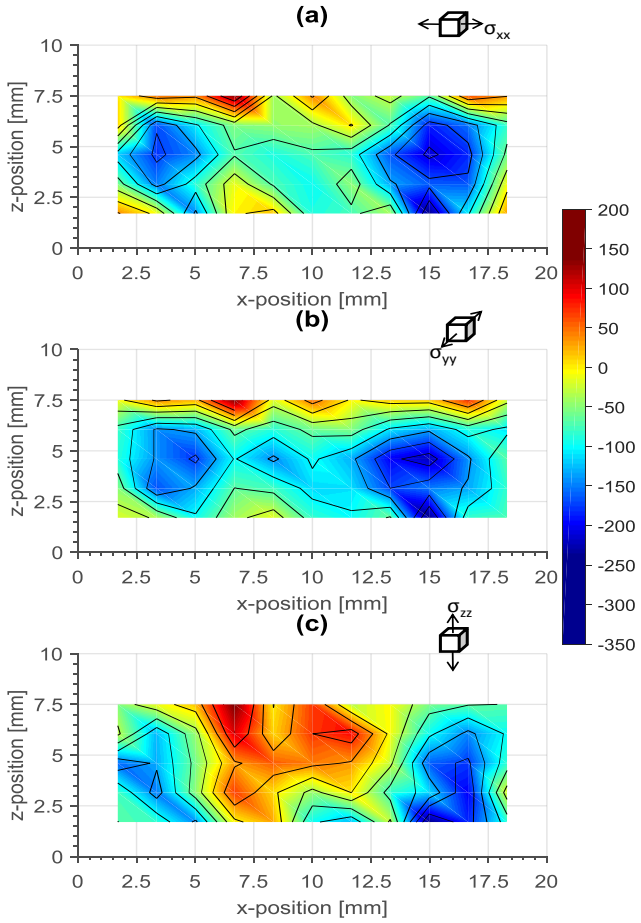

Figure 5.1 Stress a) σ_{xx}, b) σ_{yy} and c) σ_{zz} measured for specimen 130.

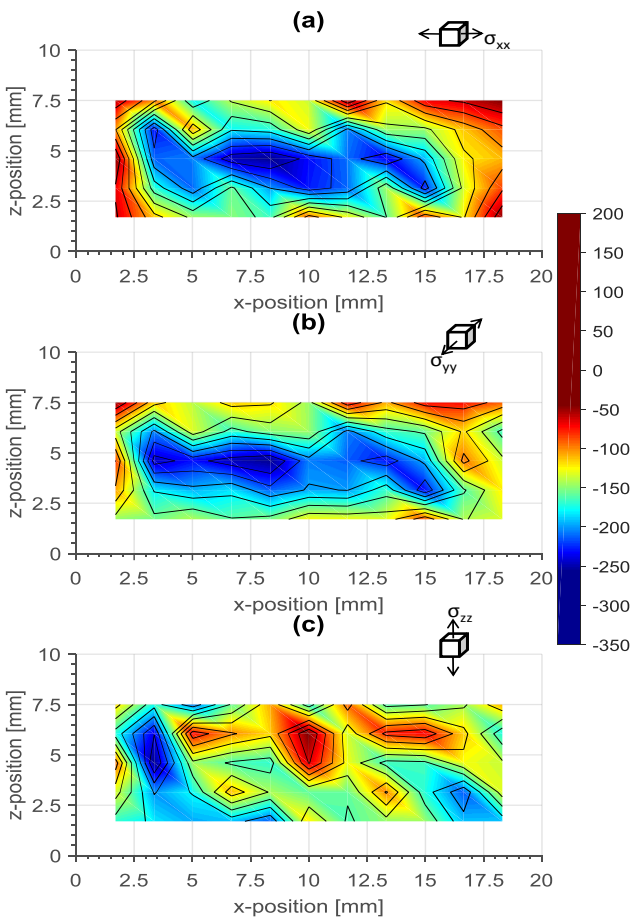

Figure 5.2 Stress a) σ_{xx}, b) σ_{yy} and c) σ_{zz} measured for specimen 230.

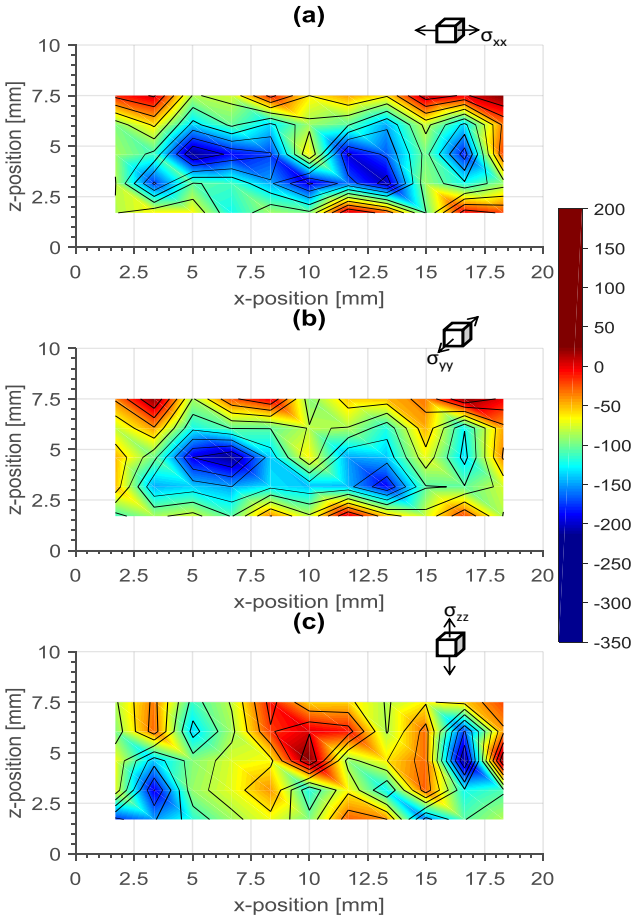

Figure 5.3 Stress a) σ_{xx}, b) σ_{yy} and c) σ_{zz} measured for specimen 290.

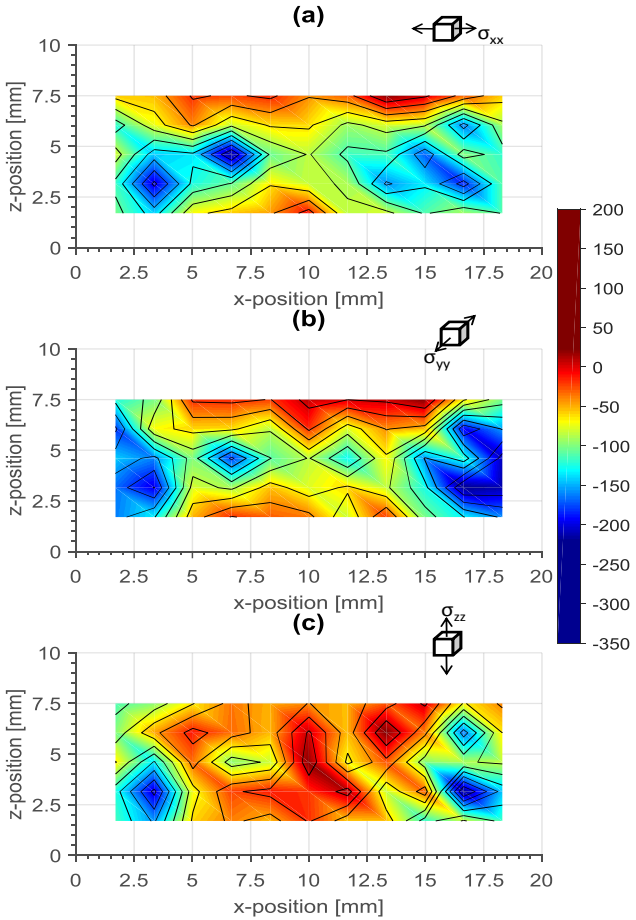

Figure 5.4 Stress a) σ_{xx}, b) σ_{yy} and c) σ_{zz} measured for specimen 330.

5.1.2 XRD surface stress results

This section presents the results obtained from the XRD surface stress analysis. This method was capable of resolving the near surface stress distribution at the top surface of the specimens. As the number of measurement angles used was sufficient to produce a full plane stress tensor, the principle stress magnitudes and directions could be calculated.

The stress tensor components calculated from Equation (4.1) can be found in Table F.1. Plots of the stress components, along with their confidence bands, for each specimen are shown in Figure 5.5 and a table of the calculated principal stresses and their directions is shown in Table 5.1.

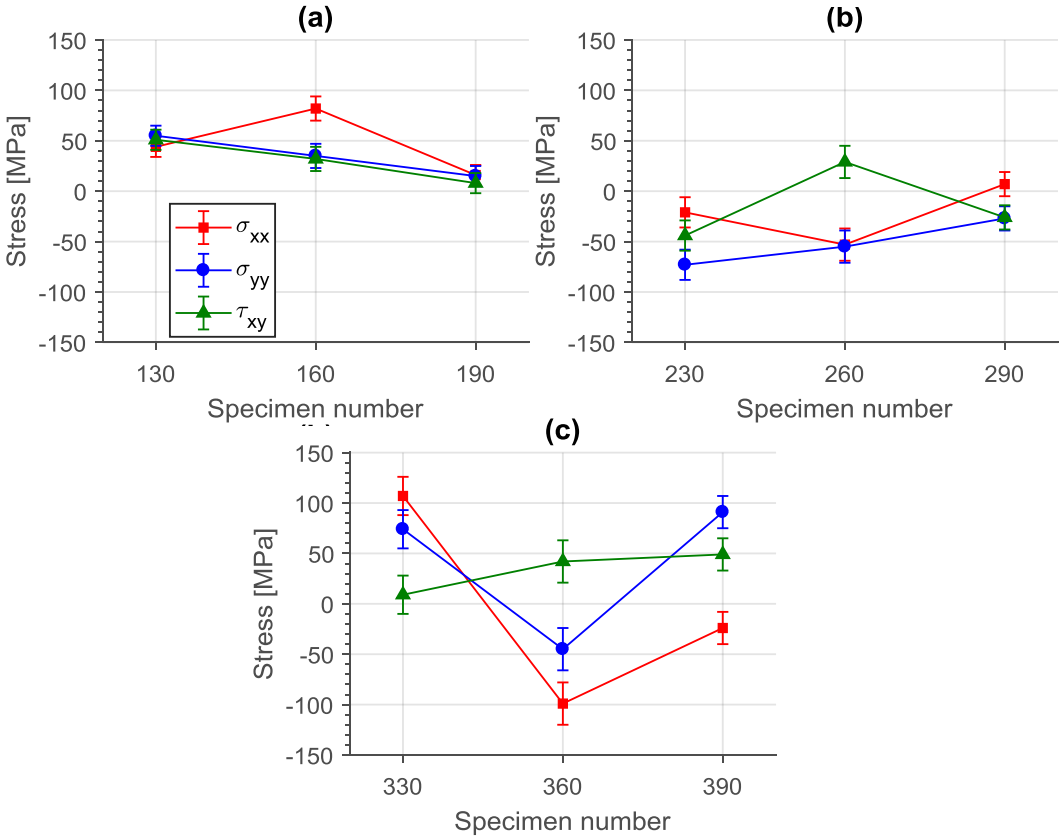

Figure 5.5 Measured surface stress components for specimens from a) exposure strategy 1, b) exposure strategy 2 and c) exposure strategy 3.

The exposure strategy 2 samples show almost entirely compressive stress at the surface. This is in contrast to surface stress results obtained by some researchers (Casavola *et al.*, 2009; Yadroitsev and Yadroitsava, 2015). However, it is in agreement with recent research done on surface RS in DLMS produced Ti64 (Lim *et al.*, 2017).

Table 5.1 Calculated principal stresses and their orientation to the x-axis.

Specimen	σ_1 (MPa)	σ_2 (MPa)	Direction (°)
130	100 ± 10	-2 ± 10	-42
160	98 ± 12	20 ± 12	27
190	23 ± 10	8 ± 10	44
230	4 ± 15	-98 ± 15	-30
260	-25 ± 16	-83 ± 16	44
290	21 ± 12	-41 ± 12	-28
330	109 ± 19	72 ± 19	14
360	-22 ± 21	-122 ± 21	-28
390	109 ± 16	-42 ± 16	-18

5.1.3 XRD stress profile results

The first set of results obtained from the analysis is the diffraction curves for the various χ tilts at each ϕ angle and depth increment, an example of which can be found in Figure 8.1 to Figure 8.3. Arbitrarily the angle $\phi = 0°$ is assigned to the *x*-axis of the specimen, shown in Figure 4.4. Thus $\sigma_{\phi=0} = \sigma_{xx}$, $\sigma_{\phi=90} = \sigma_{yy}$ and τ_{xy} can be calculated by using Equation (4.1). Figure 5.6 shows the stress values calculated at each depth, with confidence limits, for each sample analysed. Table G.1 to Table G.3 shows all calculated stress values along with the calculated errors.

5.1.4 FIB-DIC displacement results

Due to equipment malfunctions in the later phase of testing, no tests were able to be performed on the SLM produced Ti64. However, these tests are planned to be performed as soon as the equipment becomes operational.

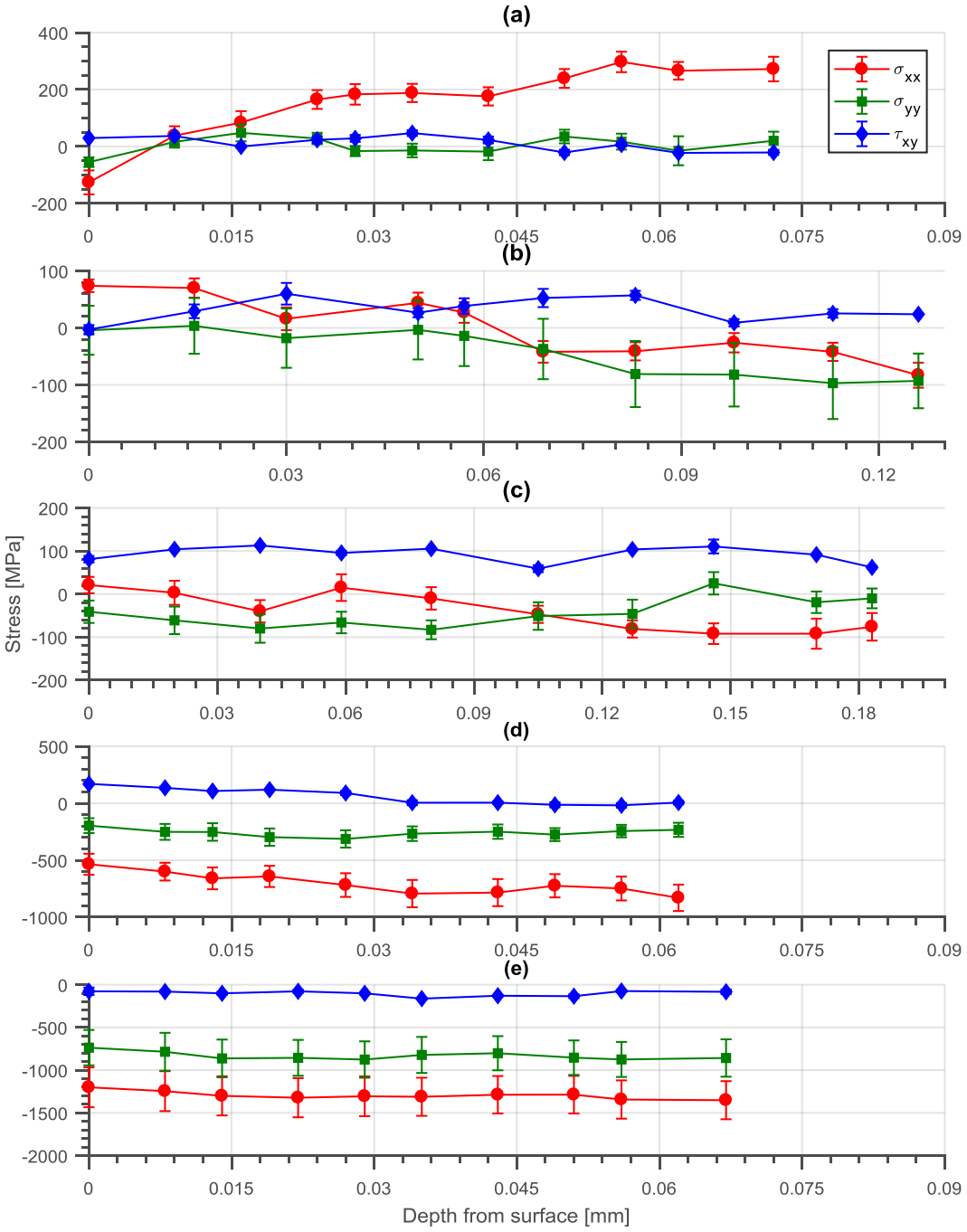

Figure 5.6 Stress vs depth profile for a) specimen 130, b) specimen 160, c) specimen 190, d) specimen 230 and e) specimen 330.

5.2 Technique analysis

This section will provide an assessment of the techniques used and the relevance of the obtained results to SLM produced Ti64.

5.2.1 Neutron diffraction

The ND testing was intended as a means of resolving the macro-scale, Type I, stress distribution through the full depth of the test specimens. Due to the penetration capabilities of the thermal neutron beam, penetration through the full depth of the specimens was achieved. This exceeded the penetration depth of 4 mm in Ti-alloys estimated by Withers & Bhadeshia (2001b).

The technique was successful in resolving a triaxial Type I stress distribution through the depth of the specimen, as intended, with a measurement confidence inverval of ~30 MPa. However, due to flaws in the assumptions used during the analyses, the results could only be used qualitatively. The reference specimens used for attaining the zero-stress spacing had not been stress relieved through heat treatment as such heat treatments can alter the microstructure of the material and thus the crystallographic structure. Thus, it is unknown whether the assumption that these specimens were truly stress free was flawed or not. The second assumption made, that the principal directions correspond to the coordinate system, was known to be a flawed assumption and was used as a means to reduce the analysis time. This was further emphasised by the results shown in Table 5.1, which shows the orientation of the principal axes from the specimen coordinate system.

In order to have achieved accurate quantitative results, by using six ϕ orientations instead of three, the duration of the analyses would have increased to ~30 days per sample. The duration required for performing ND analyses is thus the limiting factor in the use of this technique. The use of a smaller analysis domain would have allowed for shorter test durations, in which case a full set of ND scan orientations may have been practical. The long testing durations required for ND mean that careful planning of the desired analysis domain and number of measurements performed is needed before testing can commence. This makes this technique technically challenging as it is often not known what the RS distribution will be.

Despite the quantitative errors due to the assumptions made, the obtained data shows that the use of ND has merit in the application of measuring RS in SLM produced Ti64. The technique made it possible to resolve a definable stress distribution through the full depth of an SLM produced Ti64 specimen, without being limited by measurement noise or measurement resolution.

5.2.2 XRD surface stress and depth profiling measurements

Although surface stress XRD measurements have limited applicability to the quantification of the RS distribution in SLM produced Ti64 components, they can provide important information about the stress state at the top surface of the component. This technique was able to resolve the plane stress tensor at the surface of the material, and from this the principal stresses and their orientation

could be computed. The surface stress analysis was able to perform Type I stress measurements to a resolution of ~1 MPa, within an average confidence band of 20% relative error.

It has been found in previous research that the maximum stress found in SLM produced components occurs at the top surface and reduces rapidly with distance from the surface (Yadroitsev and Yadroitsava, 2015; Mercelis and Kruth, 2006; Casavola *et al.*, 2009). Thus, the ability of XRD to perform accurate stress measurements at the surface makes it a powerful technique for quantifying the peak stress formed in SLM produced components. Additionally, due to the penetration depth of the X-rays, the stress values are not averaged over a significant depth and the measured stress can be taken as the true surface stress value. However, care should be taken in interpreting the stress results in specimens with high surface roughness as this surface roughness can influence the accuracy of the results (Fitzpatrick *et al.*, 2005).

By incorporating the use of electro-polishing to perform incremental surface stress measurements, the capabilities of XRD are extended. The combination of these two techniques allowed for the in-plane stress distribution through the top two build layers of the tested specimens to be resolved successfully. The measurable stress scale was thus between the Type I and Type II scales, as described in Section 2.3. No previous testing of this nature has been performed with SLM produced Ti64. The use of this method shows promise in evaluating the evolution of RS in SLM produced Ti64 components. Through a better understanding of the stress distribution through the build layers, a link may be able to be formed between this stress distribution and the stress distribution through the component at the macro-scale.

With the use of the $\sin^2\psi$ method of stress calculation coupled with the plane stress assumption, the measurement procedure is relatively simple. The surface stress analyses can be performed in approximately 4 hours per specimen, whereas the stress profiling measurements require approximately 2 days per specimen due to the added intricacy of performing the depth increments. These test durations are sufficiently short that a high number of measurements can be performed without becoming impracticable. Furthermore, the equipment required to perform the analyses, although not as common as that required for standard hole-drilling tests, is relatively accessible compared to the equipment required for ND or FIB milling.

5.2.3 Micro-stress relaxation with DIC

This technique has been used successfully to quantify stress down to a scale of 3 µm (Korsunsky *et al.*, 2009; Korsunsky *et al.*, 2010). However, scaling it up to perform measurements at ~50 µm presented several challenges.

Due to the scale at which testing was performed in this experiment, it was assumed that the influence of the milled speckle pattern on the stress results would be negligible. This was a safe assumption as the depth of the speckle pattern was approximately one tenth of a single milling increment. Additionally, it was assumed that the volume affected by ion damage would be negligible relative to the scale of the region of interest. These two assumptions simplified the testing procedure as the deposition of a protective surface layer was not required.

The larger scale meant that the use of low ion beam currents, such as the 28 pA used by Korsunsky, *et al.* (2009), which are preferable due to the low ion damage associated with them, resulted in impractically long milling durations; up to 18 hours for a single increment. Thus, the use of higher beam currents was necessary. High beam currents are associated with high ion erosion of the surface, which is problematic for the application of DIC. Ion erosion can artificially distort surface features leading to erroneous displacements being measured by the DIC algorithm. This problem was exacerbated by using the FIB to capture snapshots of the surface in order to realign the FIB milling area after each stage tilt. However, by reducing the imaging window to exclude the speckle pattern, the influence of ion erosion on the analysis surface could be minimized.

A further problem associated with the scale at which testing was performed was the large amount of material that was ejected from the milling site by the ion beam. This ejected material tends to deposit on surfaces near the milling site and appears as powder-like particles on the surface. This is, again, problematic for the application of DIC as the deposited material tends to alter the surface features, causing correlation errors. This problem was solved by using an outer-to-inner spiral milling pattern and a wide trench. This allowed the ejected material moved towards the outer edge of the trench instead of onto the central stub.

The use of the SEM to capture images also presented some challenges. Due to the tilting required between the SEM and FIB columns, the SEM required refocusing and contrast adjustment at each imaging step. As DIC uses pixel based arithmetic to perform correlation calculations, the refocusing and contrast adjustment results in erroneous displacement measurements to occur. This is due to a change in the light intensity values of some pixels within a subset that is not associated with a physical displacement. To minimize this effect, care was taken to set the SEM to the same focus and contrast value for each image acquired.

Despite the technically challenging nature of this technique, the testing performed on the wrought 12CrNiMo steel was successful in producing displacement maps that could be used to calculate the in-plane strain components to a depth of ~20 µm. If full relaxation had been achieved, the stress components at each depth increment could have been calculated from the measured displacements. These stresses are, similar to the XRD stress profiling, at the SLM layer scale and lie between the Type I and Type II stresses described in Section 2.3. Furthermore, the calculated strains were representative of a shot peening surface treatment.

However, due to an equipment breakdown, no testing could be performed on a SLM produced Ti64 specimen.[8].

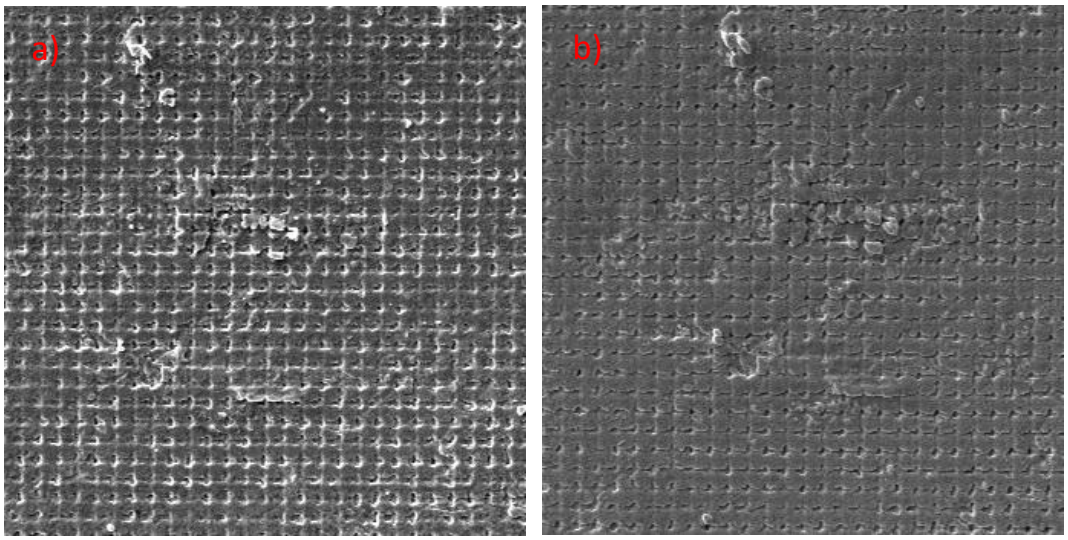

Figure 5.7 Central area of the stub showing the speckle pattern a) before milling and b) after the last milling step. The softening of surface features due to ion erosion and sputtering can be seen.

The reliance of this method on the use of a dual beam FIB/SEM is what limits its application in measuring RS in SLM produced Ti64. Due to the high cost of the equipment and the specialised facilities required to house it, access to this technique is limited. In South Africa, the only facility where this equipment is available is at the CHRTEM at NMU. Thus, although this technique shows promise that it is capable of resolving the stress distribution through a SLM build layer, much work is still needed to refine the process before this can be realised.

6 Discussion of results

In this chapter the results obtained from the various testing procedures and their relevance to furthering the understanding of RS in SLM produced Ti64 will be discussed. Links between the process parameters used and the resultant RS are formed through the interpretation of the attained results. Recommendations for further work is given for each technique. The discussion is broken down according to the analysis method used. The results of volumetric stress analysis

[8] Submission date is 8th September 2017. FIB/SEM broke down in May 2017 and remains inoperable at the date of submission. Testing on SLM produced Ti64 specimens will commence once the equipment has been brought back to working order

will be discussed first, followed by a discussion of the results obtained at the top surface and through the build layers.

6.1 Volumetric stress measurements analysis

ND had an advantage over the other techniques used in its ability to perform stress measurements throughout the volume of the specimens without the need for material removal. As such, the analyses performed with ND allowed for further testing using any of the other methods identified.

The use of the assumption that the principal directions were aligned with the specimen coordinate system was the most significant source of error for the ND results. The use of this assumption is the reason that the results are discussed qualitatively instead of quantitatively.

6.1.1 Volumetric stress distribution

The stress distribution on the analysis domain for each specimen was shown in Figure 5.1 to Figure 5.4. Although much of the analysis domain appears to be in a state of compressive stress, σ_{xx} and σ_{yy} at points along the edges of the domain are in tension or low compression. This is particularly evident from specimen 130, in Figure 5.1, where, at $z = 7.5$ mm, both σ_{xx} and σ_{yy} are tensile. Furthermore, the figures indicate that the stress near the bottom surface, at $z = 1.7$ mm, is also in tension or in low compression compared to the central volume. The RS is shown decreases sharply with distance from the free surfaces, resulting in an approximately parabolic distribution in the z-direction. This parabolic distribution, most evident in Specimen 130 and 230, is shown in Figure 6.1 and Figure 6.2. Interestingly, the stress distribution in the x-direction also appears to be approximately parabolic in the specimens produced using exposure strategy 2. However, this is not the case for specimen 130. This is due to the uni-directional scan strategy used in specimen 130 as opposed to the bi-directional scan strategy used in specimen 230

Parabolic functions were fitted to the results in each direction and are represented by the dotted lines in Figure 6.1 and Figure 6.2. These curves can be used to extrapolate the approximate stress magnitude at the surfaces of the specimens. It can be seen that the extrapolated stress values in Figure 6.1 at $z = 10$ mm shown an ~90% drop in magnitude when compared to the stress measured at $z = 7.5$ mm This drop in magnitude is similar to what is reported by reported by Mercelis & Kruth (2006) and Casavola, *et al.* (2009).

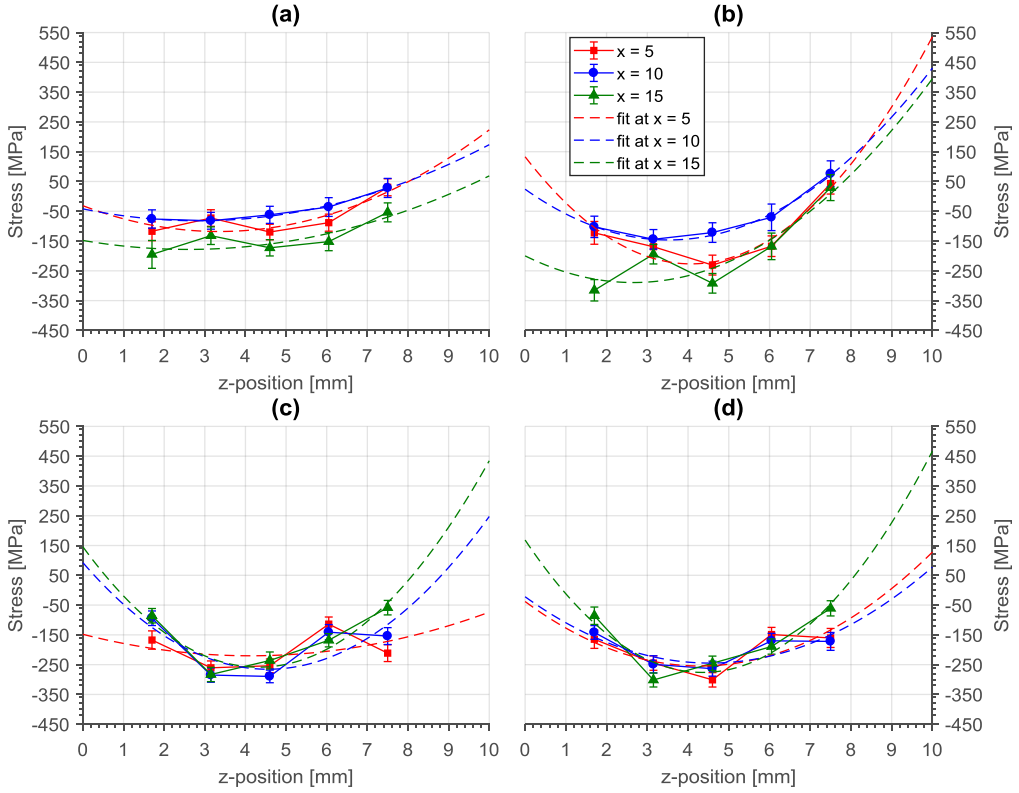

Figure 6.1 Parabolic distribution of stress, with fitted curves, in the *z*-direction for Specimen 130 in a) σ_{xx} and b) σ_{yy} and for Specimen 230 in c) σ_{xx} and d) σ_{yy}

No research could be found to indicate that these stresses have been studied before and it is assumed that they have been dismissed as insignificant compared to the stress at the top and bottom surface.

As it is known that the stress magnitude decreases upon releasing a component from the base plate, it is likely that a stress state like that shown in Figure 6.3 a) exists while components are still attached to the base plate. The theoretical deformation that would result from this stress distribution upon releasing a component from the base plate is shown in Figure 6.3 b). Figure 6.4 shows the physical manifestation of this deformation in SLM produced Ti64 specimens. The red arrows indicate vertical surfaces that experience concavity. In Figure 6.3 the red areas are regions of tensile stress and the blue areas are regions of compressive stress. The size of the tensile stress region diminishes upon release from the base plate.

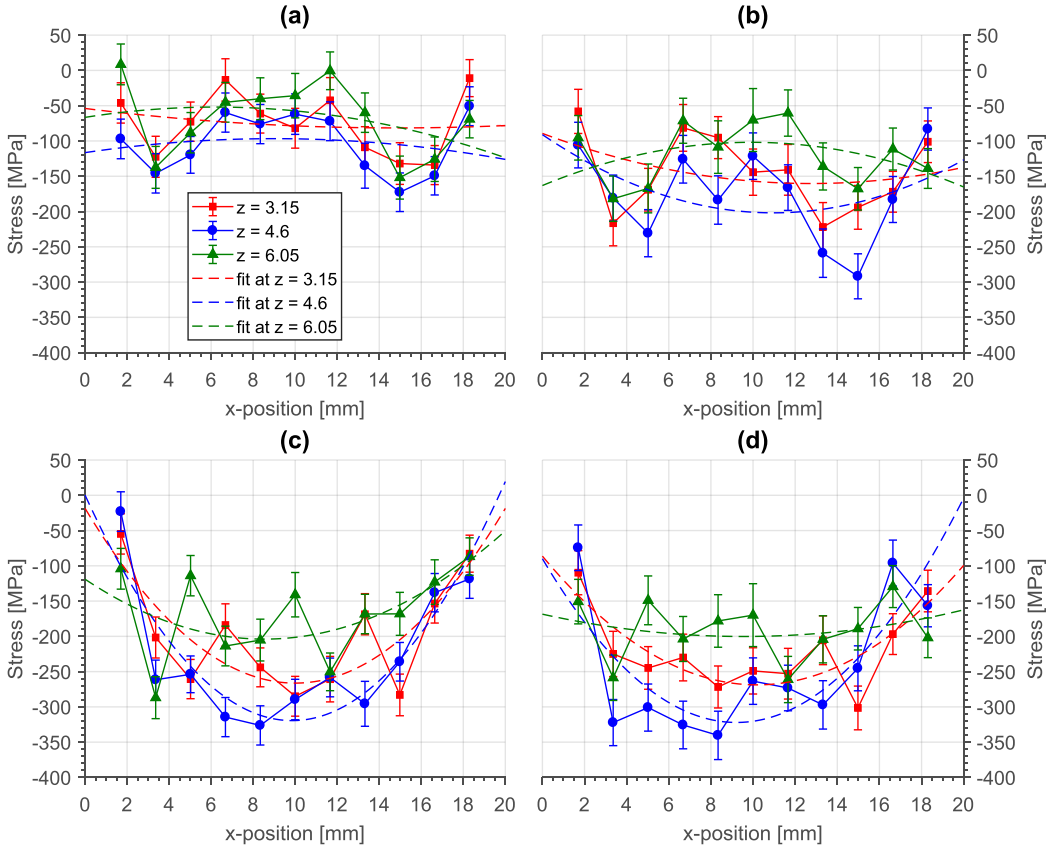

Figure 6.2 Parabolic distribution of stress, with fitted curves, in the *x*-direction for Specimen 130 in a) σ_{xx} and b) σ_{yy} and for Specimen 230 in c) σ_{xx} and d) σ_{yy}

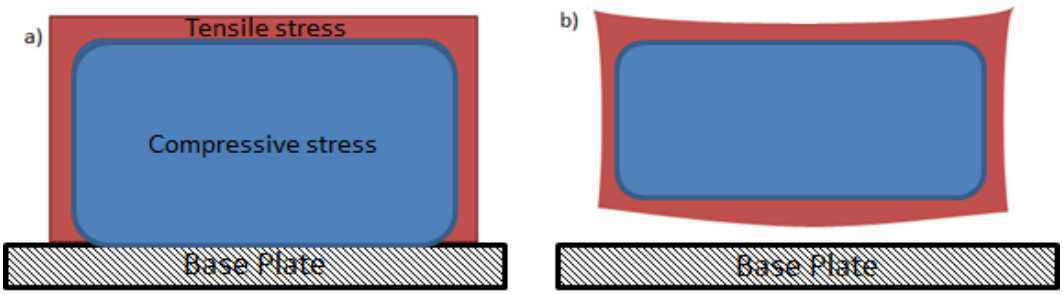

Figure 6.3 Representation of a) the stress distribution through a specimen still attached to the base plate and b) the deformation resulting from this stress distribution upon the release of the specimen.

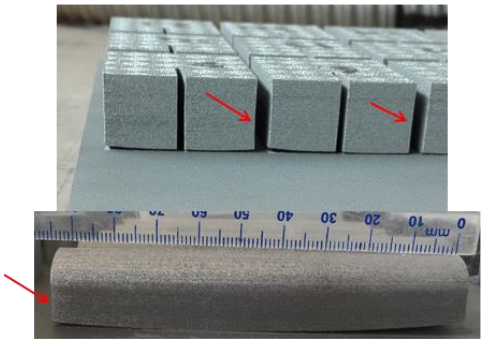

Figure 6.4 Warping and concavity at free surfaces of SLM produced Ti64 specimens caused by RS distribution.

It is important to consider the domain over which the ND analysis was performed. The positioning of the gauge volume centres resulted in a loss of data from the top surface to a depth of ~1 mm and from the bottom surface to a depth of ~0.5 mm. As discussed by Casavola, *et al*. (2009), the stress at the surface is ~80% higher than at a depth of 1.5 mm from the top surface. This means that the results obtained by the ND analysis at the highest *z*-position (closest to the top surface) were ~80% lower than what would be measured at the surface with this technique.

It can be seen from Figure 5.1 to Figure 5.4 that the σ_{zz} stress is of little interest as it shows no real trend and appears to just be noisy data at some offset position. As discussed by Parry, *et al.* (2016), σ_{zz} has the lowest magnitude of the three directions and also appears to be relatively constant over the analysis domain compared to the stress components σ_{xx} and σ_{yy}. Zaeh and Branner (2009) also found that for unidirectional and alternating scan strategies, the σ_{zz} stress is relatively constant through the depth of the specimen and is lower in magnitude than σ_{xx} and σ_{yy}. It should be noted that despite σ_{zz} being of little interest, ε_{zz} is the most significant of the strain components, leading to the upwards curvature associated with releasing the specimens from the base plate (Parry *et al.*, 2016).

6.1.2 The effect of layer thickness

By increasing the layer thickness, the number of layers required to form the specimen is reduced. Specimens constructed with a 30 µm layer thickness required 334 build layers, specimens with a 60 µm layer thickness required 167 layers and specimens with a 90 µm layer thickness required 112 layers. As mentioned in Section 2.4, the magnitude of the developed RS is directly proportional to the number of build layers used and this is confirmed by the results shown in Figure 5.2 and Figure 5.3.

The results show that an increase in layer thickness decrease both the stress magnitude as well as the stress gradient. This decrease in stress gradient is shown most prominently in Figure 6.5 a) and b), with the stress gradient in the *z*-direction of Specimen 290 being approximately half that of Specimen 230

(Specimen 260 was not examined with ND). A decrease in stress gradient in the *x*-direction is not as evident in Figure 6.5 c) and d). The decrease in stress gradient in the z-direction can be attributed to the lower number of layers existing within a ND gauge volume in Specimen 290 compared to Specimen 230. The stress gradients were calculated using MATLAB's *gradient* function, which employs the central differencing method for numerical calculation of the derivative (Mathews and Fink, 2004).

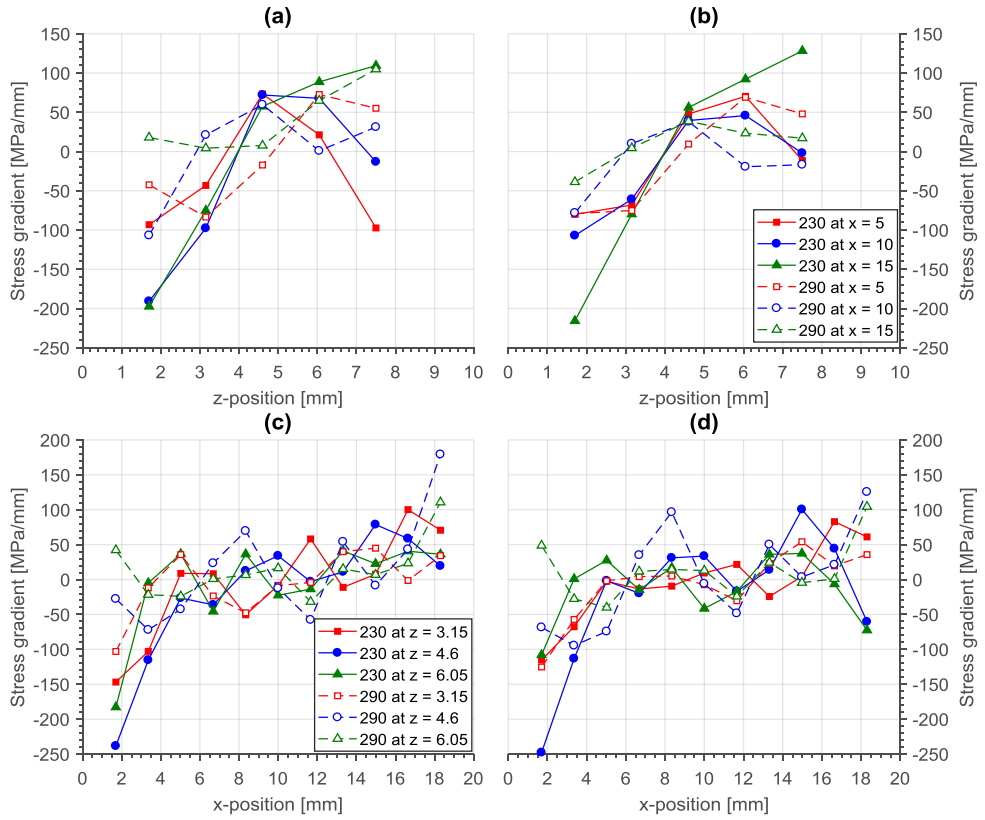

Figure 6.5 Stress gradient values in *z*-direction of a) σ_{xx} in Specimen 230 and 290 and b) σ_{yy} in Specimen 230 and 290; and in the *x*-direction for c) σ_{xx} in Specimen 230 and 290 and d) σ_{yy} in Specimen 230 and 290.

Another possible explanation for an increase in layer thickness leading to lowered stress magnitude and stress gradient can be found in the mechanism through which the RS develops. If a single, thick, layer of powder is deposited and melted, it will have a higher thermal mass than a thin layer. This means that the thick layer is better able to store heat. If additional layers are added to this, the temperature gradient between the molten region and the previously consolidated material is reduced. In turn, the cooling rate is reduced and the high tensile stresses that form during the cooling phase are minimized. This effectively acts in the same manner as a heated base plate. Shiomi, *et al*. (2004) found that heating the base plate to 160°C can reduce the magnitude of the RS by up to 40%.

Similarly, the results obtained from the ND analyses show that increasing the layer thickness from 30 µm to 90 µm reduces the stress magnitude by 25-30%.

6.1.3 The effect of exposure strategy

The major influence of the exposure strategy is on the homogeneity of the stress distribution. Yadroitsev & Yadroitsava (2015) found that by rotating the scan vectors, layer by layer, allows for the disorientation of the developed stress, but does not reduce its magnitude. By comparing the results shown in Figure 5.1, Figure 5.2 and Figure 5.4 it appears that this observation is only partially true.

Although the stress magnitudes measured for Specimen 130 and 230 are comparable, the magnitudes measured for Specimen 330 are the lowest of all the specimens analysed with the ND technique. It is possible, however, that this is due to stress magnitude measurement errors resulting from the assumptions made – as eluded to in Section 5.2.1. What is clear from Figure 5.1 to Figure 5.4 is that the use of exposure strategy 3 reduced both the stress gradient and the directionality of the stress distribution. From Figure 5.4 a) and b) it can be seen that σ_{xx} and σ_{yy} are approximately equal in magnitude over much of the analysis domain.

The stress directionality is important as it can have an influence on the mechanical performance of a component. If there is high tensile RS oriented in the direction of the in-service loading, the component will be more vulnerable to cracking or yield failure. Figure 6.6 shows the in-plane stress ratio of σ_{yy} to σ_{xx} for each of the specimens produced with a 30 µm build layer thickness. These figures can be used to assess the effect of the exposure strategy on the directionality of the RS. A grey plane has been inserted at a stress ratio of one. If the surface lies above this plane then σ_{yy} is greater than σ_{xx} and vice versa. A true bi-axial stress state is represented by a stress ratio of one or close to one. In this stress state the two normal stress components are of approximately the same magnitude. If the ratio of the maximum normal stress component to the minimum normal stress component is much greater than one, the stress state can be approximated as uni-axial.

Some local extreme values exist as the ratio surfaces were generated point for point from the stress surfaces. These extreme values can be ignored as outliers. It is clear from Figure 6.6 a) that, for Specimen 130, σ_{yy} is significantly greater than σ_{xx} for almost all points on the analysis domain. The results show that σ_{yy} is ~2-3 times greater than σ_{xx} over most of the analysis domain. This signifies that the stress state in this specimen can be approximated as uni-axial. This result was expected as previous research has shown that for a unidirectional scan strategy, the stress in the direction parallel to the scan vector is usually higher than the stress in the perpendicular direction by a factor of ~2 (Yadroitsev and Yadroitsava, 2015; Parry *et al.*, 2016). Thus, in the case of Specimen 130, the *y* measurement axis in Figure 4.3 corresponds to the axis parallel to the laser scan vector.

In Figure 6.6 b) and c) the stress in one direction does not appear to dominate over the other, as seen in Figure 6.6 a). Additionally the in-plane stress ratio is not as high in Figure 6.6 b) and c) as it is in a), with the ratio of σ_{yy} to σ_{xx} being close to unity at many points. Thus, even by using a bi-directional laser exposure strategy, as with exposure strategy 2, an approximately biaxial stress state can be achieved. The values of the calculated stress ratios in each specimen can be found in Appendix E.2. It can be seen that the use of exposure strategy 3 provides little discernible improvement to the stress disorientation compared to exposure strategy 2.

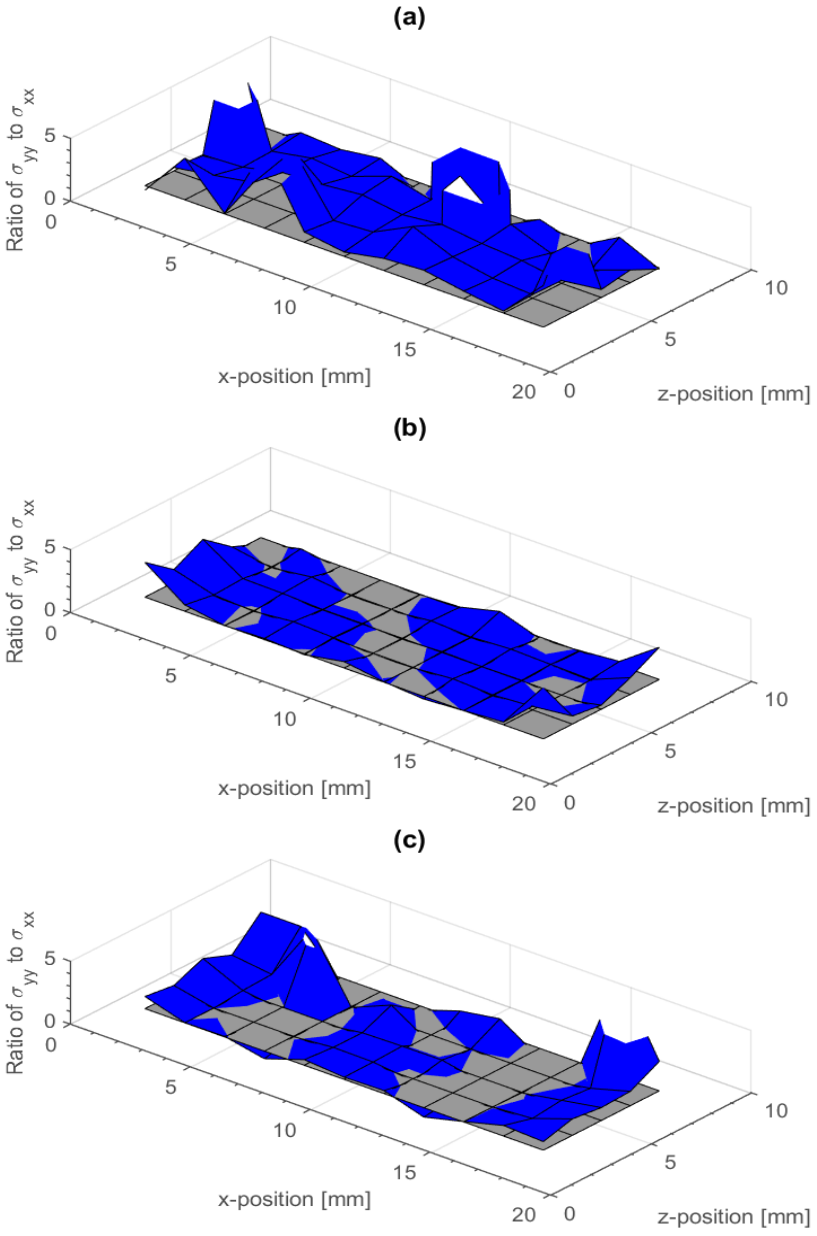

Figure 6.6 Ratio of σ_{yy} to σ_{xx} for a) Specimen 130, b) Specimen 230 and c) Specimen 330

6.1.4 Recommendations for further work

The use of this technique for further research into the RS distribution in SLM produced Ti64 components should be done in such a way that a full stress tensor can be created. Thus measurements in six independent ϕ directions should be performed. This is advisable as the distribution of stress resulting from the SLM build process is complex and as such, the use of the principal stress assumption is inherently flawed. In order to mitigate the increased testing duration associated with increasing the number of ϕ angles scanned, the size of the analysis domain can be reduced.

As seen from the results obtained in Section 5.1.1, the stress distribution is approximately symmetrical across the lines shown in Figure 6.7. Thus a single quadrant of the analysis domain used in this study, shown in Figure 6.7, would provide sufficient information about the stress distribution. The analysis domain should be defined so as to allow stress measurement to be captured from the material as close to the surface as possible.

Furthermore, it is advised that sufficiently stress relieved specimens are used to establish the reference lattice spacing. This can be done by cutting a small pillar from the test specimen using wire EDM and then sectioning this pillar into smaller cubes. These cubes can then be used to determine the reference spacing at a number of depths through the test specimen. Alternatively the powder used to produce the specimens can be used to measure the reference lattice spacing. A micronized powder cannot hold macro-stresses and thus the lattice spacing of the powder is a true zero-stress lattice spacing. However, this technique is not strongly advised as the high heat input associated with the SLM manufacturing process can result in a change in the chemical properties of the material. For example, the amount of Vanadium precipitates in Ti64 can influence the lattice spacing and can be altered by heat treatment.

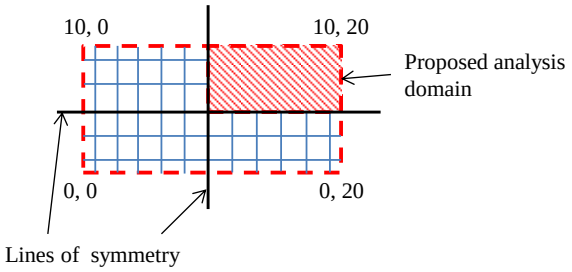

Figure 6.7 Lines of symmetry across analysed domain used and a proposed analysis domain for further testing.

6.2 Top surface stress analysis

The surface stress analysis was performed in order to accurately quantify the RS magnitude present at the top surface of the specimens. As the top surface is the location of the most severe stress experienced by a SLM produced specimen, surface measurements can be used as a representation of the overall magnitude of the RS state.

6.2.1 Stress at the surface

The ND analysis identified that the influence of increasing the layer thickness was to decrease both the stress magnitude and gradient. However, the results obtained from the XRD surface analysis do not reflect this conclusion. Figure 5.5 shows that, only in the exposure strategy 1 specimens, does an increase in layer thickness results in a decrease in magnitude of the stress components. The exposure strategy 2 and 3 specimens show an initial decrease in stress component magnitudes between the specimens manufactured with 30 µm and 60 µm layers. However, specimens manufactured with a 90 µm layer thickness display a sharp increase in stress component magnitude. A possible explanation for this is afforded by Fitzpatric, *et al*. (2005) in that high surface roughness can lead to spurious stress measurements. As a result of the limited penetration of XRD, the stress within the surface peaks strongly influences the RS measurement. As surface peaks act as stress concentrators, the measured stress appears higher than expected. There is evidence that increasing the layer thickness leads to an increase in the surface roughness due to increased spattering of the molten material (Turner *et al.*, 1998).

6.2.2 Comparison with near surface ND results

The RS measured at the surface by XRD can be related to the RS measured near the surface with ND, as seen in Figure 6.8. By averaging the ND results of the three central nodes at the $z = 7.5$ mm, a stress that is representative of the sub-service stress at the site of the XRD analysis was calculated. It can be seen that there is little agreement between the two measurement techniques. The magnitudes of the normal stress components (σ_{xx} and σ_{yy}) obtained for Specimens 230 and 330 are not consistent with those found in previous research for near surface stress values in SLM produced Ti64. Further they do not support the results of either the ND analysis or the surface XRD analysis and the results of Specimen 330 far exceed the material yield strength, which is not possible. Thus, the stress distribution measured in these specimens will be treated qualitatively.

6.2.3 Recommendations for further work

As surface XRD is a technique that is extensively used for quantifying RS in SLM produced components the only recommendation that can be given to improve the technique is to use a light surface treatment in the case of specimens with high

surface roughness. The use of electro-polishing can assist in reducing the high surface peaks that tend to influence the measured stress without adversely affecting the surface stress distribution.

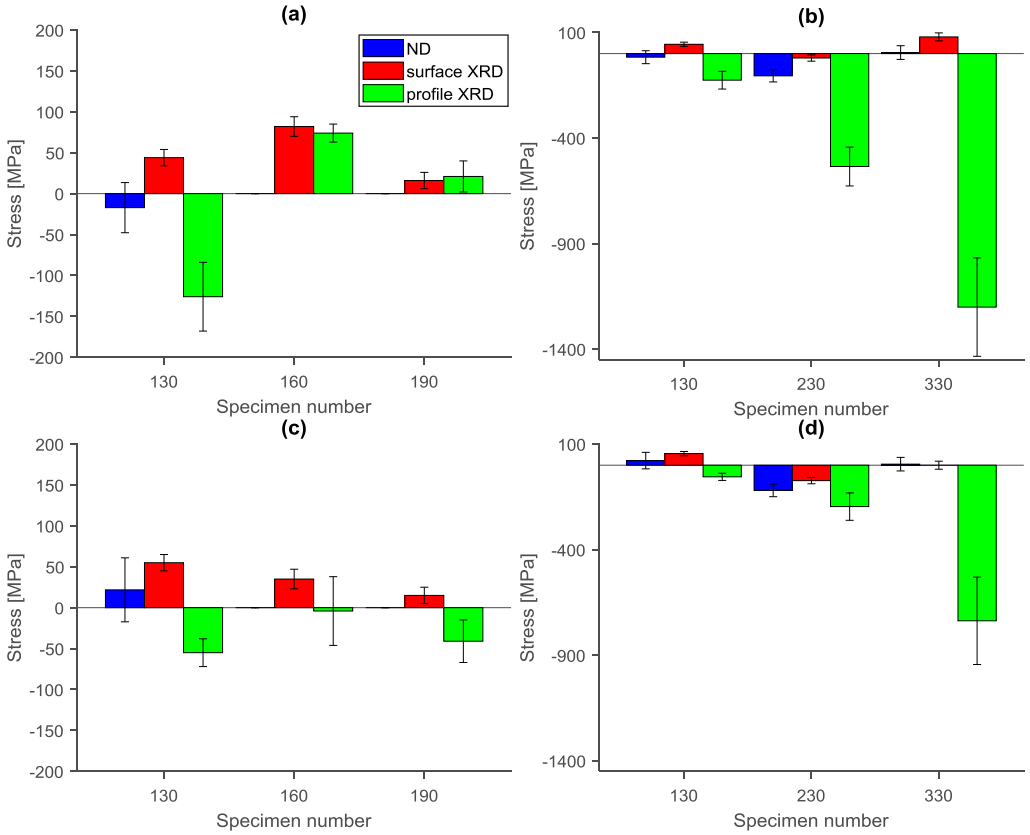

Figure 6.8 Near surface ND and XRD results for σ_{yy} compared by a) layer thickness for and b) exposure strategy; and the results for σ_{xx} compared by c)layer thickness and d) exposure strategy.

6.3 Layer stress analysis

This analysis was performed with the aim of defining the stress distribution within individual layers of a SLM produced Ti64 specimen. By using XRD in conjunction with electro-polishing, it was possible to resolve the stress distribution through the top two build layers of the tested specimens. It can be seen from the results that the shear stress in all of the specimens, except for Specimen 190, is low and tends towards zero as the depth is increased. This result was expected as the mechanism through which stress forms in SLM produced components does not induce significant shear stress.

Although the results shown in Figure 5.6 are useful for quantifying the stress present in each specimen, it does not show how the change of layer thickness or

laser exposure strategy affects the distribution of the stress. The results were rescaled using Equation (6.1) to allow for a direct comparison of the effects of changing the layer thickness and exposure strategy. The stress results at each scaled depth increment are shown in Figure 6.9 and the scaled stress results at each depth increment are shown in Figure 6.10.

$$\boldsymbol{\sigma}_{scaled} = \frac{\boldsymbol{\sigma_{ii}}}{(\sigma_{avg})} \qquad \boldsymbol{h}_{scaled} = \frac{\boldsymbol{h}}{H}, \tag{6.1}$$

Where $\boldsymbol{\sigma}_{scaled}$ is a vector of scaled stress values, $\boldsymbol{\sigma_{ii}}$ is a vector of the stress values measured at each increment for a particular stress component, σ_{avg} is the average of $\boldsymbol{\sigma_{ii}}$, $\boldsymbol{h}_{scaled}$ is a vector of the scaled depth increments, $\boldsymbol{h}$ is a vector of the measurement depth increments and H is the layer thickness.

6.3.1 The effects of layer thickness

By scaling the depth increments to a maximum of 1, as shown in Figure 6.9, it is possible to make a direct comparison between the stress profiles of the three layer thicknesses. In order to ensure that the change in layer thickness was the only parameter to affect the stress results, only specimens from exposure strategy 1 were considered.

Similarly to the results shown by the ND analysis, the effect of increasing the layer thickness is to reduce the stress gradients present in the material. This mechanism is thus present for both the part scale stress as well as the layer scale stress. It can be seen that by increasing the layer thickness, the stress magnitude is decreased. This is most evident when comparing the magnitudes of the stress in Specimen 130 to Specimen 160. The reduction in stress magnitude from Specimen 160 to Specimen 190 is not as clear. This may point to stress reduction by layer thickness increase having an asymptotic nature, where successive increases in the layer thickness result in diminishing reductions in stress magnitude.

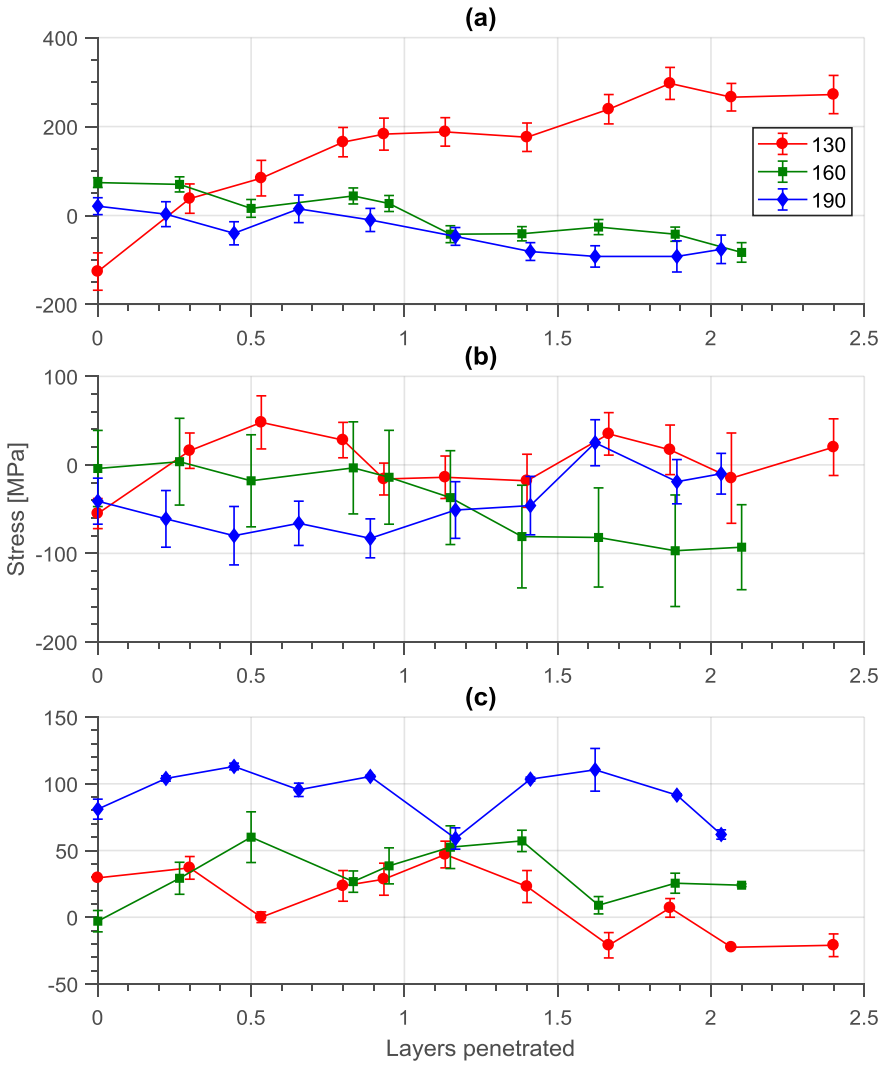

Figure 6.9 Stress vs number of layers penetrated in exposure strategy 1 specimens for a) σ_{xx}, b) σ_{yy} and c) τ_{xy}.

6.3.2 The effects of the scan strategy used

By rescaling the stress values of the three specimens manufactured with 30 µm build layers, the effect of the exposure strategy can be compared directly. Figure 6.10 shows the scaled stress magnitudes for each depth increment. The RS distribution in Specimen 130 fluctuates noticeably through the build layers, whereas Specimen 230 and 330 display a more constant stress distribution. This is due to the disorientation of the RS in Specimen 230 and 330 by alternating the laser vector directions, as described by Yadroitsev & Yadroitsava (2015). In support of the results obtained by the ND analysis, the exposure strategy is shown to influence the stress gradient, which ties into the mentioned stress oscillation. The stress gradients in Specimen 130 are much higher than those in Specimen 230 and 330, which is consistent with the results from the ND analysis.

Unlike the results obtained from the ND analysis, the exposure strategy used does not appear to play a significant role in reducing the directionality of the stress distribution through individual build layers. At the localised scale at which these measurements were performed, the influence of rotating the laser vector is not realised, as it is at the part scale. Thus, it can be said that at the layer scale, the stress within the layer remains approximately uni-axial even if the stress at the part scale is approximately bi-axial.

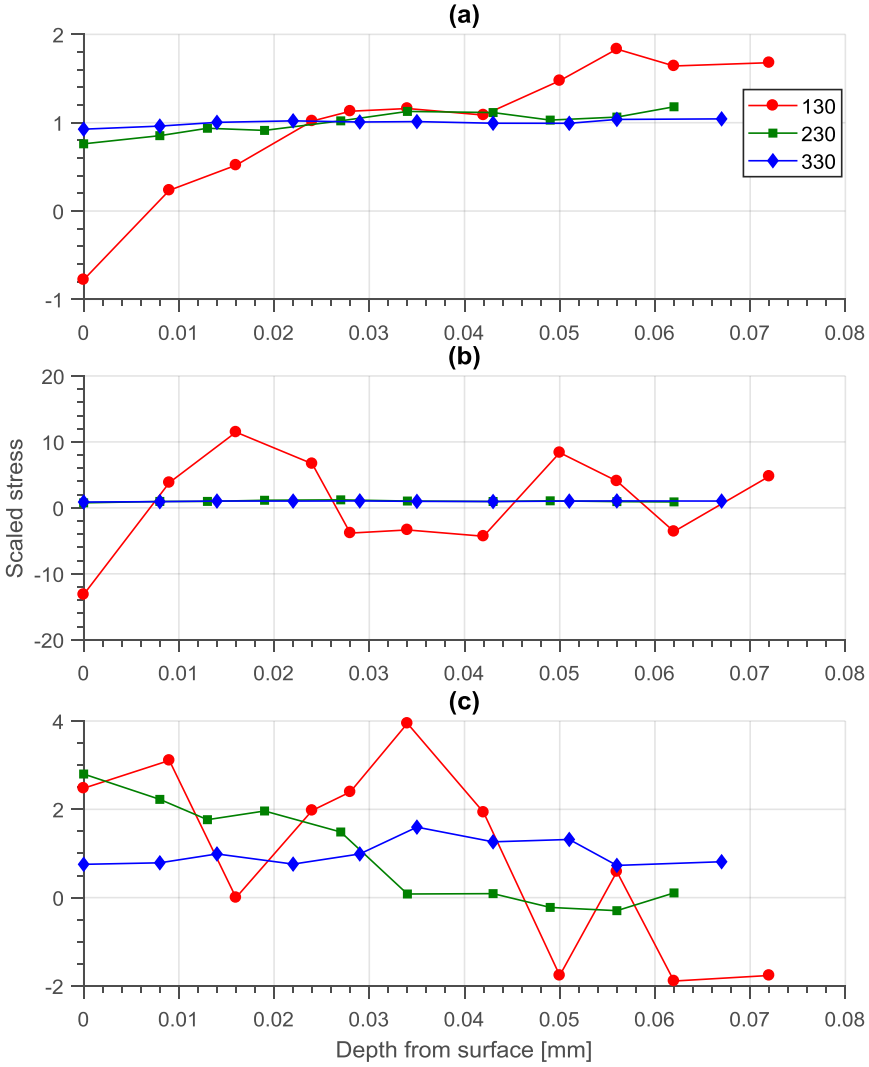

Figure 6.10 Scaled stress vs depth increment in specimens with 30 µm build layers for a) σ_{xx}, b) σ_{yy} and c) τ_{xy}.

6.3.3 Recommendations for further work

The accuracy of the measurements can be improved by experimentally determining the XEC's, S_1 and S_2, for SLM Ti64 for the analysed family of lattice planes. Although wrought Ti64 can be regarded as an isotropic material, due to

the nature of the microstructure that develops during the SLM manufacturing process, SLM produced Ti64 tends to have directional material properties and is thus not truly isotropic (Lim *et al.*, 2017). This is due to the formation of columnar prior beta grains that are characteristic of SLM manufactured Ti64 (Qiu *et al.*, 2013).

6.4 Progress of the FIB – DIC method

Once the required equipment has been brought back into operation, it is intended to begin testing on SLM Ti64 using the methodology established along with the recommended corrections. Due to the complexity of the stress that has been shown to develop in SLM manufactured specimens it is foreseen that further refinements to the established method will be necessary once testing has begun with SLM Ti64.

7 Conclusion

This research project set out to identify and evaluate the capabilities of a number of stress measurement techniques in the application of measuring RS in SLM produced Ti64. This research provides the basis for the establishment of a testing framework that can be used in further research. Further this project performed a brief investigation into the effects of two SLM build parameters, namely the build layer thickness and exposure strategy, on the distribution of RS at various scales of interest. The project formed part of the CPAM initiative with the global aim of qualifying SLM produced Ti64 for industrial application in South Africa.

Through a thorough review of RS and how it is generated by the SLM build process, it was concluded that two major scales of stress are of interest in SLM produced Ti64. The first scale, Type I stresses, are present at the part scale and equilibrate over the full size of the built component. This RS plays a significant role in the mechanical performance of the component. The build-up of stress at this scale can lead to manufacturing failures such as delamination and component deformation. The second scale of interest exists at a scale between that of Type I and Type II (microstructural scale) stresses. This stress propagates through the individual build layers of an SLM produced specimen. It is this incremental addition of this scale of stress that leads to the build-up of Type I stress in SLM produced components.

Stress measurement techniques were investigated that showed the capability of the measurement of one or both of the stress scales of interest. A detailed review of each technique was performed w.r.t the resolvable stress tensor, the stress scale measureable, measurement assumptions made and the stress measurement resolution. Through this review, four measurement techniques were selected for evaluation: neutron diffraction, surface XRD, XRD stress vs depth profiling and a miniaturised stress relaxation technique using a dual beam FIB/SEM coupled with DIC.

These techniques were applied to specimens that had been manufactured with a nine combinations of build layer thickness and exposure strategy. The capabilities and limitations of each of these techniques can be concluded as follows:

- ND was capable of resolving a tri-axial, Type I, stress distribution across an analysis domain that extended through the full depth of the tested specimens. The methodology used produce results within a confidence interval of ~30 MPa. However, due to flaws in the assumptions used – that the principal stresses were aligned with the measurement directions and that the specimen used to measure the reference lattice spacing was fully stressed relieved – the obtained results could only be used qualitatively. The major limitations of this technique are the lack of access to the required equipment and the time required to perform measurements. In order to construct full stress tensors at each data point, testing durations of up to 30 days would have been required

for each specimen. This technique shows great promise in the application of RS measurement in SLM produced Ti64. However, further testing should be performed in such a way that a full stress tensor can be measured, the analysis domain can be reduced in order to make this testing practical.

- The XRD surface analysis was capable of resolving the in-plane, Type I, stress components at the top surface of the material. This method achieved a stress resolution on the scale of 1 MPa and an average confidence interval of within 20% relative error. Although this technique is limited by its low penetration depth, it is applicable to the measurement of RS in SLM produced Ti64 as it has been shown in literature that the maximum RS is present at the top surface of a SLM produced component. This technique is relatively accessible and the measurement process in simplified by the use of the plane stress assumption and the estimation of the stress free lattice spacing as defined by the $\sin^2\psi$ method. Further research should include the experimental measurement of the XEC's, S_1 and S_2, for SLM produces Ti64.
- The XRD stress vs depth analysis was successful in resolving the in-plane stress distribution at the layer scale of the tested specimens. The use of electro-polishing combined with surface XRD extends the applicability of XRD for the measurement of RS in SLM produced Ti64. The addition of the electro-polishing step increases the technical complexity of the testing procedure. However, the overall process remains relatively simple.
- The FIB-DIC micro-stress relaxation method developed during this project provided a number of challenges. However, it was capable of measuring full-field displacements over the chosen region of interest. A validation study performed on a wrought 12CrNiMo steel specimen showed that this technique was able to resolve the in-plane strain components associated with in-plane stress to depths that are on the scale of a single SLM build layer. As full relaxation of the SOI was not achieved, incremental stress values could not be determined. This technique, although technically challenging, is able to provide a higher depth resolution than the XRD stress vs depth profiling technique. However, as DIC has a strain resolution of ~100 με, this technique has a lower stress resolution than XRD. The major limitation of this technique is the access to the FIB/SEM equipment. There is only one facility in South Africa that has a dual beam FIB/SEM.

An analysis of results obtained by the various measurement techniques concluded the following about the influence of build layer thickness and exposure strategy on RS distribution:

- The ND analysis showed that the distribution of in-plane RS in the direction in which the component is grown (*z*-direction) is approximately parabolic, with the top and bottom surface being in tension or low compression and the internal volume being in compression. This supports the findings of previous studies. It was also found that stresses equivalent to those at the top and

bottom surface are present on the sides of the specimens. These stresses explain the concavity that occurs in the sides of some components

  - ND identified that the influence of the layer thickness on the Type I stress distribution was to decrease both the magnitude of the developed stress as well as the gradient of the measured stress components as the layer thickness increases. This supports the investigated literature, which suggests that the RS magnitude is a function of the number of build layers used. Thicker layers result in fewer layers being deposited, resulting in a lower stress magnitude. The thickness of the layer may also play a role as the higher thermal mass reduces the cooling rate and thus reduces the effects of the TGM.
  - ND identified that the influence of the exposure strategy on the Type I stress distribution is to improve the homogeneity of the stress. Specimens produced with a unidirectional exposure strategy displayed an approximately uni-axis stress distribution. By using an exposure strategy that rotates the laser vector by 90° in each successive layer, an approximately biaxial stress distribution can be achieved. The use of more than two laser vector directions did not show any discernible improvement to the homogeneity of the stress distribution.

- The top surface stress analysis did not show strong agreement between the techniques used. The surface XRD analysis may have had its results affected by the high surface roughness present at the top surface of the specimens. It appeared that the surface XRD analysis underestimated the magnitudes of the stress components at the surface
- The stress vs depth XRD profiling showed that the stress distribution through individual build layers tends to have a low shear stress, that tends towards zero with depth from the surface.
  - The stress vs depth XRD analysis identified that the influence of the layer thickness on the stress distribution at the layer scale was to decrease the stress component gradients as the layer thickness was increased. The stress component magnitude was also decreased by an increase in layer thickness.
  - The stress vs depth XRD analysis found that the effect of exposure strategy on the stress distribution at the layer scale was to reduce the fluctuation of the stress magnitude as laser vector directions are added. This is due to the disorientation of the stress components caused by alternating the laser vector direction. It was found that at the layer scale, the stress distribution remains approximately uni-axial even if the Type I stress distribution in the component is approximately bi-axial.
- Due to equipment failure that occurred in May of 2017, the FIB-DIC method was unable to be used to perform tests on SLM produced Ti64.

This project was able to identify a number of techniques which are applicable to the measurement of RS in SLM produced Ti64. The review and evaluation of the capabilities of these techniques presented in this project can be used to form a testing framework to be used in future investigations into the distribution of RS in SLM produced Ti64.

8 References

Abudayyeh, H. a (2012) *Synthesis and Analysis of ZnO Nanowires*. Bizeit University.

Albert, M. (2001) Machining to Sub-Micron Accuracy with EDM. *Modern Machine Shop*. [online]. Available from: http://www.mmsonline.com/articles/machining-to-sub-micron-accuracy--with-edm [Accessed August 26, 2017].

ASTM (2012) F2921 - Standard Terminology for Additive Manufacturing — Coordinate Systems and Test. *American Society for Testing and Materials*. **11**, 12.

ASTM International (2001) E 837-01 Standard Test Method for Determining Residual Stresses by the Hole-Drilling Strain-. . **1**, 1–16.

Barsanti, M., Beghini, M., Santus, C., Benincasa, A., Bertelli, L. (2015) Integral Method Coefficients and Regularization Procedure for the Ring-Core Residual Stress Measurement ... *Advanced Materials Research*. **996**(August 2014), 331–336.

van Belle, L., Vansteenkiste, G., Boyer, J. (2013) Comparisons of numerical modelling of the Selective Laser Melting.

Boyer, R.R. (1996) An overview on the use of titanium in the aerospace industry. *Materials Science and Engineering A*. **213**(1–2), 103–114.

Bremen, S., Meiners, W., Diatlov, A. (2012) Selective Laser Melting A manufacturing technology for the future ? *Laser Technik Journal*. **9**(2), 33–38.

BSI (2008) *BD EN 15305: Non-destructive Testing — Test Method for Residual Stress analysis by X-ray Diffraction*.

Carter, J.L.W., Uchic, M.D., Mills, M.J. (2015) Impact of Speckle Pattern Parameters on DIC Strain Resolution Calculated from In-situ SEM Experiments. *Conference Proceedings of the Society for Experimental Mechanics Series*. **66**(VOLUME 5), 119–126.

Casavola, C., Campanelli, S.L., Pappalettere, C. (2009) Preliminary investigation on distribution of residual stress generated by the selective laser melting process. *Journal of Strain Analysis*. **44**, 93–105.

Davis, J. (2012) *Analytical Modeling and Applications of Residual Stresses Induced by Shot Peening*. University of Washington.

Dowling, N.E. (2013) *Mechanical Behavior of Materials: Engineering Methods for Deformation, Fracture, and Fatigue*. 4th ed. Essex: Pearson Education

Limited.

Figliola, R.S., Beasley, D.E. (2011) Strain Measurement. In *Theory and Design for Mechanical Measurements*. John Wiley & Sons, pp. 466–479.

Fitzpatrick, M.E., Fry, A.T., Holdway, P., Kandil, F.A., Shackleton, J., Suominen, L. (2005) *Determination of Residual Stresses by X-ray Diffraction - Issue 2*. Middlesex, UK: National Physics Laboratory.

Fitzpatrick, M.E., Lodini, A. (2003) Characterization of macrostresses. In M. E. Fitzpatrick & A. Lodini, eds. *Analysis of Residual Stress by Diffraction Using Neutron and Sychrotron Radiation*. Taylor & Francis, pp. 60–77.

Da Fonseca, J.Q., Mummery, P.M., Withers, P.J. (2005) Full-field strain mapping by optical correlation of micrographs acquired during deformation. *Journal of Microscopy*. **218**(1), 9–21.

Gamiet, N. (2015) *Numerical Analysis of Compressive Residual Stresses in Metallic Materials as a Result of Shot Peening*. Univesrity of Cape Town.

Gibson, I., Rosen, D., Stucker, B.E. (2010) Introduction and Basic Principles. In *Additive Manufacturing Technologies: 3D Printing, Rapid Prototyping and Direct Digital Manufacturing*. New York: Springer US, pp. 1–19.

Group, V.P. (2010) *Measurement of Residual Stresses by the Hole-Drilling* Strain Gage Method*.

Gusarov, A. V, Malakhova-ziablova, I.S., Pavlov, M.D. (2013) Thermoelastic residual stresses and deformations at laser treatment. *Physics Procedia*. **41**, 896–903.

Herzog, D., Seyda, V., Wycisk, E., Emmelmann, C. (2016) Additive manufacturing of metals. *Acta Materialia*. **117**, 371–392.

Huchzermeyer, R.L. (2017) *Measuring mechanical properties using digital image correlation: Extracting tensile and fracture properties from a single sample*. Stellenbosch University.

Kaufmann, E.N. (2003) *Characterization of Materials*. 1st ed. John Wiley & Sons.

Knowles, C.R., Becker, T.H., Tait, R.B. (2012) Residual Stress Measurements and Structural Integrity Implications for Selective Laser Melted Ti-6Al-4V. *South African Journal of Industrial Engineering*. **23**(3), 119–129.

Korsunsky, A.M., Sebastiani, M., Bemporad, E. (2009) Focused ion beam ring drilling for residual stress evaluation. *Materials Letters*. **63**(22), 1961–1963.

Korsunsky, A.M., Sebastiani, M., Bemporad, E. (2010) Residual stress evaluation at the micrometer scale : Analysis of thin coatings by FIB milling and digital image correlation. *Surface & Coatings Technology*. **205**(7), 2393–2403.

Lim, G., Lau, K., Cheng, W.S., Chiang, Z., Krishnan, M., Ardi, D.T. (2017) Residual Stresses in Ti-6Al-4V Parts Manufactured by Direct Metal Laser Sintering and Electron Beam Melting. In *British Society of Strain Meaurement*.

Lord, J.D., Penn, D., Whitehead, P. (2008) The Application of Digital Image Correlation for Measuring Residual Stress by Incremental Hole Drilling. , 65–73.

Malesa, M., Kujawińska, M., Malowany, K., Lusa, T. (2015) Application of Multi-camera DIC System for Measurements of Industrial Structures. *Procedia Engineering*. **114**, 453–460.

Mathews, J.H., Fink, K.D. (2004) Approximating the Derivative. In *Numerical Methods Using Matlab*. Upper Saddle River, New Jersey, USA: Prentice-Hall Inc., pp. 323–342.

Mercelis, P., Kruth, J.-P. (2006) Residual stresses in selective laser sintering and selective laser melting. *Rapid Prototyping Journal*. **12**(5), 254–265.

Murr, L.E., Gaytan, S.M., Ramirez, D.A., Martinez, E., Hernandez, J., Amato, K.N., Shindo, P.W., Medina, F.R., Wicker, R.B. (2012) • Invited Review Metal Fabrication by Additive Manufacturing Using Laser and Electron Beam Melting Technologies. *Journal of Materials Science & Technology*. **28**(1), 1–14.

de Oliveira, U., Ocelík, V., De Hosson, J.T.M. (2006) Residual stress analysis in Co-based laser clad layers by laboratory X-rays and synchrotron diffraction techniques. . **201**, 533–542.

Park, M.J., Yang, H.N., Jang, D.Y., Kim, J.S., Jin, T.E. (2004) Residual stress measurement on welded specimen by neutron diffraction. . **156**, 1171–1177.

Parry, L., Ashcroft, I.A., Wildman, R.D. (2016) Understanding the effect of laser scan strategy on residual stress in selective laser melting through thermo-mechanical simulation. *Additive Manufacturing*. **12**, 1–15.

Qiu, C., Adkins, N.J.E., Attallah, M.M. (2013) Microstructure and tensile properties of selectively laser-melted and of HIPed laser-melted Ti-6Al-4V. *Materials Science and Engineering A*. **578**, 230–239.

Rack, H.J., Qazi, J.I. (2006) Titanium alloys for biomedical applications. *Materials Science and Engineering C*. **26**(8), 1269–1277.

Reyntjens, S., Puers, R. (2001) A review of focused ion beam applications in microsystem technology. *Journal of Micromechanics and Microengineering*.

11(4), 287–300.

Sabate, N., Vogel, D., Keller, J., Gollhardt, A., Marcos, J., Cane, C., Michel, B., Gra, I. (2007) FIB-based technique for stress characterization on thin films for reliability purposes. . **84**, 1783–1787.

Sebastiani, M., Eberl, C., Bemporad, E., Pharr, G.M. (2011) Depth-resolved residual stress analysis of thin coatings by a new FIB – DIC method. *Materials Science & Engineering A*. **528**(27), 7901–7908.

Shiomi, M., Osakada, K., Nakamura, K., Yamashita, T., Abe, F. (2004) Residual stress within metallic model made by selective laser melting process. In *CIRP Annals*- …. pp. 3–6.

Simiprof (2015) File:Rezidual Stress.JPG - Wikimedia Commons. [online]. Available from: https://commons.wikimedia.org/wiki/File:Rezidual_Stress.JPG [Accessed July 27, 2017].

Song, X., Yeap, K.B., Zhu, J., Belnoue, J., Sebastiani, M., Bemporad, E. (2011) Residual stress measurement in thin films using the semi- destructive ring-core drilling method using Focused Ion Beam. *Procedia Engineering*. **10**, 2190–2195.

Stacey, A., MacGillivary, H.J., Webster, G.A., Webster, P.J., Ziebeck, K.R.. (1985) Measurement of residual stresses by neutron diffraction. *Journal of Strain Analysis*. **20**(2), 93–100.

Thöne, M., Leuders, S. (2012) Influence of heat-treatment on Selective Laser Melting products – e.g. Ti6Al4V. In *SFF, Austin Texas*. Austin Texas, pp. 492–498.

Turner, I.Y., Thompson, D.C., Wood, K.L., Crawford, R.H. (1998) Characterization of Surface Fault Patterns with Application to a Layered Manufacturing Process. *Journal of Manufacturing Systems*. **17**(1), 23–36.

Volkert, C.A., Minor, A.M. (2007) Focused Ion Beam Microscopy and Micromachining. *MRS Bulletin*. **32**(5), 389–399.

Vrancken, B., Cain, V., Knutsen, R., Van Humbeeck, J. (2014) Residual stress via the contour method in compact tension specimens produced via selective laser melting. *Scripta Materialia*. **87**, 29–32.

Winiarski, B., Withers, P.J. (2010) Mapping residual stress profiles at the micron scale using FIB micro- hole drilling. , 267–272.

Winiarski, B., Withers, P.J. (2012) Micron-Scale Residual Stress Measurement by Micro-Hole Drilling and Digital Image Correlation. *Experimental Mechanics*. **52**(4), 417–428.

Withers, P.J., Bhadeshia, H.K.D.H. (2001a) Residual stress. Part 2 – Nature and origins. *Materials Science and Technology*. **17**(4), 366–375.

Withers, P.J., Bhadeshia, H.K.D.H. (2001b) Residual stress Part 1 – Measurement techniques. *Materials Science and Technology*. **17**(4), 355–365.

Wong, K. V, Hernandez, A. (2012) A Review of Additive Manufacturing. . **2012**.

Wu, A.S., Brown, D.W., Kumar, M., Gallegos, G.F., King, W.E. (2014) An Experimental Investigation into Additive Manufacturing-Induced Residual Stresses in 316L Stainless Steel. *Metallurgical and Materials Transactions A: Physical Metallurgy and Materials Science*. **45**(13), 6260–6270.

Yadroitsev, I., Yadroitsava, I. (2015) Evaluation of residual stress in stainless steel 316L and Ti6Al4V samples produced by selective laser melting Evaluation of residual stress in stainless steel 316L and Ti6Al4V samples produced by selective laser melting This paper investigates the residua. *Virtual and Physical Prototyping*. **10**(July), 67–76.

Yates, J.R., Zanganeh, M., Tai, Y.H. (2010a) Quantifying crack tip displacement fields with DIC. *Engineering Fracture Mechanics*. **77**(11), 2063–2076.

Yates, J.R., Zanganeh, M., Tai, Y.H. (2010b) Quantifying crack tip displacement fields with DIC. *Engineering Fracture Mechanics*. **77**(11), 2063–2076.

Zaeh, M.F., Branner, G. (2009) Investigations on residual stresses and deformations in selective laser melting. *Production Engineering*. **4**(1), 35–45.

Appendix A The $\sin^2\psi$ method of calculating stress

Using the modified χ-method the specimen is tilted through a number of χ angles while maintaining a single ϕ angle. At each χ angle the diffraction peak is captured. If two detectors are used, then each detector captures a diffraction peak.

The steps followed to use the $\sin^2\psi$ method to calculate stress are as follows:

1. The 2θ location of the reference peak position for each detector is calculated at $\chi = 0°$. This peak position is shown in the first two peak plots at increment 0, at $\phi = 0°$ in Figure 8.1.

2. Bragg's Law is used to calculate the spacing at $\chi = 0°$ using the 2θ location from each detector. The results are averaged to determine the reference spacing

3. The specimen is tilted to a number of χ angles and the shift in the peak position from the reference position captured by each detector is calculated.

4. Using Bragg's Law the peak position shifts are related to a change in d-spacing. The change in d-spacing measured by each detector is averaged and the d-spacing at a particular χ angle is calculated. The measured shifts and calculated d-spacing values can be seen in Table A.1.

5. A plot of d-spacing vs $\sin^2\chi$ is generated (χ and ψ are equivalent for the modified χ-method) and a linear function is fitted to the data as seen in Figure 8.4.

6. The gradient of the black line in Figure 8.4 is calculated. This gradient is the average lattice strain measured.

7. The stress in the particular angle ϕ can then be calculated using Equation (A.**1**).

$$\sigma_\phi = \left(\frac{E}{1+\nu}\right) m, \tag{A.1}$$

where, m is the gradient of the black line in the d vs $\sin^2\chi$ graph and E and ν are the materials Young's Modulus and Poisson's Ratio, respectively.

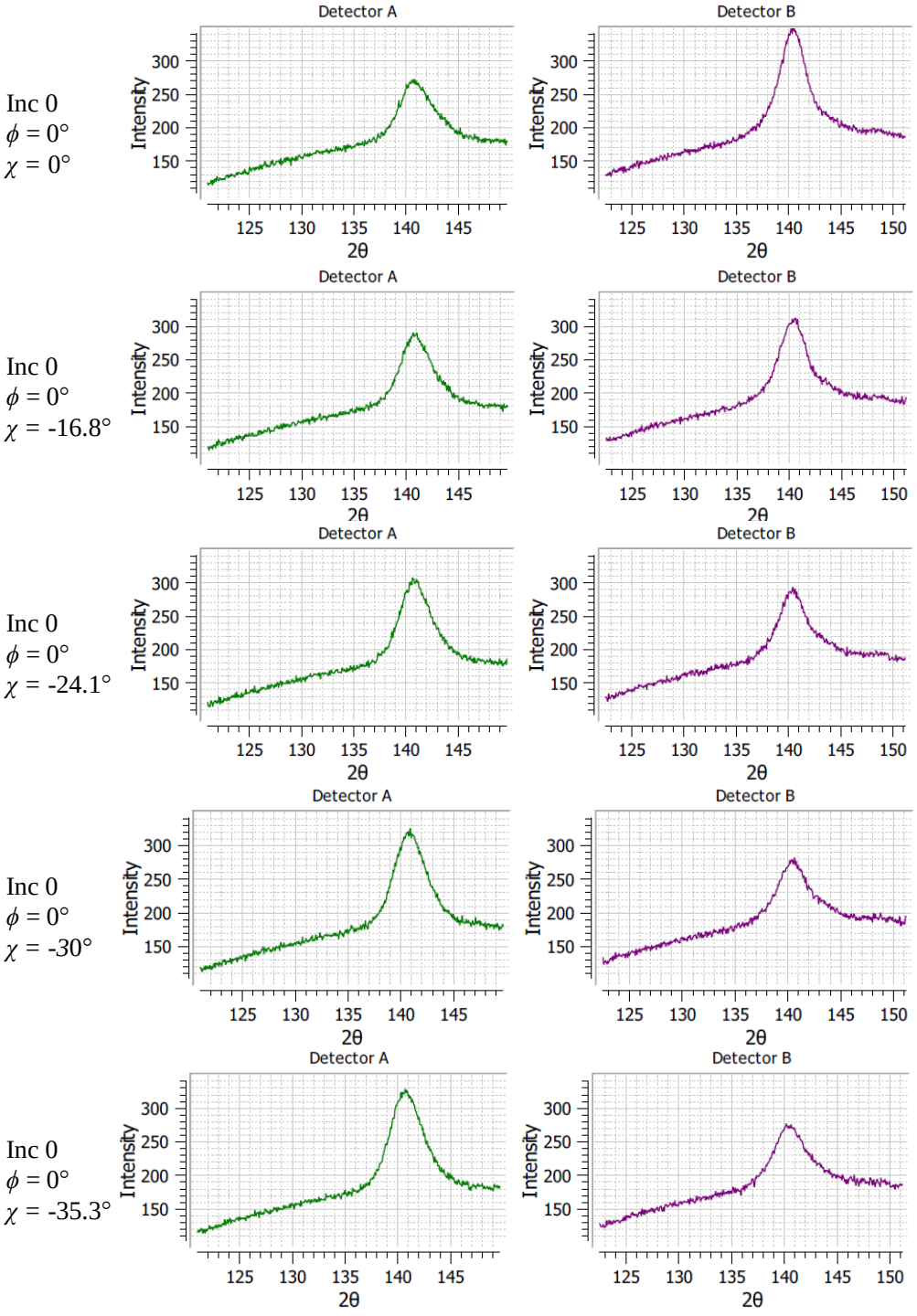

Figure 8.1 Diffraction peaks detected at Chi tilts 1-5 for depth increment 0 at ϕ = 0° in Specimen 160.

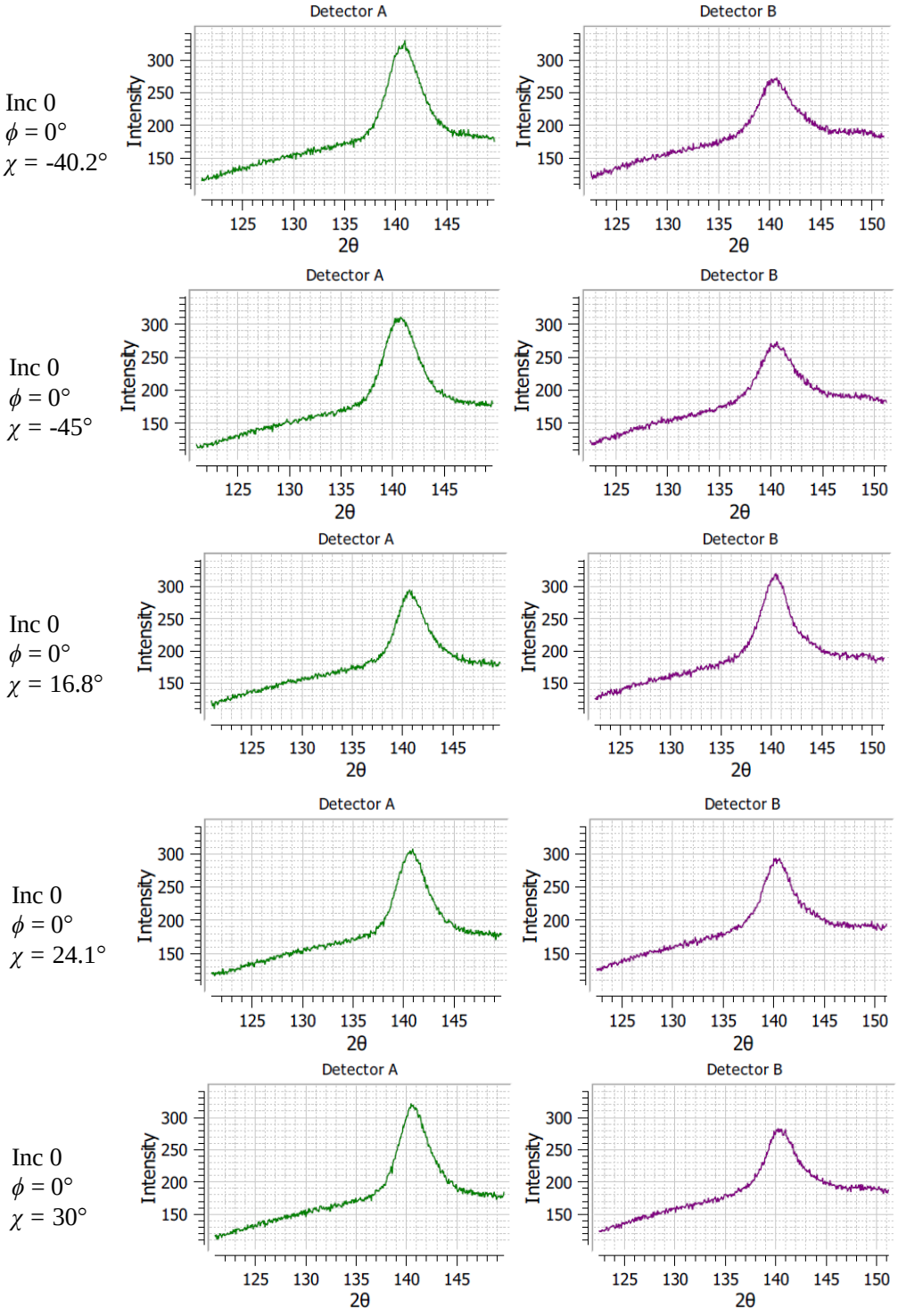

Figure 8.2 Diffraction peaks detected at Chi tilts 6-10 for depth increment 0 at ϕ = 0° in Specimen 160.

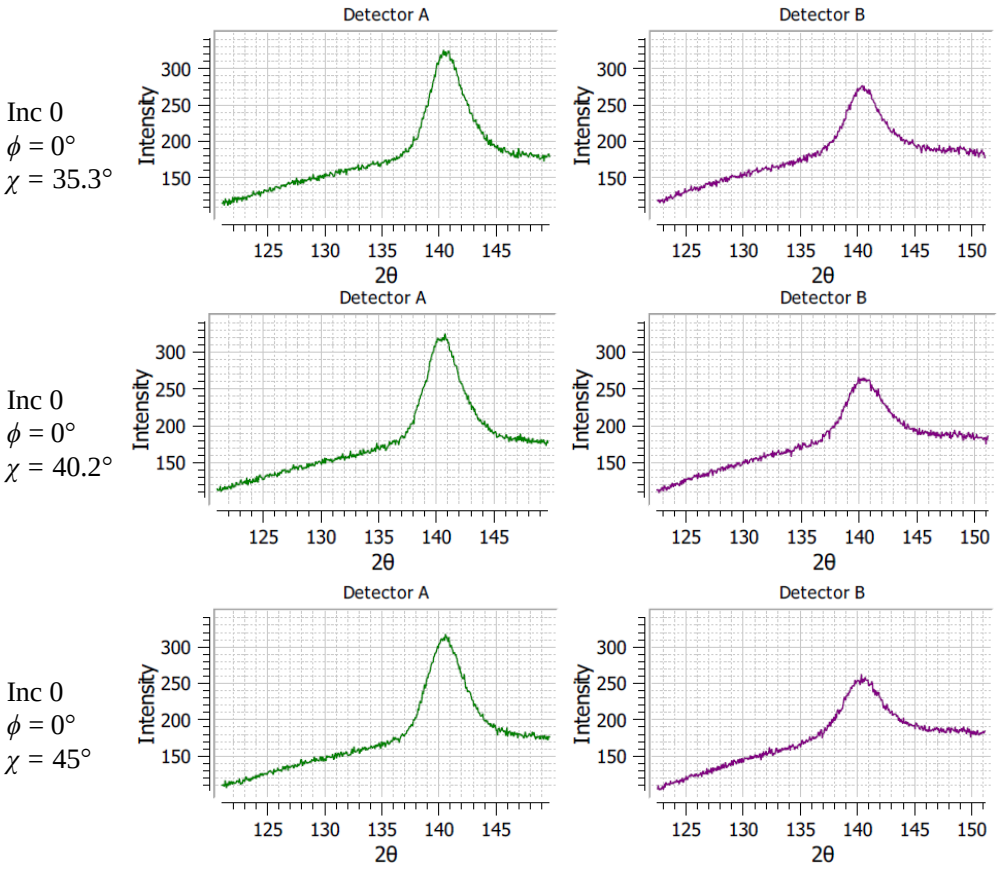

Figure 8.3 Diffraction peaks detected at Chi tilts 11-13 for depth increment 0 at ϕ = 0° in Specimen 160.

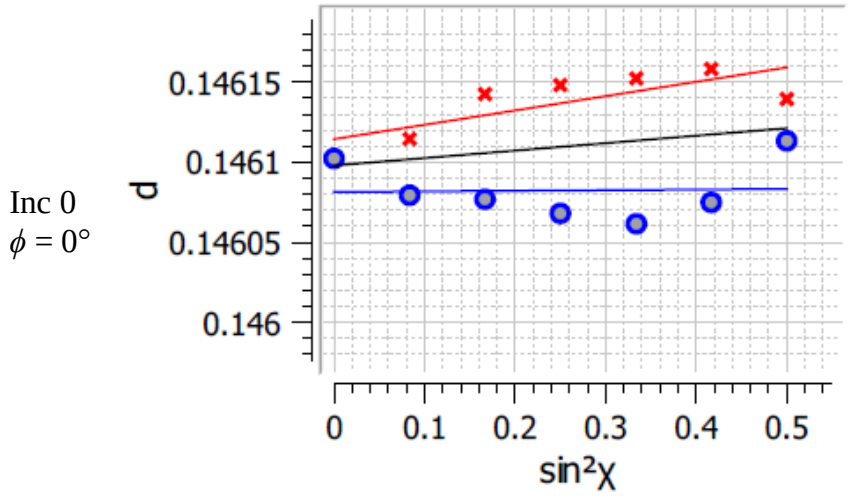

Figure 8.4 d vs $\sin^2\chi$ plot for depth increment 0 at at ϕ = 0° in Specimen 160. Red markers are for positive Chi angles, blue markers are for negative Chi angles and th black line is the average relationship between d and $\sin^2\chi$

Table A.1 Diffraction peak shift measured by each detector and d-spacing at each Chi tilt for depth increment 0 at ϕ = 0° in Specimen 160.

χ	Shift A (°)	Shift B (°)	d
0	0	0	0.1460673
-16.8	0.07	-0.08	0.1460705
-24.1	0.05	-0.14	0.1460885
-30	0.07	-0.08	0.1460693
-35.3	-0.03	-0.11	0.1460997
-40.2	-0.03	-0.08	0.1460930
-45	-0.04	-0.06	0.1460914
16.8	-0.03	-0.09	0.1460959
24.1	0	-0.15	0.1461005
30	-0.1	-0.06	0.1461047
35.3	-0.18	-0.04	0.1461170
40.2	-0.25	-0.14	0.1461560
45	-0.26	-0.09	0.1461479

Appendix B FIB milling and SEM imaging

B.1 FIB milling

The FIB, or focused ion beam, is a device that is typically used for surface erosion at the micro- or nano-scale. It can used in conjunction with a SEM as a dual beam device, in which the electron and ion beams intersect at a 52° angle and are coincident at a point known as the eucentric point. This configuration allows for the high definition imaging capabilities of a SEM to be coupled with the material removal abilities of the FIB. A schematic of a dual beam device can be seen in Figure 8.5. The FIB operates in a similar fashion to an electron beam except that uses highly energized, charged particles, or ions, instead of electrons. The ion beam has multiple uses including imaging, micro-milling and film (Volkert and Minor, 2007). In recent years FIB has become very popular for use in the semiconductor and chip design industries due to its ability to remove or deposit conductor or insulator material at nanometer precision (Reyntjens and Puers, 2001).

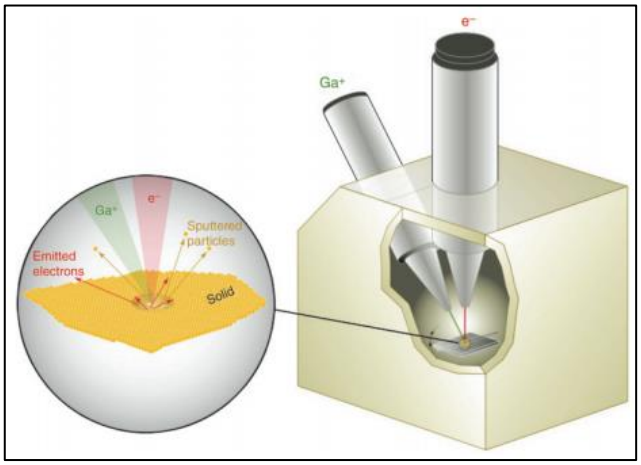

Figure 8.5 A SEM-FIB duel beam device (Volkert and Minor, 2007).

Most modern FIB columns use a liquid-metal ion source (LMIS) as this produces the brightest and most focused ion beam. The most commonly used source material is Gallium as it has a low melting temperature, low volatility and low vapor pressure, thus making the LMIS more stable, easier to design and operate than with other ion sources (Volkert and Minor, 2007).

During operation, a strong electric field to the LMIS which causes positively charged ions to be emitted from a liquid Gallium cone, which is formed at the tip of a Tungsten needle (Reyntjens and Puers, 2001). A schematic of a FIB column

is shown in Figure 8.6. The Gallium source emits the ion beam which is initially refined through the spray aperture. The upper octopole is a collection of electromagnets that adjust the beams stigmatism, or focal point. The beam current is controlled through the variable aperture and shut off by the blanking aperture. The raster scanning of the surface of the material is controlled by the lower octopole and the beam is focused to a fine stop by the second electrostatic lens. The multichannel plate (MCP) is used to collect secondary particles for imaging purposes, similar to the use of a secondary electron sensor in a SEM (Reyntjens and Puers, 2001). Depending on the beam current chosen, the FIB is able either to image the surface at a high resolution or perform precise milling procedures on the sample surface.

A gas injection source can also be implemented for chemical vapor deposition, where a specifically selected precursor gas is injected into the vicinity of the ion beam and the non-volatile components of the gas, typically Tungsten, Platinum or Carbon are deposited on the sample surface. The volatile components are extracted by a vacuum system. These layers can be deposited for either surface protection from ion damage or to provide a conductive surface on a non-conductive sample. A schematic of the various processes is shown in Figure 8.7.

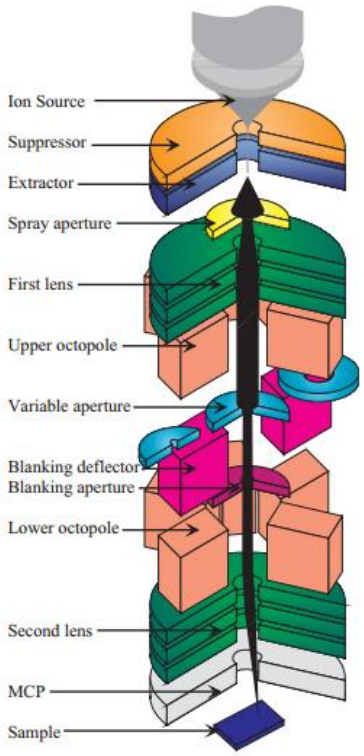

Figure 8.6 Schematic of a typical FIB column (Reyntjens and Puers, 2001).

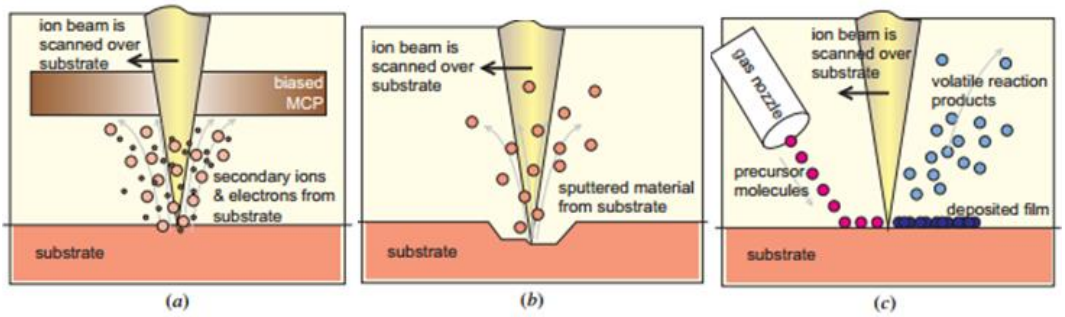

Figure 8.7 FIB processes. a) imaging. b) milling. c) deposition (Reyntjens and Puers, 2001).

Material removal with the FIB is performed using a high beam current. The strength of this current is dependent on the material to be milled, the size of the milled area and the depth of each milling step. When the highly energized ion impinges on the surface of the material it transfers its kinetic energy to the sample atoms. Various processes occur due to this energy transfer including electron and ion emission, atomic sputtering, sample heating and surface damage (Volkert and Minor, 2007). It is the sputtering action of the ion beam that allows it to perform the material removal process. As the electrons are ejected from the sample material, the material erodes in the vicinity of the ion beam tip. The rate at which the material is sputtered depends on the beam current and the material properties. Material re-deposition, which is unavoidable in the milling process, also acts to reduce the rate of erosion. The conic shape of the ion beam as well as this re-deposition is a reason that completely vertical side walls cannot be milled unless the sample is tilted to a high angle (Volkert and Minor, 2007).

Figure 8.8 shows the effects of using two different milling strategies at the grain boundary of a Cu sample. Each of the milled areas was exposed to the same cumulative ion dose. Using a slow, single pass, milling step the trench formed was deeper, but the large amount of material re-deposition caused the side walls to be thick and highly sloped. When a more rapid, multi pass, milling procedure was used the side walls are less affected by re-deposition, however there is a step in the milling trench due to the darker grain having a lower erosion rate (Volkert and Minor, 2007).

Along with material re-deposition there are other problems associated with the use of FIB milling, namely ion beam damage and ion beam heating. As ions penetrate into the material surface they cause a cascade effect of releasing (sputtering) and migrating electrons, this causes an area of damage surrounding the implantation region of the ion. This area is called a cascade region and when multiple regions overlap an area of surface damage is formed. This damage can be in the form of grain modification, phase formation, surface amorphization or dislocation formation depending on the sample material and temperature (Volkert and Minor, 2007). Ion beam heating is caused due to the fact that almost all of the ion's

kinetic energy is converted to heat when it impinges on the surface of the sample. This heating is dependent on the sample material, beam current, dwell duration and sample geometry and in some situations can cause unacceptable degrees of heating of the sample that may change the characteristics of the material or even burn the material (Volkert and Minor, 2007).

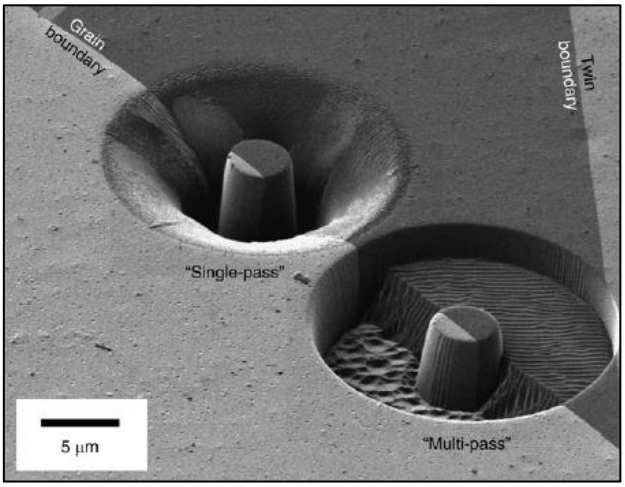

Figure 8.8 Different milling strategies at a grain boundary (Volkert and Minor, 2007)

B.2 SEM imaging

A SEM is a type of microscope used to capture images at a very high magnification, typically from 3 x up to 150 000 x magnification. Detailed information about the topographical features of the material, phase distribution, crystal structure, chemical composition, and many other physical characteristics may be captured through the use of SEM imaging (Kaufmann, 2003). Due to the way in which the lenses of the SEM are used to demagnify and focus the electron beam 3-dimensional information can be extracted as a result of the relatively high depth of field achievable using SEM imaging. The use of a SEM allows for much finer details to be captured than with the use of optical microscopy. A field emission electron gun SEM (FEGSEM) is able to resolve details on the scale of 1 nm (Kaufmann, 2003).

Typically a SEM uses a tungsten or lanthanum hexaboride filament cathode to thermoionically emit electrons. This is done by heating the filament by passing an electrical current through it. The emission of the electrons from the filament is performed in a high vacuum to prevent oxidation of the filament material. A third type of electron gun is the field emission electron gun, which provides much

higher brightness and correspondingly an increase in image resolution (Kaufmann, 2003).

Electromagnets are used to focus and position the electron beam probe on the surface of the material. It is these electromagnets that control the movement of the beam along the surface. Scanning is typically performed in a raster grid fashion in order to generate an image.

When the electron beam impinges on the surface of the sample there is both elastic and inelastic interactions between the electron beam and the sample surface. Inelastic interactions result in a transferal of energy from the beam to the sample, whereas elastic interactions result in no loss in energy for the beam electrons, but a change in trajectory. As a result of these two types of interactions, there are two types of electron signals that are sensed by the SEM. Secondary electrons (SE's) are electrons that are ejected from the surface atoms of the sample due to inelastic interactions between the electron beam and the sample material. These electrons are typically low energy electrons, with energies of less than 50 eV. Backscatter electrons (BSE's) are electrons that originated from the electron beam which have had their trajectory changed due to elastic interactions with the surface of the sample. These electrons have a much higher energy than SEs and make up the majority of the electrons emitted from the sample (Kaufmann, 2003).

A schematic of a SEM column can be seen in Figure 8.9. The deflection coils are the electromagnets that control the position at which the beam impinges on the sample.

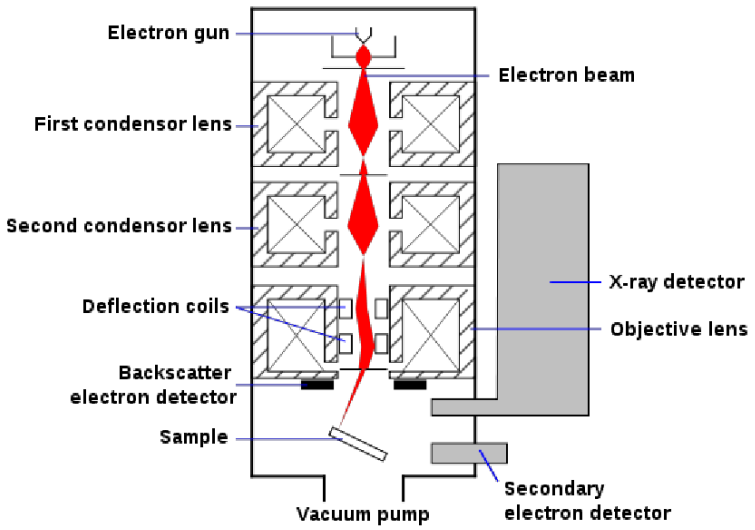

Figure 8.9 Schematic of a SEM column (Abudayyeh, 2012).

The generation of SEs is concentrated around the electron probe diameter and as a result produce a higher resolution image that BSEs and produce an image of the specimen morphology. The intensity of the BSE signal is a function of the sample material's atomic number and as such BSEs are useful for generating composition images. As the change in electron trajectory is also a function of the angle of incidence between the electron beam and the sample surface, BSEs also give information about the topology of the material (Kaufmann, 2003). As seen in Figure 8.9a typical SEM is fitted with both a BSE detector and a SE detector. This coupling of image signals ensures that the most comprehensive image possible of the sample is generated. Detectors can be used individually in order to concentrate on a certain aspect of the image, such as composition, or may be used in conjunction to form a high resolution topographical image of the specimen.

Appendix C SEM micrographs and DIC displacement maps

C.1 SEM micrographs of the milled ring trench

The SEM image captured of each depth increment is shown in Figure 8.10 and Figure 8.11. Each milling increment increases the trench depth by ~2 µm

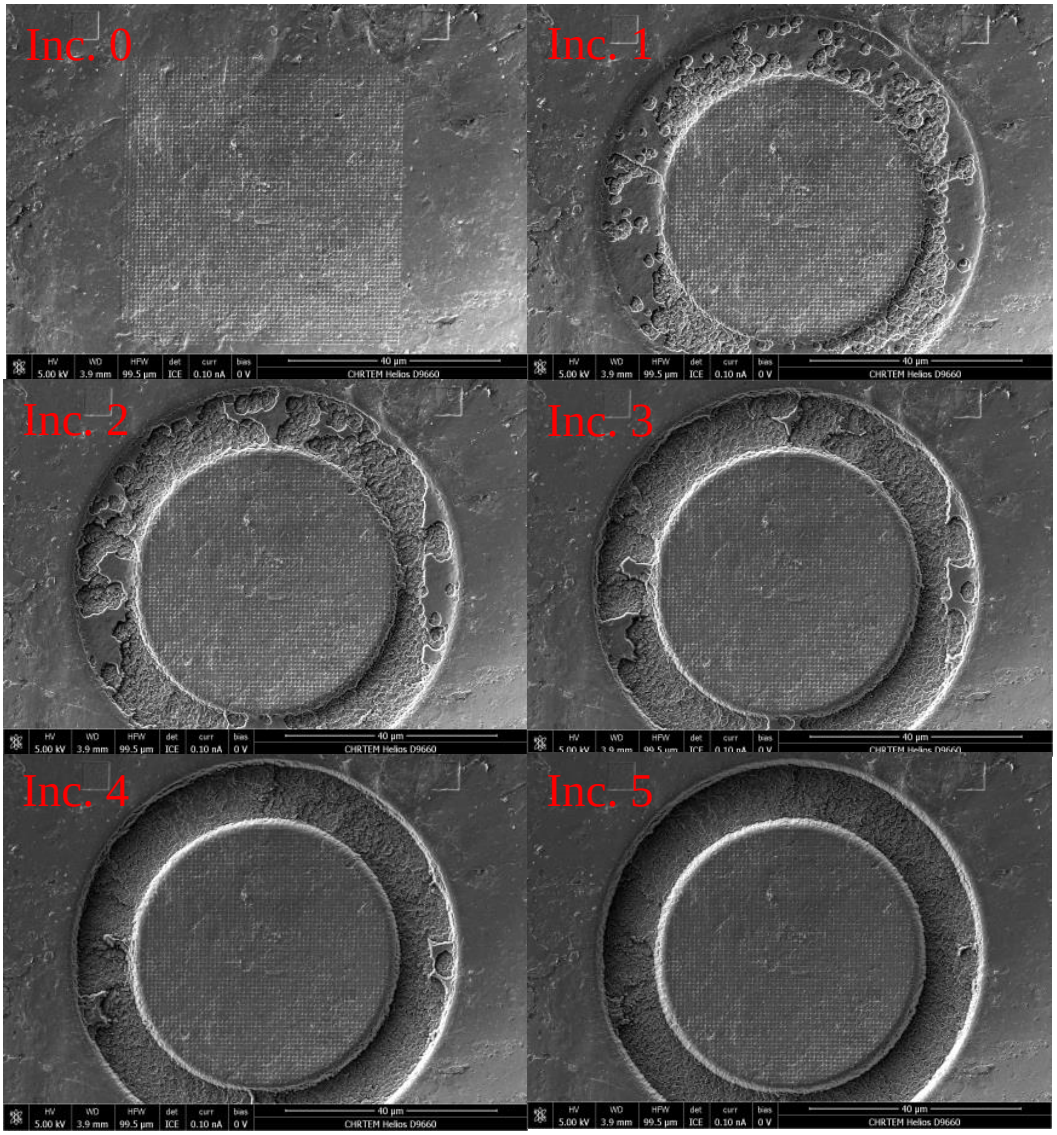

Figure 8.10 Milled ring trench from a depth of 0 µm to approximately 12 µm.

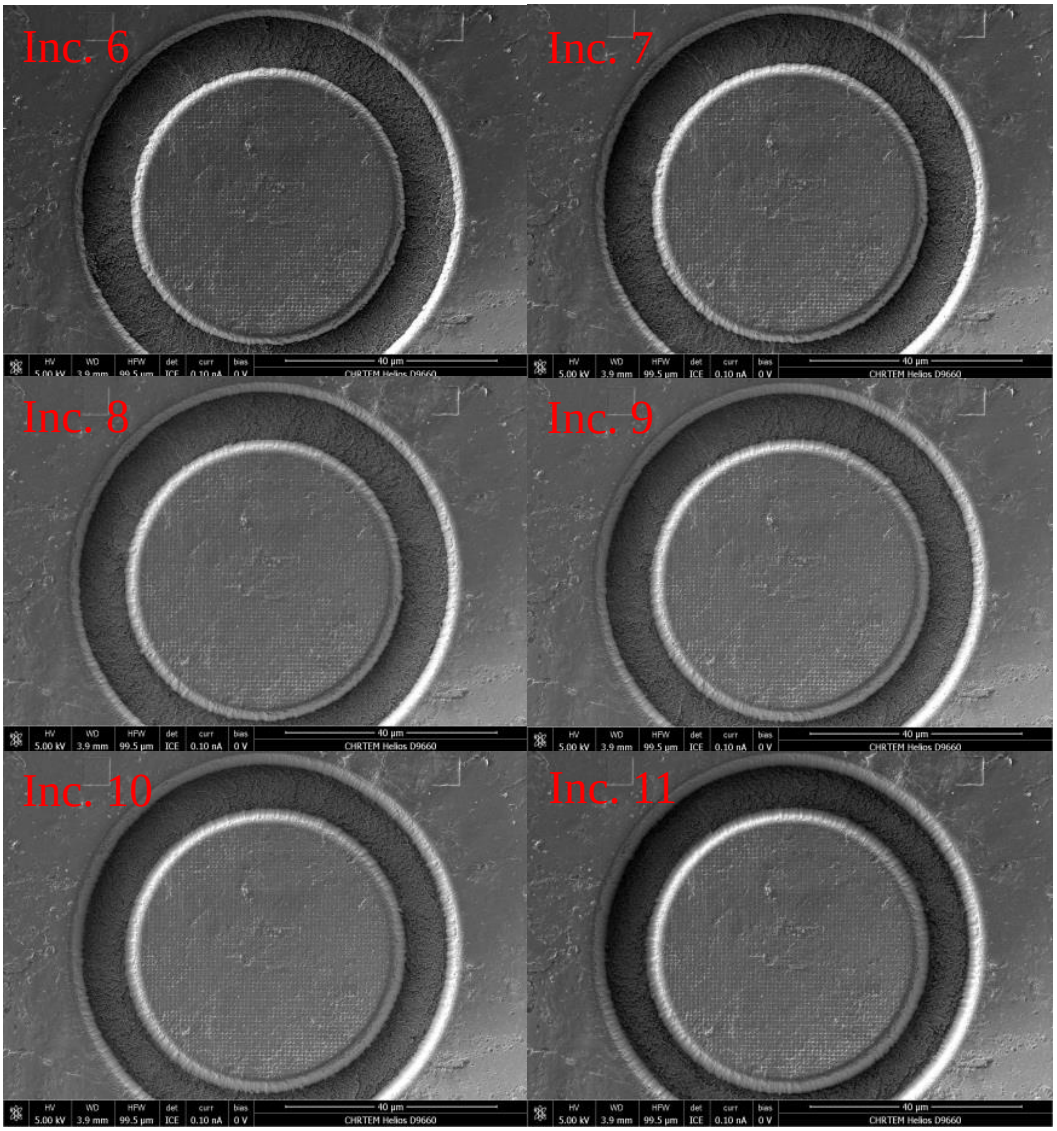

Figure 8.11 Milled ring trench from a depth of approximately 14 µm to approximately 22 µm.

C.2 Absolute displacement maps generated with DIC

It should be noted that the order of the images was reversed for the DIC analysis in order to define the masking region on the undamaged portion of the stub surface. Thus the measured displacement vectors are reversed from the physical displacements experienced by the material.

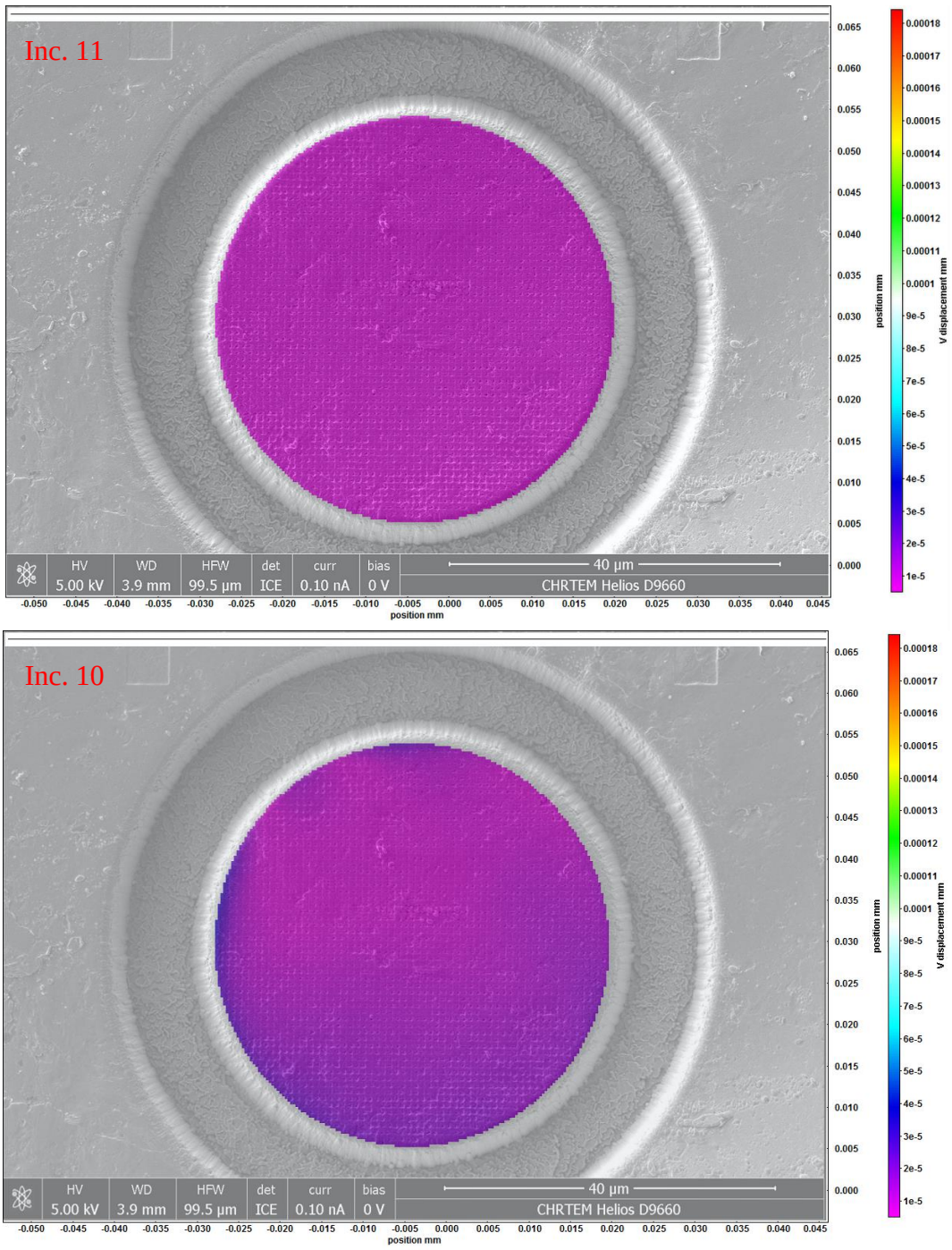

Figure 8.12 Absolute displacement over stub surface at increment 11 and 10, relative to increment 11

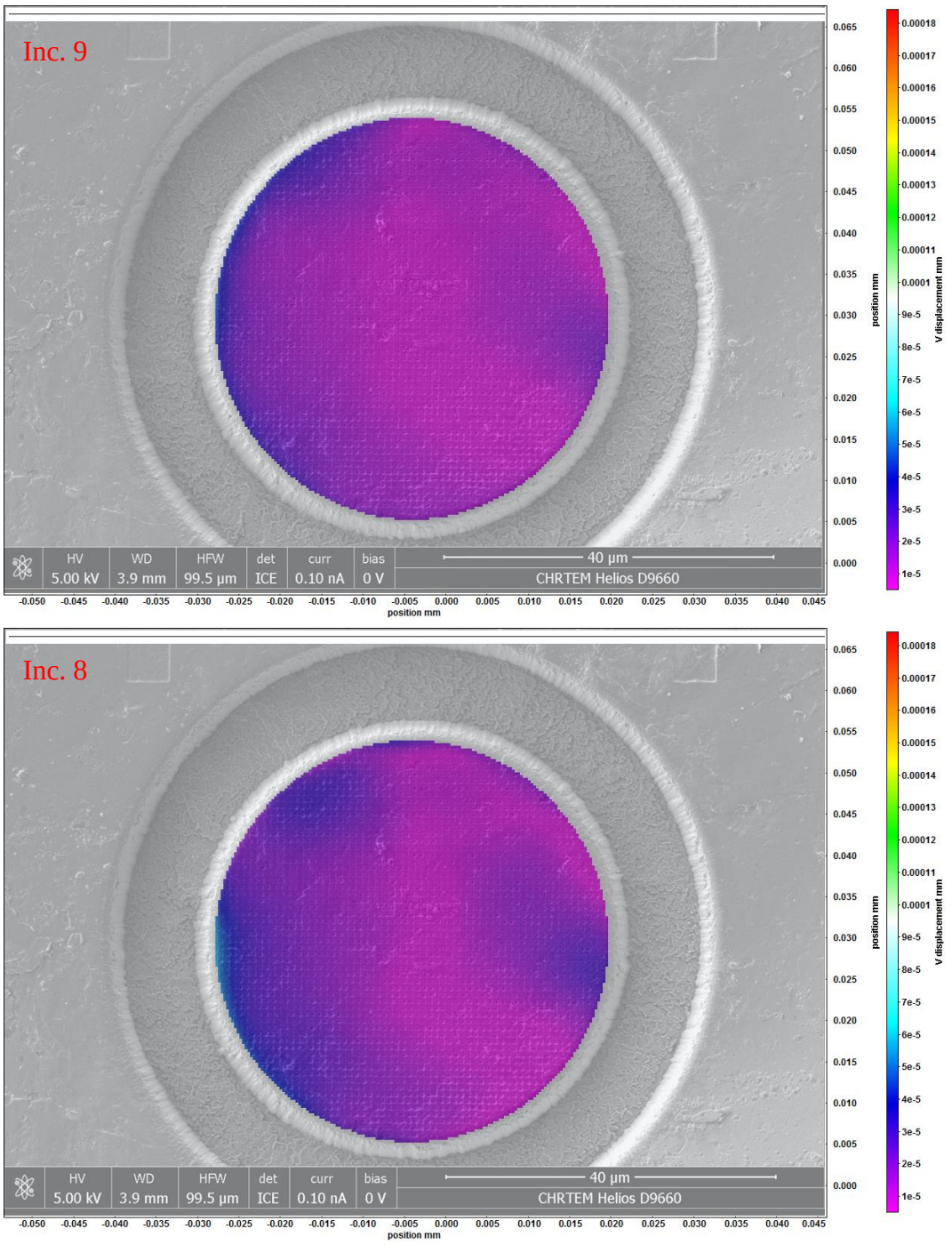

Figure 8.13 Absolute displacement over stub surface at increment 9 and 8, relative to increment 11

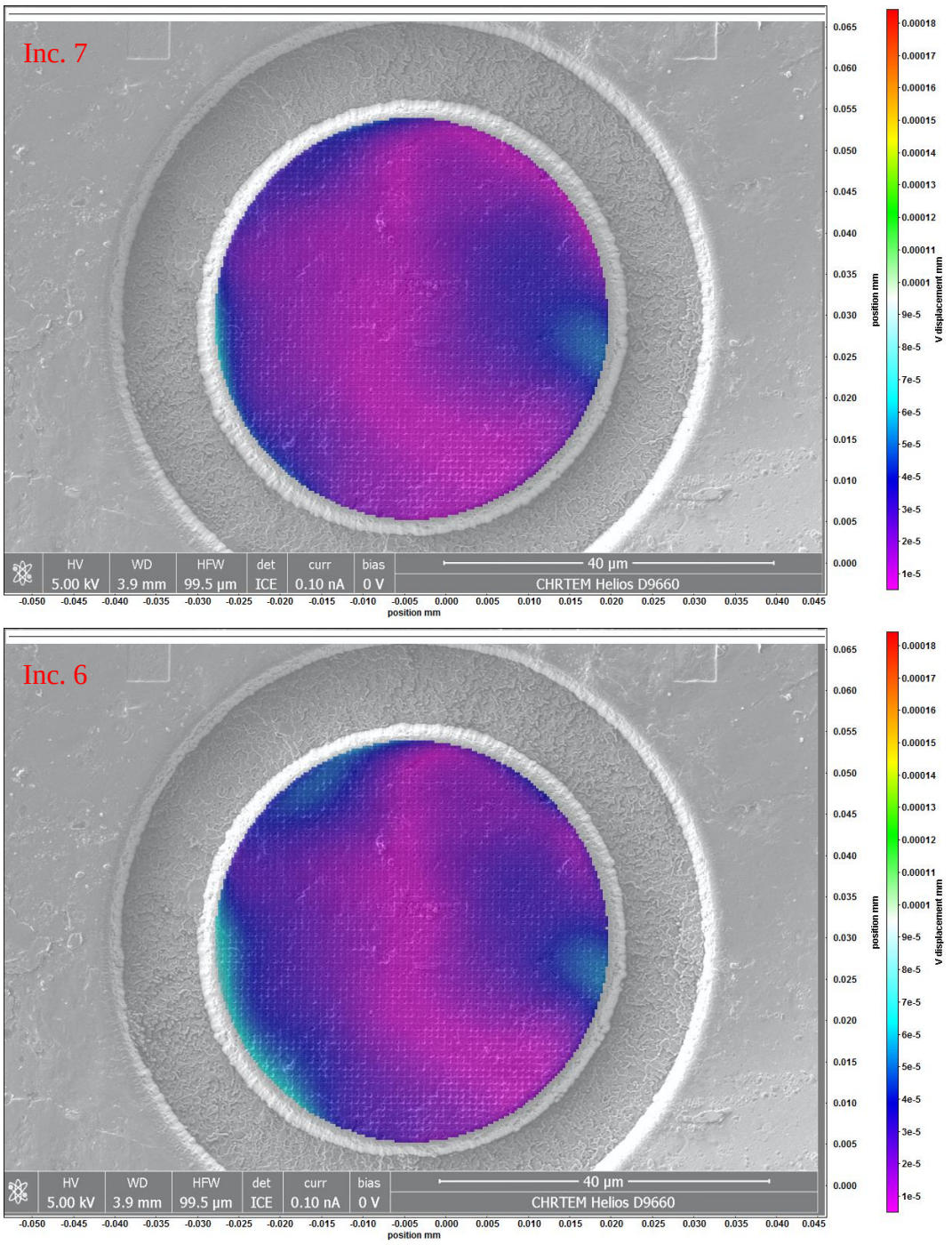

Figure 8.14 Absolute displacement over stub surface at increment 7 and 6, relative to increment 11

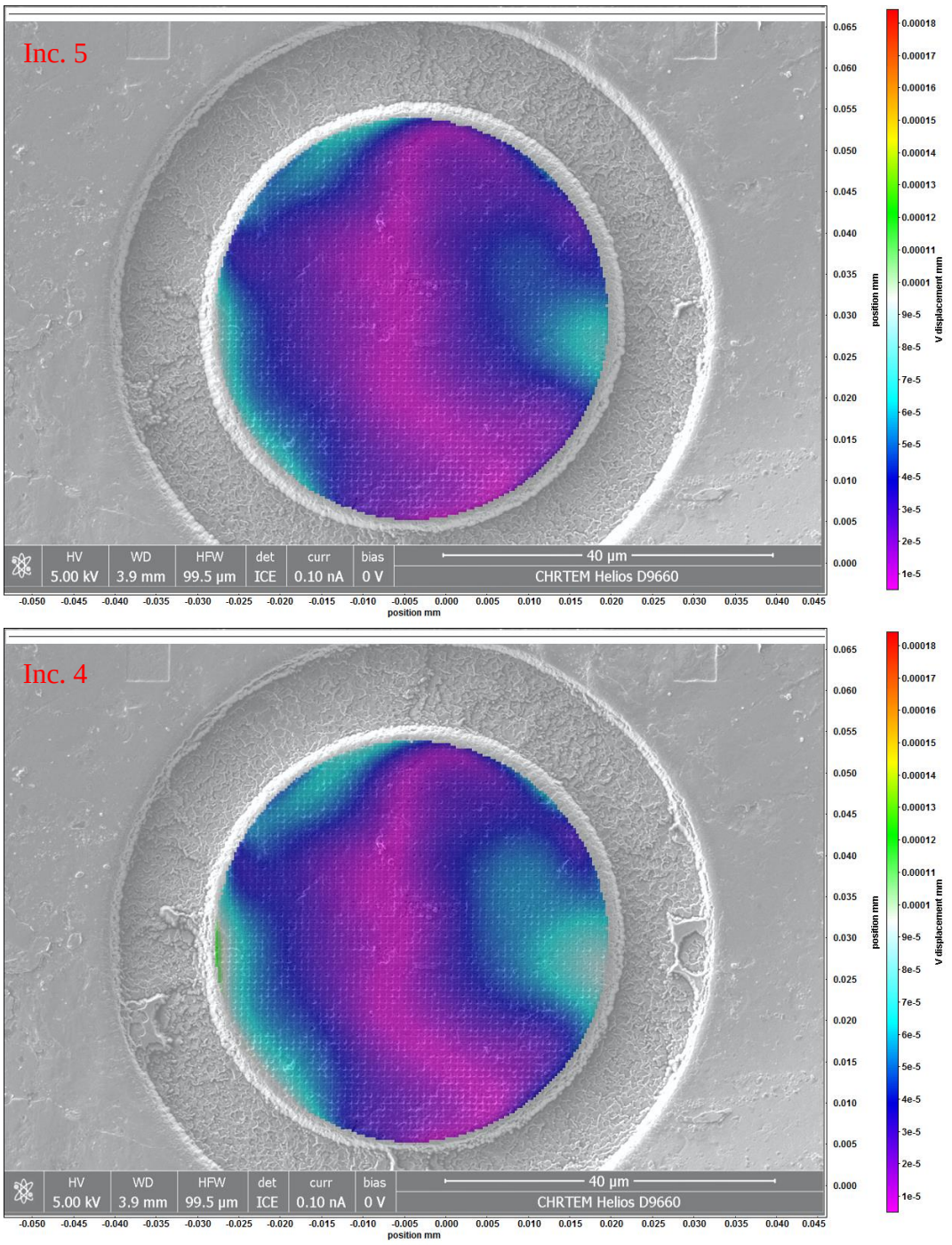

Figure 8.15 Absolute displacement over stub surface at increment 5 and 4, relative to increment 11

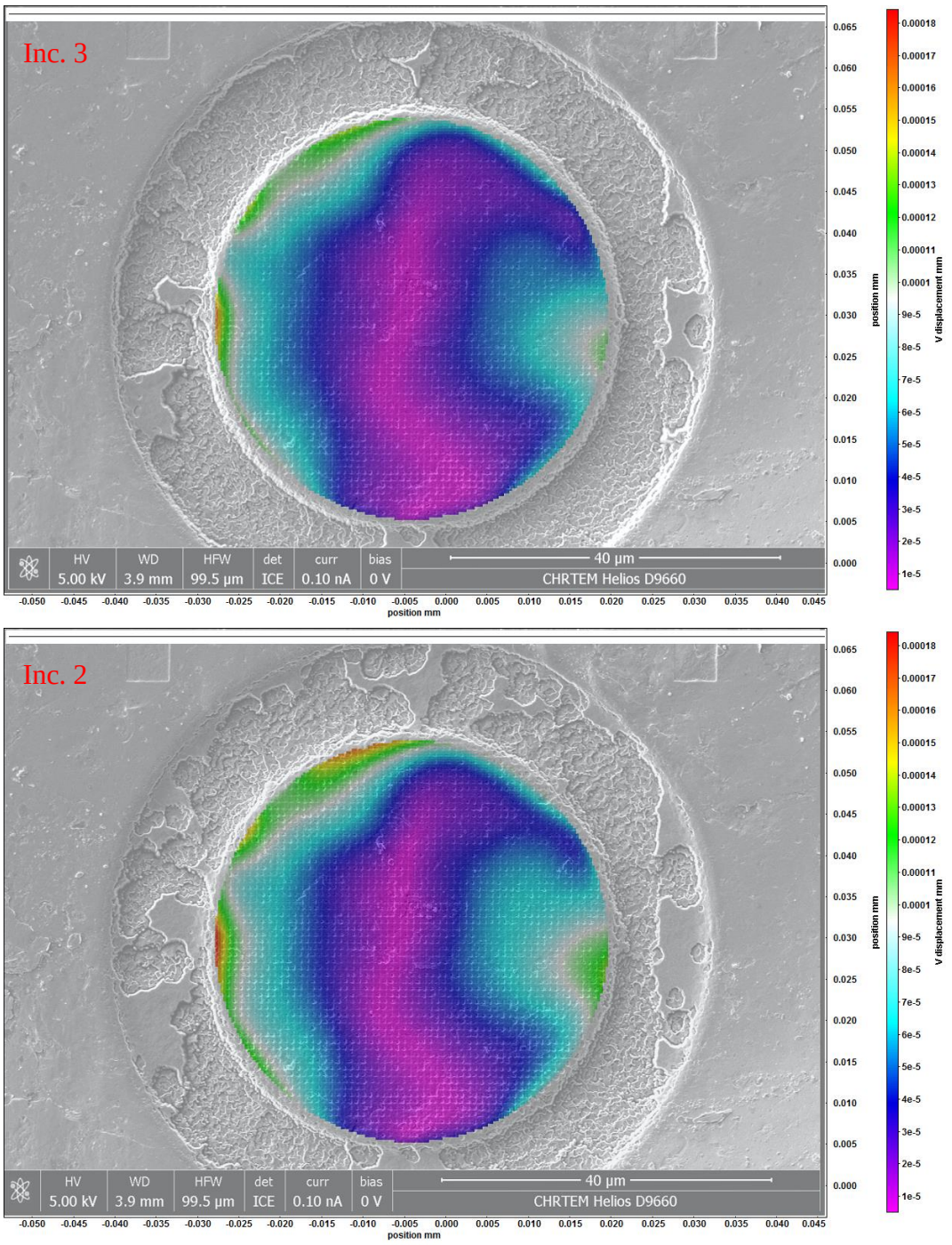

Figure 8.16 Absolute displacement over stub surface at increment 3 and 2, relative to increment 11

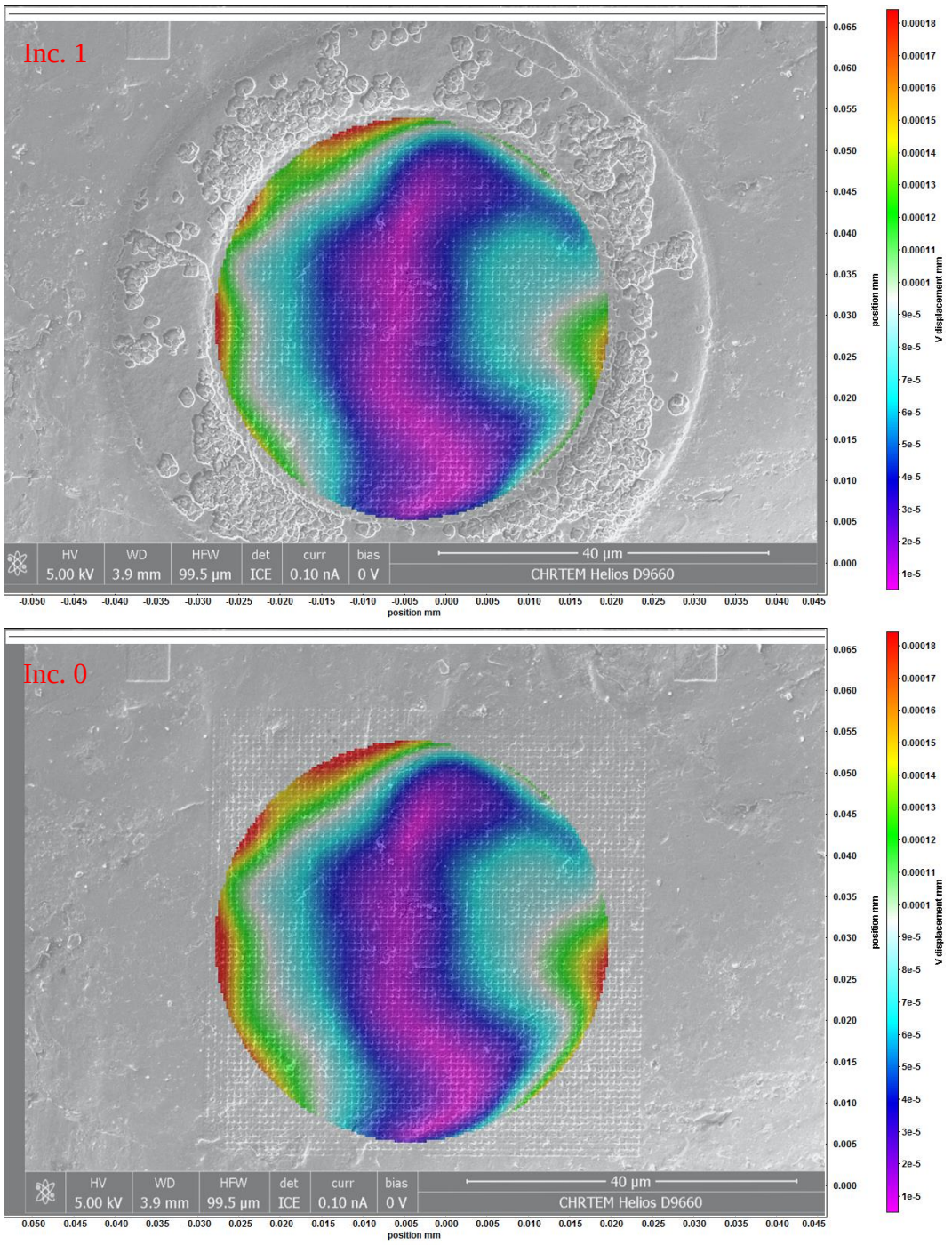

Figure 8.17 Absolute displacement over stub surface at increment 1 and 0, relative to increment 11

Appendix D MATLAB script for calculating strains

```
function [exx,eyy,exy]=getstrainLucas(imgno)

% Get TECplot data.
[pos,u,mask]=getDICdata(imgno);
datasize=[length(unique(pos(:,2))),length(unique(pos(:,1))),length
(unique(pos(:,3)))];

% Remove rigid body translation and rotation.
T=findtrans(pos,u);
tmpu = [u,ones(length(pos),1)]*T;
u = tmpu(:,1:3);

% Gridded format
POSX=reshape(pos(:,1),datasize);
POSY=reshape(pos(:,2),datasize);
POSZ=reshape(pos(:,3),datasize);
UX=reshape(u(:,1),datasize);
UY=reshape(u(:,2),datasize);
UZ=reshape(u(:,3),datasize);
MASK=reshape(mask,datasize);
MASK(MASK==0)=NaN;

% Show vector length plot.
f1=figure;
imagesc(POSX(:),POSY(:),sqrt(UX.^2+UY.^2).*MASK)
axis equal;
axis tight;
colorbar;
title('Select middle in region of interest.')
xlabel('x (mm)')
ylabel('y (mm)')

% Choose centre point.
[midposx,midposy]=ginput(1);
[~,ind] =
min(bsxfun(@minus,pos,[midposx,midposy,0]).^2*ones(3,1),[],1);
[ii,jj,kk]=ind2sub(datasize,ind);
close(f1);

% Adjust data to centre point.
POSX=POSX-POSX(ii,jj,kk);
POSY=POSY-POSY(ii,jj,kk);
POSZ=POSZ-POSZ(ii,jj,kk);
UX=UX-UX(ii,jj,kk);
UY=UY-UY(ii,jj,kk);
UZ=UZ-UZ(ii,jj,kk);

% Gaussian weighting over middle of data.
W=exp(-((POSX/(0.25*range(POSX(:)))).^2)-
((POSY/(0.25*range(POSY(:)))).^2));
useind=find(mask);
```

```
% Surface fit to displacement data.
sfx=fit([POSX(useind),POSY(useind)],UX(useind),'poly11','exclude',
[],'Weights',W(useind));
sfy=fit([POSX(useind),POSY(useind)],UY(useind),'poly11','exclude',
[],'Weights',W(useind));
UXfit=sfx.p00+POSX.*sfx.p10+POSY.*sfx.p01;
UYfit=sfy.p00+POSX.*sfy.p10+POSY.*sfy.p01;

% Strain components.
exx=sfx.p10;
eyy=sfx.p01;
exy=(sfx.p01+sfy.p10)/2;

% Show fit in UX
figure;
hold on;
box on;
grid on;
surf(POSX,POSY,UX.*MASK)
mesh(POSX,POSY,UXfit.*MASK)
daspect([max(daspect)*[1 1],1]);
axis tight;
colorbar;
view(3);
title('Displacement in X')
xlabel('x (mm)')
ylabel('y (mm)')
zlabel('Displacement (mm)')

% Show fit in UY
figure;
hold on;
box on;
grid on;
surf(POSX,POSY,UY.*MASK)
mesh(POSX,POSY,UYfit.*MASK)
daspect([max(daspect)*[1 1],1]);
axis tight;
colorbar;
view(3);
title('Displacement in Y')
xlabel('x (mm)')
ylabel('y (mm)')
zlabel('Displacement (mm)')

disp(['Strain in xx: ',num2str(exx)])
disp(['Strain in yy: ',num2str(eyy)])
disp(['Strain in xy: ',num2str(exy)])
end

function [pos,u,mask] = getDICdata(imgno)
%GETDICDATA Loads displacment field from LaVision .dat files.
%   [posXdic,posYdic,posZdic,uXdic,uYdic,uZdic] =
GETDICDATA(imgno)
%   obtaines the positonal (pos),displacement (u) and mask (mask)
data from
```

```
%   LaVision DIC data for a filename format of B0000#. imgno is
the data
%   file number to be loaded.
%
%   fmt can be .txt or .dat - but .dat is the default (use Tecplot
in DaVis
%   export)
%
%   Thorsten Becker, Sept 2017.

% Load data according to LaVision convention: B00__#.dat.
filename = sprintf('B%3.5d.dat', imgno);
filedata = importdata(filename);
filedata = sortrows(filedata.data,1);

% Save to variables pos, u and mask.
pos(:,1)=filedata(:,1);
pos(:,2)=filedata(:,2);
pos(:,3)=zeros(size(pos(:,1)));
u(:,1)=filedata(:,3);
u(:,2)=filedata(:,4);
u(:,3)=zeros(size(pos(:,1)));
mask=filedata(:,5);
end

function T = findtrans(pos,u)
% FINDTRANS Find translation and rotation in displacement data.
%   FINDTRANS(pos,u) finds translation and rotation in
displacement data u.
%
%   Thorsten Becker, sept 2017.
pos0 = pos;
pos1 = pos+u;
H =
bsxfun(@minus,pos0,mean(pos0))'*bsxfun(@minus,pos1,mean(pos1));
[U,~,V] = svd(H);
R = V*U';
if det(R) < 0
    V(:,3) = -1;
    R = V*U';
end
t = mean(pos0)*-R+mean(pos1);
T  = [R',[0;0;0];-t*R',1];
end
```

Appendix E Neutron diffraction stress results

E.1 Stress measurements with calculated errors

Table E.1 σ_{xx} with standard deviation (MPa) for Specimen 130.

z-pos (mm) / x-pos (mm)	**1.70**	**3.15**	**4.60**	**6.05**	**7.50**
1.70	27.2 ± 28.5	-46.1 ± 28.6	-97.1 ± 28.1	8.5 ± 28.9	6.7 ± 28.7
3.36	-9.3 ± 28.5	-122.4 ± 29.1	-145.9 ± 27.9	-137.4 ± 29.7	40.2 ± 31.5
5.02	-117.1 ± 31.6	-72.6 ± 27.8	-119.7 ± 26.0	-88.3 ± 28.6	30.5 ± 28.6
6.68	-6.3 ± 29.2	-13.5 ± 30.0	-59.7 ± 27.8	-45.1 ± 28.2	107.3 ± 29.6
8.34	7.1 ± 30.9	-61.2 ± 27.6	-76.0 ± 27.8	-40.1 ± 29.6	-35.0 ± 30.6
10.00	-75.9 ± 30.6	-81.9 ± 28.2	-61.9 ± 28.7	-35.7 ± 31.5	28.3 ± 32.0
11.66	-63.7 ± 31.3	-42.4 ± 32.2	-72.0 ± 27.5	-0.5 ± 26.7	-44.6 ± 29.3
13.32	-35.7 ± 27.8	-108.9 ± 29.2	-135.0 ± 31.9	-59.8 ± 27.9	-20.4 ± 29.1
14.98	-194.7 ± 46.8	-132.0 ± 29.5	-172.6 ± 27.4	-151.9 ± 30.5	-53.7 ± 31.8
16.64	-88.2 ± 28.1	-134.1 ± 27.7	-149.3 ± 27.2	-125.8 ± 31.5	47.9 ± 31.5
18.30	20.3 ± 26.4	-10.9 ± 26.2	-50.7 ± 27.6	-69.0 ± 26.5	26.6 ± 28.7

Table E.2 σ_{yy} with standard deviation (MPa) for Specimen 130.

z-pos (mm) / x-pos (mm)	1.70	3.15	4.60	6.05	7.50
1.70	-17.2 ± 38.2	-58.0 ± 31.3	-106 ± 32.3	-95.5 ± 31.6	0.10 ± 31.4
3.36	-40.2 ± 31.1	-217 ± 32.1	-181 ± 32.7	-182 ± 32.1	65.2 ± 36.8
5.02	-123 ± 38.2	-169 ± 30.2	-231 ± 33.4	-167 ± 34.6	42.9 ± 35.1
6.68	-46.5 ± 36.2	-81.4 ± 33.1	-126 ± 33.8	-71.3 ± 31.9	197 ± 36.9
8.34	-13.0 ± 34.1	-95.2 ± 29.8	-184 ± 34.3	-109 ± 37.2	-15.2 ± 39.8
10.00	-102 ± 35.9	-144 ± 32.8	-122 ± 33.0	-70.3 ± 44.6	75.8 ± 43.5
11.66	-125 ± 35.0	-141 ± 36	-166 ± 32.3	-60.4 ± 32.8	4.8 ± 34
13.32	-77.0 ± 37.4	-222 ± 34.6	-259 ± 34.3	-136 ± 33.4	30.1 ± 33.6
14.98	-315 ± 88.9	-194 ± 31	-292 ± 31.9	-168 ± 30.1	29.3 ± 31.3
16.64	-102 ± 28.4	-172 ± 28.9	-183 ± 32.5	-111 ± 29.7	111 ± 35.9
18.30	-87.8 ± 26.5	-101 ± 29.5	-83.0 ± 30.0	-139 ± 28.2	-23.9 ± 33.2

Table E.3 σ_{zz} with standard deviation (MPa) for Specimen 130.

z-pos (mm) / x-pos (mm)	1.70	3.15	4.60	6.05	7.50
1.70	-67.9 ± 29.1	-76.5 ± 31.1	-157 ± 28.1	-27.1 ± 28.8	-50.2 ± 28.5
3.36	-81.9 ± 29.1	-151 ± 28.7	-133 ± 26.3	-128 ± 29.8	-11.6 ± 35.0
5.02	-143 ± 31.1	-51.1 ± 29.8	-59.5 ± 27.1	-45.8 ± 29.8	16.9 ± 30.2
6.68	-6.1 ± 30.4	67.6 ± 35.9	31.2 ± 28.6	104 ± 31.6	140 ± 32.9
8.34	26.5 ± 31.1	6.8 ± 29.2	56.1 ± 28.6	9.00 ± 29.6	0.30 ± 34.7
10.00	-97.3 ± 30.3	-44.3 ± 31.5	44.3 ± 30.0	70.4 ± 35.4	67.6 ± 35.9
11.66	-126 ± 30.3	1.40 ± 33.1	32.5 ± 26.7	88.0 ± 28.0	-31.8 ± 34.9
13.32	-28.7 ± 28.8	-81.8 ± 29.5	-26.3 ± 30.7	-6.40 ± 32.6	-4.6 ± 29.1
14.98	-242 ± 47.6	-114 ± 28.0	-161 ± 27.9	-96.0 ± 32.0	-54.9 ± 37.7
16.64	-186 ± 29.4	-200 ± 26.8	-177 ± 27.2	-146 ± 31.5	-66 ± 33.0
18.30	-86.0 ± 24.9	-17.7 ± 29.7	-84.6 ± 26.5	-98.3 ± 32.4	-68.8 ± 32.7

Table E.4 σ_{xx} with standard deviation (MPa) for Specimen 230.

z-pos (mm) / x-pos (mm)	1.70	3.15	4.60	6.05	7.50
1.70	-46.3 ± 29.5	-54.8 ± 21.5	-23.1 ± 21.2	-104 ± 22.3	-32.1 ± 24.6
3.36	-123 ± 27.05	-202 ± 24.5	-262 ± 21.9	-287 ± 23.3	-98.9 ± 26.2
5.02	-167 ± 30.8	-261 ± 23.0	-254 ± 23.0	-114 ± 24.0	-211 ± 28.3
6.68	-175 ± 24.6	-184 ± 25.3	-315 ± 24.7	-214 ± 20.4	-158 ± 27.6
8.34	-197 ± 25.7	-244 ± 23.6	-326 ± 22.7	-205 ± 23.2	-133 ± 31.5
10.00	-94.2 ± 24.5	-285 ± 24.1	-290 ± 21.2	-141 ± 25.5	-154 ± 28.3
11.66	-140 ± 26.7	-261 ± 25.2	-258 ± 23.9	-250 ± 24.7	-29.7 ± 26.8
13.32	-189 ± 24.5	-169 ± 23.3	-296 ± 25.1	-168 ± 24.2	-130 ± 30.5
14.98	-85.7 ± 24.2	-283 ± 23.9	-236 ± 28.6	-168 ± 22.3	-58.7 ± 24.3
16.64	-136 ± 28.2	-154 ± 21.6	-138 ± 24.5	-123 ± 21.3	-45.7 ± 27.1
18.30	-29.5 ± 23.3	-82.8 ± 20.2	-119 ± 23.8	-86.9 ± 22.9	-23.9 ± 26.5

Table E.5 σ_{yy} with standard deviation (MPa) for Specimen 230.

z-pos (mm) / x-pos (mm)	1.70	3.15	4.60	6.05	7.50
1.70	-174 ± 30.9	-110 ± 22.6	-74.4 ± 21.3	-151 ± 25.2	-16.3 ± 26.1
3.36	-186 ± 30.9	-225 ± 23.5	-322 ± 23.4	-259 ± 26.0	-123 ± 31.1
5.02	-165 ± 30.7	-245 ± 24.1	-301 ± 24.1	-149 ± 24.1	-160 ± 31.9
6.68	-191 ± 25.4	-230 ± 25.0	-326 ± 24.8	-204 ± 22.6	-123 ± 28.6
8.34	-183 ± 28.1	-272 ± 27.4	-340 ± 24.6	-178 ± 23.8	-130 ± 31.8
10.00	-144 ± 23.0	-249 ± 28.8	-264 ± 25.1	-170 ± 25.0	-172 ± 30.0
11.66	-144 ± 26.2	-253 ± 27.4	-273 ± 25.4	-261 ± 24.8	-56.2 ± 27.0
13.32	-149 ± 28.3	-206 ± 26.1	-297 ± 22.0	-204 ± 25.0	-111. ± 34.9
14.98	-85.7 ± 29.2	-302 ± 23.5	-245 ± 24.1	-189 ± 25.7	-60.9 ± 25.6
16.64	-165 ± 24.2	-197 ± 22.9	-96.1 ± 25.0	-130 ± 20.8	-59.8 ± 25.7
18.30	-150 ± 21.4	-136 ± 21.0	-157 ± 19.3	-202 ± 22.2	-85.0 ± 25.5

Table E.6 σ_{zz} with standard deviation (MPa) for Specimen 230.

z-pos (mm) / x-pos (mm)	1.70	3.15	4.60	6.05	7.50
1.70	-169 ± 25.1	-133 ± 17.4	-93 ± 20.2	-169 ± 22.4	-115 ± 22.1
3.36	-184 ± 24.7	-201 ± 19.1	-258 ± 19.6	-238 ± 24.0	-173 ± 24.8
5.02	-197 ± 24.2	-178 ± 18.8	-146 ± 18.9	-70.9 ± 22.8	-211 ± 26.9
6.68	-192 ± 19.8	-111 ± 20.2	-164 ± 20.9	-100 ± 23.2	-159 ± 24.2
8.34	-215 ± 24.8	-143 ± 21.2	-170 ± 21.1	-117 ± 24.6	-109 ± 25.0
10.00	-123 ± 21.7	-160 ± 21.1	-61.9 ± 20.6	-43.8 ± 23.0	-171 ± 26.0
11.66	-164 ± 21.6	-159 ± 22.2	-128 ± 22.7	-135 ± 24.0	-94.3 ± 25.7
13.32	-148 ± 22.8	-100 ± 19.8	-167 ± 19.5	-77.3 ± 24.2	-167 ± 27.8
14.98	-146 ± 23.7	-172 ± 20.0	-165 ± 22.1	-69.4 ± 23.6	-162 ± 22.0
16.64	-193 ± 23.3	-214 ± 20.6	-127 ± 20.0	-116 ± 22.2	-145 ± 23.5
18.30	-191 ± 21.0	-132 ± 18.4	-138 ±18.9	-174 ± 22.0	-108 ± 22.8

Table E.7 σ_{xx} with standard deviation (MPa) for Specimen 290.

z-pos (mm) / x-pos (mm)	1.70	3.15	4.60	6.05	7.50
1.70	-109 ± 28.2	-107 ± 32.6	-111 ± 28.7	-122 ± 28.8	-28.0 ± 32.0
3.36	-89.5 ± 30.3	-210 ± 31.4	-139 ± 29.9	-79.6 ± 30.0	-6.50 ± 31.1
5.02	-88.3 ± 30.4	-131 ± 37.8	-255 ± 29.0	-165 ± 31.4	-110 ± 32.9
6.68	-153 ± 31.0	-139 ± 28.1	-224 ± 30.5	-128 ± 31.0	-99.9 ± 33.4
8.34	-114 ± 34.3	-178 ± 31.8	-209 ± 33.7	-163 ± 34.3	-26.2 ± 33.9
10.00	-127 ± 28.2	-234 ± 34.3	-85.1 ± 30.9	-114 ± 31.8	-83.3 ± 42.2
11.66	-10.0 ± 37.0	-195 ± 33.5	-233 ± 33.6	-131 ± 30.5	-59.9 ± 35.6
13.32	-45.0 ± 30.9	-242 ± 32.3	-201 ± 29.7	-178 ± 31.5	-80.6 ± 33.8
14.98	-134 ± 31.1	-116 ± 32.1	-125 ± 29.5	-100 ± 31.5	4.5 ± 31.7
16.64	-21.5 ± 33.9	-153 ± 29.9	-218 ± 28.3	-164 ± 28.3	-13.2 ± 32.1
18.30	-37.7 ± 32.4	-118 ± 31.6	-38.3 ± 26.9	-53.6 ± 27.3	14.9 ± 30.6

Table E.8 σ_{yy} with standard deviation (MPa) for Specimen 290.

z-pos (mm) / x-pos (mm)	1.70	3.15	4.60	6.05	7.50
1.70	-143 ± 30.6	-60.9 ± 31.2	-57.3 ± 30.5	-101 ± 30.2	-45.1 ± 34.1
3.36	-111 ± 32.9	-186 ± 33.6	-126 ± 30.4	-52.2 ± 32.2	35.3 ± 35.2
5.02	-96.1 ± 33.8	-175 ± 37.6	-246 ± 30.0	-156 ± 32.0	-108 ± 35.0
6.68	-136 ± 31.8	-190 ± 32.3	-275 ± 29.3	-132 ± 33.0	-26.1 ± 33.5
8.34	-47.3 ± 31.2	-167 ± 35.8	-176 ± 31.4	-133 ± 35.3	4.2 ± 33.9
10.00	-102 ± 32.0	-180 ± 37.5	-81.5 ± 31.9	-104 ± 32.8	-120 ± 44.5
11.66	7.10 ± 33.9	-182 ± 35.3	-188 ± 29.9	-107 ± 32.8	-63.7 ± 33.7
13.32	-65.8 ± 32.9	-240 ± 29.1	-178 ± 31.8	-152 ± 29.8	-61.6 ± 35.4
14.98	-96.8 ± 30.3	-136 ± 30.8	-87.9 ± 30.4	-58.4 ± 29.5	-41.4 ± 36.1
16.64	-25.5 ± 31.2	-132 ± 28.3	-171 ± 27.5	-161 ± 27.3	34.1 ± 30.4
18.30	-107 ± 25.9	-96.4 ± 27.0	-45.5 ± 26.5	-56.4 ± 26.2	0.50 ± 26.1

Table E.9 σ_{zz} with standard deviation (MPa) for Specimen 290.

z-pos (mm) / x-pos (mm)	1.70	3.15	4.60	6.05	7.50
1.70	-178 ± 29.1	-70.5 ± 32.2	-67.6 ± 25.5	-96.8 ± 29.4	-87.6 ± 34.0
3.36	-152 ± 29.4	-195 ± 35.9	-141 ± 27.2	-30.1 ± 30.8	-34.4 ± 37.1
5.02	-118 ± 30.7	-91.9 ± 39.7	-96.3 ± 29.2	-137 ± 30.3	-114.3 ± 36.9
6.68	-90.2 ± 28.7	-73.0 ± 31.1	-75.6 ± 26.9	-89.6 ± 28.8	-82.1 ± 33.3
8.34	-70.2 ± 28.9	-41.0 ± 34.0	-67.7 ± 29.4	-20.5 ± 32.5	-10.5 ± 30.6
10.00	-98.8 ± 27.8	-123 ± 37.1	26.0 ± 28.5	1.70 ± 30.8	-58.6 ± 47.3
11.66	-27.8 ± 29.0	-67.1 ± 34.9	-92.7 ± 28.0	-8.90 ± 29.2	-57.2 ± 36.8
13.32	-39.7 ± 28.6	-128 ± 31.7	-62.6 ± 30.1	-85.8 ± 33.7	-86.5 ± 37.6
14.98	-159 ± 28.0	-28.1 ± 34.8	-30.9 ± 27.4	-31.6 ± 35.7	-64.5 ± 38.5
16.64	-107 ± 31.2	-125 ± 32.5	-217 ± 26.1	-175 ± 28.3	-55.7 ± 31.2
18.30	-85.1 ± 29.0	-110 ± 32.6	24.5 ± 33.7	-44.3 ± 30.2	-21.8 ± 33.1

Table E.10 σ_{xx} with standard deviation (MPa) for Specimen 330.

z-pos (mm) / x-pos (mm)	1.70	3.15	4.60	6.05	7.50
1.70	-81.9 ± 31.1	-99.1 ± 28.8	-53.1 ± 28.0	-104 ± 29.5	-31.0 ± 33.1
3.36	-130 ± 28.1	-204 ± 29.4	-132 ± 28.2	-50.1 ± 30.7	-25.2 ± 33.8
5.02	-44.5 ± 29.5	-111 ± 30.2	-123 ± 27.8	-9.00 ± 30.1	17.7 ± 32.1
6.68	-29.1 ± 29.5	-89.5 ± 30.5	-224 ± 30.2	-59.3 ± 29.1	10.7 ± 34.6
8.34	-16.0 ± 29.7	-40.1 ± 30.6	-87.0 ± 28.9	-35.8 ± 30.6	20.2 ± 33.8
10.00	25.5 ± 30.8	-59.8 ± 29.1	-63.3 ± 28.7	-34.7 ± 28.1	-10.6 ± 30.9
11.66	-62.3 ± 31.6	-67.8 ± 29.7	-98.7 ± 28.9	-71.7 ± 30.3	4.80 ± 32.7
13.32	-57.5 ± 31.3	-148 ± 29.4	-95.9 ± 29.2	-54.4 ± 31.2	67.4 ± 29.7
14.98	-94.7 ± 29.6	-122 ± 28.0	-163 ± 27.0	-62.2 ± 29.4	45.5 ± 30.9
16.64	-69.8 ± 27.6	-182 ± 27.7	-78.8 ± 26.8	-154 ± 26.2	6.20 ± 29.0
18.30	-92.9 ± 27.2	-93.1 ± 27.0	-103 ± 26.8	-70.5 ± 27.7	-28.9 ± 29.1

Table E.11 σ_{yy} with standard deviation (MPa) for Specimen 330.

z-pos (mm) / x-pos (mm)	1.70	3.15	4.60	6.05	7.50
1.70	-161 ± 29.5	-165 ± 28.2	-140 ± 29.3	-180 ± 29.8	-123 ± 30.1
3.36	-131 ± 29.9	-200 ± 29.0	-159 ± 27.1	-65.5 ± 28.8	-99.6 ± 32.1
5.02	-46.4 ± 28.9	-74.8 ± 30.2	-95.8 ± 28.4	-53.7 ± 28.5	-9.30 ± 32.4
6.68	-11.4 ± 29.5	-86.9 ± 31.1	-181 ± 31.8	-55.2 ± 29.5	-7.60 ± 31.7
8.34	-23.1 ± 28.6	-49.7 ± 31.8	-107 ± 27.6	-80.4 ± 30.1	-13.8 ± 33.4
10.00	-29.9 ± 31.8	-72.1 ± 29.3	-81.3 ± 28.4	-9.2 ± 29.3	18.3 ± 31.7
11.66	-76.9 ± 30.7	-55.4 ± 29.7	-129 ± 29.0	-72.5 ± 30.7	10.7 ± 31.4
13.32	-14.9 ± 29.4	-79.0 ± 30.6	-63.3 ± 29.2	-35.3 ± 31.8	14.4 ± 31.2
14.98	-97.1 ± 30.4	-122 ± 28.5	-155 ± 27.8	-45.3 ± 28.0	33.5 ± 31.5
16.64	-129 ± 28.9	-222 ± 28.3	-117 ± 28.4	-194 ± 27.9	-56.3 ± 29.8
18.30	-156 ± 27.4	-215 ± 29.3	-208 ± 28.1	-151 ± 27.9	-96.6 ± 28.9

Table E.12 σ_{zz} with standard deviation (MPa) for Specimen 330.

z-pos (mm) / x-pos (mm)	1.70	3.15	4.60	6.05	7.50
1.70	-114 ± 31.12	-122.7 ± 32.17	-63.4 ± 29.78	-100.1 ± 33.46	-115.8 ± 34.42
3.36	-158.3 ± 31.74	-205.3 ± 30.12	-134.6 ± 28.02	-47.8 ± 31.8	-98.5 ± 33.09
5.02	-61.2 ± 30.07	-73.4 ± 34.5	-33.5 ± 29.57	-11.8 ± 31.82	-66.1 ± 35.02
6.68	-38.3 ± 30.52	-23 ± 30.76	-98.6 ± 32.34	-33.2 ± 33.46	-35.8 ± 34.23
8.34	-51.7 ± 27.94	-13.2 ± 37.72	-83.5 ± 29.54	-52.5 ± 35.45	-51.5 ± 36.48
10.00	-17.7 ± 32	-19.4 ± 31.21	20.3 ± 31.22	5.8 ± 33.96	-42.1 ± 35.45
11.66	-55 ± 30.27	11.8 ± 31.62	-70 ± 32.58	-53.7 ± 34.15	-54 ± 33.38
13.32	-53.7 ± 31.79	-83.1 ± 33.81	-27 ± 29.15	24.8 ± 35.22	-29.4 ± 30.77
14.98	-119.4 ± 30.8	-31 ± 30.81	-99.5 ± 28.68	-36.8 ± 29.46	6.5 ± 36.78
16.64	-84.9 ± 30.76	-221.9 ± 31.29	-89.5 ± 28.26	-165.3 ± 28.51	-66.9 ± 34.47
18.30	-116.4 ± 29.2	-145.8 ± 33.59	-83.6 ± 32.16	-64.9 ± 33.49	-38.6 ± 33.17

E.2 Stress ratios of σ_{yy} to σ_{xx}

Table E.13 Ratio of σ_{yy} to σ_{xx} for Specimen 130.

z-pos (mm) / x-pos (mm)	**1.70**	**3.15**	**4.60**	**6.05**	**7.50**
1.70	-0.63	1.26	1.09	11.24	0.02
3.36	4.29	1.77	1.24	1.32	1.62
5.02	1.05	2.33	1.93	1.89	1.41
6.68	7.40	6.04	2.11	1.58	1.84
8.34	1.82	1.56	2.41	2.71	0.43
10.00	1.35	1.76	1.96	1.96	2.68
11.66	1.96	3.32	2.30	120	0.11
13.32	2.15	2.04	1.92	2.27	1.47
14.98	1.62	1.47	1.69	1.10	0.55
16.64	1.15	1.28	1.23	0.88	2.31
18.30	4.33	9.19	1.64	2.01	0.90

Table E.14 Ratio of σ_{yy} to σ_{xx} for Specimen 230.

z-pos (mm) / x-pos (mm)	1.70	3.15	4.60	6.05	7.50
1.70	3.75	2.00	3.22	1.45	0.51
3.36	1.50	1.12	1.23	0.90	1.24
5.02	0.98	0.94	1.19	1.31	0.76
6.68	1.09	1.25	1.04	0.95	0.78
8.34	0.93	1.11	1.04	0.87	0.98
10.00	1.51	0.87	0.91	1.21	1.12
11.66	1.03	0.97	1.06	1.04	1.89
13.32	0.79	1.22	1.01	1.21	0.85
14.98	1	1.07	1.04	1.13	1.04
16.64	1.21	1.28	0.70	1.05	1.31
18.30	5.10	1.64	1.32	2.32	3.56

Table E.15 Ratio of σ_{yy} to σ_{xx} for Specimen 330.

z-pos (mm) / x-pos (mm)	1.70	3.15	4.60	6.05	7.50
1.70	1.97	1.66	2.63	1.72	3.95
3.36	1.01	0.98	1.21	1.31	3.95
5.02	1.04	0.67	0.78	5.97	0.53
6.68	0.39	0.97	0.81	0.93	0.71
8.34	1.44	1.24	1.23	2.25	0.68
10.00	1.17	1.21	1.28	0.27	1.73
11.66	1.23	0.82	1.30	1.01	2.23
13.32	0.26	0.53	0.66	0.65	0.21
14.98	1.03	1.01	0.95	0.73	0.74
16.64	1.84	1.22	1.49	1.26	9.08
18.30	1.68	2.31	2.03	2.14	3.34

Appendix F XRD surface stress results

Stress components and error for each specimen obtained from XRD surface stress analysis

Table F.1 Surface stress components with error for each specimen.

Specimen	Stress component [MPa]		
	σ_{xx}	σ_{yy}	τ_{xy}
130	44 ± 10	55 ± 10	51 ± 10
160	82 ± 12	35 ± 12	32 ± 12
190	16 ± 10	15 ± 10	8 ± 10
230	-21 ± 15	-73 ± 15	-44 ± 15
260	-53 ± 16	-55 ± 16	29 ± 16
290	7 ± 12	-27 ± 12	-26 ± 12
330	107 ± 19	74 ± 19	9 ± 19
360	-99 ± 21	-45 ± 21	42 ± 21
390	-24 ± 16	91 ± 16	49 ± 16

Appendix G XRD stress vs depth profiling results

Stress components and error for each specimen obtained from XRD stress vs depth profiling analysis.

Table G.1 Stress components with error at each depth increment for specimen 130 and 160.

Specimen 130				Specimen 160			
Depth (mm)	**σ_{xx} (MPa)**	**σ_{yy} (MPa)**	**τ_{xy} (MPa)**	**Depth (mm)**	**σ_{xx} (MPa)**	**σ_{yy} (MPa)**	**τ_{xy} (MPa)**
0	-126 ± 42	-55 ± 17	29.5 ± 0.5	0	74 ± 11	-4.1 ± 43	-3 ± 8
0.009	38 ± 33	16 ± 20	37 ± 8.5	0.016	70 ± 17	3.6 ± 49	29.2 ± 12
0.016	84 ± 40	48 ± 30	0 ± 4	0.030	16 ± 20	-18 ± 52	60 ± 19
0.024	165 ± 33	28 ± 20	23.5 ± 11.5	0.050	44 ± 18	-3.4 ± 52	26.7 ±8
0.028	183 ± 36	-16 ± 18	28.5 ± 12	0.057	27 ± 18	-14 ± 53	38.5 ± 13.5
0.034	188 ± 32	-14 ± 24	47 ± 10	0.069	-42 ± 19	-37 ± 53	52.5 ± 16
0.042	176 ± 32	-18 ± 30	23 ± 12	0.083	-41 ± 16	-81 ± 58	57.2 ± 8
0.050	239 ± 33	35 ± 24	-21 ± 9.5	0.098	-26 ± 17	-82 ± 56	9 ± 6.5
0.056	297 ± 36	17 ± 28	7 ± 7	0.113	-42 ± 16	-97 ± 63	25.5 ± 7.5
0.062	266 ± 31	-15 ± 51	-22.5 ± 0	0.126	-83 ± 22	-93 ± 48	24 ± 1
0.072	272 ± 43	20 ± 32	-21 ± 8.5				

Table G.2 Stress components with error at each depth increment for specimen 190 and 230.

Specimen 190				Specimen 230			
Depth (mm)	**σ_{xx} (MPa)**	**σ_{yy} (MPa)**	**τ_{xy} (MPa)**	**Depth (mm)**	**σ_{xx} (MPa)**	**σ_{yy} (MPa)**	**τ_{xy} (MPa)**
0	21 ± 19	-41 ± 26	81 ± 7.5	0	-535 ± 92	-196 ± 65	170.5 ± 11.5
0.020	3 ± 28	-61 ± 32	104 ± 2	0.008	-600 ± 78	-251 ± 70	135.5 ± 12
0.040	-40 ± 26	-80 ± 33	113 ± 2.5	0.013	-659 ± 96	-252 ± 77	107.5 ± 2.5
0.059	15 ± 31	-66 ± 25	95.5 ± 5	0.019	-642 ± 93	-297 ± 76	119.5 ± 4.5
0.080	-10 ± 26	-83 ± 22	105.5 ± 1	0.027	-718 ± 104	-313 ± 76	90.5 ± 18
0.105	-47 ± 20	-51 ± 32	59 ± 8	0.034	-793 ± 120	-267 ± 64	5 ± 22
0.127	-81 ± 20	-46 ± 33	103.5 ± 1.5	0.043	-784 ± 119	-249 ± 63	5.5 ± 11
0.146	-92 ± 24	25 ± 26	110.5 ± 16	0.049	-724 ± 102	-275 ± 57	-13.5 ± 22.5
0.170	-92 ± 35	-19 ± 25	91.5 ± 1	0.056	-748 ± 105	-244 ± 55	-18 ± 20
0.183	-76 ± 32	-10 ± 23	62 ± 3.5	0.062	-830 ± 116	-233 ± 62	6.5 ± 17

Table G.3 Stress components with error at each depth increment for specimen 330.

Specimen 330			
Depth (mm)	**σ_{xx} (MPa)**	**σ_{yy} (MPa)**	**τ_{xy} (MPa)**
0	-1201 ± 233	-737 ± 207	-77 ± 44
0.009	-1246 ± 234	-785 ± 222	-80.5 ± 16
0.014	-1301 ± 229	-863 ± 221	-101 ± 18
0.022	-1323 ± 229	-856 ± 210	-77.5 ± 19.5
0.029	-1306 ± 233	-876 ± 213	-101 ± 13
0.035	-1312 ± 223	-822 ± 211	-163 ± 11
0.043	-1288 ± 219	-802 ± 200	-129 ± 8.5
0.051	-1287 ± 220	-854 ± 202	-134.5 ± 23
0.056	-1344 ± 224	-875 ± 205	-74.5 ± 13.5
0.067	-1352 ± 223	-858 ± 219	-83 ± 27